Thermoelectric Behavior of Quantum Dots Engineered Bulk Half-Heusler Nanocomposites

by

Yuanfeng Liu

A dissertation submitted in partial fulfillment
of the requirements for the degree of
Doctor of Philosophy
(Materials Science and Engineering)
In the University of Michigan
2015

Doctoral Committee:

Assistant Professor Pierre Ferdinand Poudeu Poudeu, Chair
Assistant Professor Emmanouil Kioupakis
Professor Joanna M. Millunchick
Professor Ctirad Uher

Dedication

To my family

For their love and support

Acknowledgements

I am using this opportunity to express my gratitude to everyone who supported my Ph.D study and research at the University of Michigan and University of New Orleans. I thank my advisor, Prof. Ferdinand Poudeu. During my study, he guided me with patience, encouragement, enthusiasm and immense knowledge. Without his help and guidance, I couldn't finish my study and this thesis. I could not imagine having a better advisor and mentor for my Ph.D study.

I would also like to thank Prof. Ctirad Uher and his group. Prof. Uher provided me with some great suggestions and ideas, which created a new direction in our investigation of thermoelectric materials. In addition, under the help of Prof. Uher and his group, I was able to conduct several important electronic and thermal transport measurements used in this thesis. I would also like to express my thanks to Prof. Xiaoqing Pan and his group for their assistance with microscope measurements.

My sincere thanks also go to the rest of my thesis committee: Prof. Emmanouil Kioupakis and Prof. Joanna Millunchick for their valuable suggestions, support and mentorship.

I also thank my fellow lab mates in Prof. Poudeu's research group: Erica Chen, Alan Olvera, Juan Lopez and Nicholas Moroz for their help and cooperation. I also thank the past post doctoral fellows in our group, Dr. Honore Djieutedjeu, Dr. Pranati Sahoo, Dr. Nathan Takas, Dr. Julien Makongo , Dr. Sanjaya Ranmohotti, Dr. Dinesh Misra for helping me with experiment design, result analysis and discussion.

Finally, I deeply thank my parents and husband for their tremendous support during my PhD study and throughout my life.

Table of Contents

List of Figures

Abstract

Over the past 20 years, thermoelectric materials have received more and more attention due to dwindling natural resources and inefficient energy conversion systems. In this thesis, focus was placed on the development of half-Heusler based nanocomposite materials for application in thermoelectric technology. Half-Heusler alloys were chosen as our research focus due to its environmentally friendly nature, cheap elemental constituents, and their robust mechanical stability relative to other thermoelectric materials. Half-Heuslers with 18 valence electrons are narrow band gap semiconductors with large Seebeck coefficients. Detrimentally, however, the thermal conductivity can reach ~ 10 $Wm^{-1}K^{-1}$. In order to improve the thermoelectric properties of half-Heusler, two main strategies were applied. The first strategy is to increase mass fluctuation or point defects in the sample during solid-state reaction. The second strategy is to add a doping element to tune the carrier density or other phases to form additional phonon scattering centers.

This work focuses on the effects of (1) the full-Heusler (FH) second phase, (2) heavy doping via Sb substitution at Sn sites, and (3) band gap engineering through Ge substitution at Sn sites on the electronic and thermal properties of half-Heusler (HH) matrices with composition $Ti_{0.1}Zr_{0.9}NiSn$. Additionally, (4) the concept of energy filtering at HH/FH interfaces on $Zr_{0.25}Hf_{0.75}Ni_{1+x}Sn_{1-y}Sb_y$ composites with varying doping levels is investigated. And lastly, (5) we explore the effect of varying chemical composition of the FH inclusions on the electronic and thermal properties of HH phases. This is achieved by the reaction of elemental Co with polycrystalline powder with composition $Zr_{0.25}Hf_{0.75}NiSn$.

CHAPTER 1

INTRODUCTION

1.1 Motivation and outline of the thesis

The development of materials (thermoelectric materials) suitable for the conversion of waste heat into electricity has received widespread interest in recent years as an alternative renewable energy technology. The performance of thermoelectric materials is measured by the dimensionless figure of merit, $ZT = \sigma S^2 T/\kappa$, where σ is the electrical conductivity, S is Seebeck coefficient, T is the absolute temperature and κ is the thermal conductivity [1-2].

Two main approaches are currently used to optimize the figure of merit of thermoelectric materials. The first focuses on the enhancement of the power factor ($PF = \sigma S^2$) by tuning the carrier density and mobility through chemical substitution and doping. The second strategy consists of reducing the thermal conductivity (κ) by enhancing phonon scattering within the materials. There are two main strategies to reduce the thermal conductivity by enhanced phonon scattering. The first strategy consists of increasing mass fluctuation or point defects in the sample during solid-state reaction [3-7]. The second consists of adding doping or other phase in the sample to form additional phonon scattering centers [8-10]. However, strategies to simultaneously improve the electrical conductivity and Seebeck coefficient are not clear and need more innovative research ideas and studies[11]. In our study, we explore full-Heusler (FH)

nanoparticles coherently embedded in the half-Heusler (HH) matrix and its effect on the thermal conductivity as well as Seebeck coefficient and carrier mobility of various HH/FH nanocomposites using the concept of phonon scattering and energy filtering of charge carriers at the HH/FH interfaces.

We will start in Chapter 1 with a short review of various concepts that are fundamental in thermoelectric materials research to enhance the thermoelectric figure of merit (ZT). This will include the development and catalogue of thermoelectric materials. Details of the synthesis methods and techniques used for characterization (structural and physical) and evaluation of the electronic and thermal properties are described in Chapter 2. Chapter 3 explores the large enhancements of thermopower and carrier mobility in quantum dot engineered bulk semiconductors with general composition $Ti_{0.1}Zr_{0.9}Ni_{1+x}Sn$. The addition of excess Ni element into the HH matrix ($Ti_{0.1}Zr_{0.9}NiSn$) generates FH nanophases coherently embedded in the HH matrix. The band gap difference between FH nanophase and HH matrix produces an energy filtering effect. Electrical and thermal transport properties are discussed taking into account the contribution of HH/FH interfaces to the carrier energy filtering and phonon scattering. In Chapter 4 we expand the investigation to the effect of FH nanophase on the electronic and phonon transports in Sb-doped $Ti_{0.1}Zr_{0.9}Ni_{1+x}Sn_{0.975}Sb_{0.025}$ nanocomposites. The aim is to discuss the effect of the energy potential at the HH/FH interfaces on the transport of extrinsic carrier introduced through substitution of Sb at the Sn sites. Chapter 5 reports on the thermoelectric properties of Ge doped n-type $Ti_xZr_{1-x}NiSn_{0.975}Ge_{0.025}$ half-Heusler alloys. The effects of (1) mass fluctuation due to the intermixing of Zr/Ti and Sn/Ge at the same atomic position and (2) nanostructuring arising from the phase segregation into Ti-rich and Zr-rich phases, on the thermal conductivity are discussed. In addition, discussion on the effect of band gap engineering

through isolelectronic substitution of Sn and Ge on the electronic transport properties of the synthesized phases is presented. In Chapter 6, we probe the effect of the potential barrier, at the HH/FH interfaces, on the transport of extrinsic carriers in $Zr_{0.25}Hf_{0.75}Ni_{1+x}Sn_{1-y}Sb_y$ HH matrix with decreasing doping level. The objective is to deeply analyze and understand the relationship between the energy filtering effect at the interface of FH/HH phases and the doping level. In heavily doped samples, the extrinsic carrier concentration depends on concentration of Sb dopant as well as the fraction of extrinsic carriers contributed by metallic FH phases. Therefore, it is anticipated that the extrinsic carriers in such heavily doped nanocomposites form an impurity band with a broad energy range. Under these conditions, the fraction of extrinsic electrons transmitted across the HH/FH interface is related to the height of the potential energy barrier, which in turn is related to the average size range of the FH nanophase. Chapter 7 investigates the thermoelectric properties of $Zr_{0.25}Hf_{0.75}NiSn$ HH matrix with excess Co element. Unlike the previous HH/FH composites in which the FH phase contains similar elements with the HH matrix and only different in stoichiometry, the vacancy in this system is filled by an heteroelement, Co, to produce Co-containing FH phase with composition $Zr_{0.25}Hf_{0.75}NiCoSn$. Such manipulation of the chemical composition of the FH phase using Co instead of Ni could help engineer the energy offset of the conduction band minima (CBM) at the HH/FH interfaces and/or introduce a p-type dopant into the HH matrix. The effect of this chemical manipulation of the composition of the FH phase on the electronic and thermal transport properties for the resulting composites is discussed. Chapter 8 concludes this dissertation with the summary of the current studies.

1.2 Seebeck Effect and Peltier Effect

Thermoelectric materials can directly convert heat to electrical energy under certain temperature gradients. In thermoelectric research, two key phenomena, the Seebeck effect and the Peltier effect, play the most important roles in their application. As shown in Figure 1.1(a)[12], when a heat resource is placed on one side and a cold resource is on the other side, an electrical current can be created. This is known as the Seebeck effect [13-14]. Inversely, when an electrical voltage is applied through a circuit of interconnected p and n type thermocouple (Figure 1.1(b)) using an external power source, one side will become hot and other side will be cold. This is known as the Peltier effect. Based on these two effects, several p-n junctions can be connected with each other to create a thermoelectric module (Figure 1.1(c)). These thermoelectric modules can be applied in industrial waste heat conversion and vehicle-heating systems such as power generation or refrigeration.

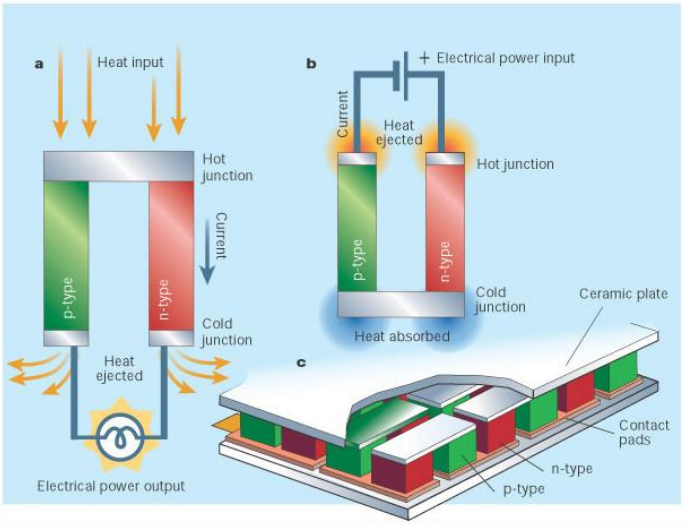

Figure 1.1 Schematic representations of the Seebeck effect (a), Peltier effect (b) and thermoelectric module (c).

1.3 Development of thermoelectric materials

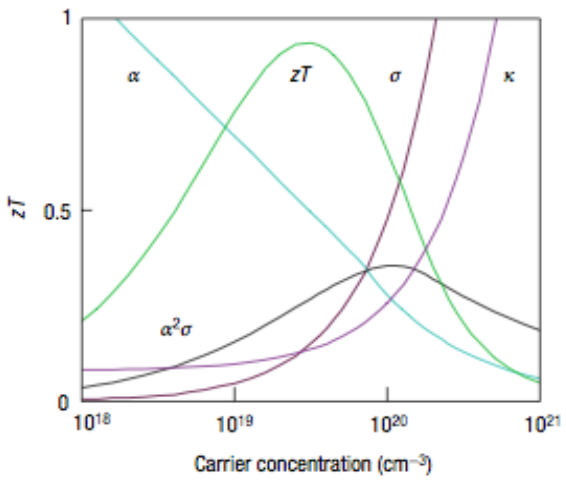

Figure 1.2 The relationship between carrier concentration and figure of merit, ZT, which involves Seebeck coefficient (α), electrical conductivity (σ), thermal conductivity (κ), ZT and power factor (α2σ). [11]

Ideal thermoelectric materials are phonon-glass/electron-crystal (PGEC) materials with a large Seebeck coefficient, low thermal conductivity and high crystal-like electrical conductivity [15-17] . The effectiveness of thermoelectric materials is characterized by the dimensionless thermoelectric figure of merit, $ZT = S^2\sigma T/\kappa$, where $S^2\sigma$ is the power factor[1-2]. According to this equation, ZT can be optimized by increasing the Seebeck coefficient and electrical conductivity, while simultaneously decreasing the thermal conductivity. However, it is very difficult to adjust these properties in such a trend. Figure 1.2 shows the relationship between carrier concentration and different thermoelectric properties[1]. When the carrier concentration increases, electrical conductivity and thermal conductivity would increase which results in a reduction in the Seebeck coefficient.

Although the correlations between various transport parameters make ZT optimization difficult to control, many thermoelectric materials with ZT >1 could be discovered [18] . They include materials systems such as Bi_2Te_3[13, 19-20] , SiGe[21-23] and PbTe[24-25] .

1.4 Half-Heusler intermetallic alloys

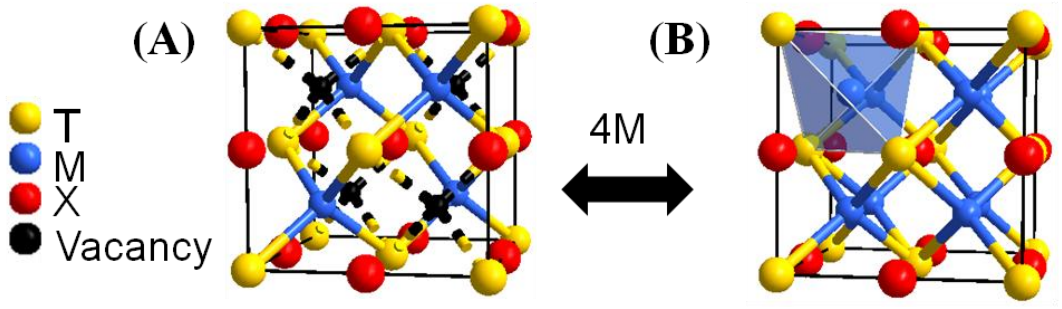

Figure 1.3 Comparison of the half-Heusler and full-Heusler crystal structures. (A) half-Heusler alloys (TMX) crystallize in the faced centered cubic (fcc) MgAgAs structure type (space group: F-43m) with half of the tetrahedral position vacant. Upon filling the vacant tetrahedral position with an additional M element, the corresponding full-Heusler phase (TM2X) crystallizing in the cubic MnCu2Al structure-type (SG: Fm-3m) is obtained (B).

As a member of the family of thermoelectric materials, half-Heusler (HH) alloys are suitable for energy conversion at 700K and above, which is close to most industrial waste heat sources[20, 26-29]. HH alloys represent a fascinating large class of intermetallic phases with general composition TMX (T and M are transition metal or rare-earth metals and X is a main-group element) and crystallize in the MgAgAs structure type (space group: *F*-43*m*). Their structure can be described as consisting of four interpenetrating *fcc* (face-centered cubic) sublattices of T, M and X atoms occupying the crystallographic positions (0,0,0), (1/4, 1/4, 1/4) and (1/2, 1/2,1/2), respectively, whereas the fourth (3/4, 3/4, 3/4) position is vacant [24, 30]. Upon filling the empty site, (3/4, 3/4, 3/4), within the structure of a HH (TMX) with an additional M atom, one directly generates the related ternary full-Heusler (FH) phase with general composition TM_2X (Figure 3.1)[4, 31]. While this conversion of a HH structure to the related FH generally induces only a marginal increase (2 to 5%) in the unit cell parameter, drastic changes in the crystal symmetry occur when switching from the non-centrosymmetric cubic MgAgAs structure type (SG: *F*-43*m*) to the centrosymmetric cubic $MnCu_2Al$ structure-type (SG: *Fm*-3*m*). This spontaneous and reversible change in the crystal symmetry upon varying the chemical composition makes the HH

and FH compounds, two distinct classes of structurally related materials exhibiting dissimilar physical and chemical properties specific to each class [4, 6-7, 32-50].

Although, these fascinating two families of compounds have been treated separately over the past several decades, the ability to interchange between the HH and FH structure upon addition or removal of M atoms (at the (3/4, 3/4, 3/4) site) enables the atomic-scale manipulation of the properties (chemical, physical, mechanical, electrical, optical etc) of one material by the other [51-56]. Half-Heusler (HH) alloys play an important role in the search for high efficiency thermoelectric materials because of their moderate thermopower and electrical resistivity [35, 42]. In addition, half-Heusler phases are chemically and thermally stable (melting above 1470K with almost no sublimation at temperatures below 1270K); they are easy to prepare in large-scale quantities using conventional solid-state synthesis techniques. They also involve cheap, abundant, lightweight and environmentally friendly elements. These advantages make HH materials suitable for large-scale utilization in high temperature energy conversion devices [16-17, 26].

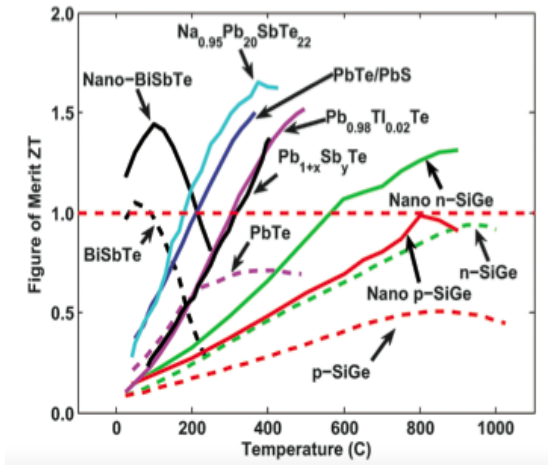

Figure 1.4 The relationship between figure of merit ZT and temperature for various thermoelectric materials.

Half-Heusler compounds with 18 valence electrons are narrow band gap semiconductors with large Seebeck coefficients and effective mass [57-58]. Uher et al. showed that ZrNiSn has a large Seebeck coefficient in the range of -170 to -210 μV/K at room temperature[42] and Poon,S.J., et al.[59]also obtained a large Seebeck coefficient of about -400 μV/K at room temperature. However, the drawback of HH compounds is their inherently high thermal conductivity. For example, the thermal conductivity of MNiSn and

MCoSb (M= Ti, Zr, Hf) are on the order of 10 $Wm^{-1}K^{-1}$ at room temperature[42, 60-61]. Therefore, the main research effort in developing superior HH compounds is to optimize synthesis methods or techniques to produce materials with significantly reduced the thermal conductivity, while simultaneously keeping a high power factor.

1.5 Energy filtering Effect

The observed large ZT values are often credited to drastic reductions in the total thermal conductivity arising from the scattering of a broad phonon spectrum at matrix/nanoinclusions interfaces and at grain boundaries with various length scales [11, 62-72]. However, the high density of interfaces (phase boundaries and grain boundaries) within the semiconducting matrix arising from the nanostructuring generally leads to large reductions in the carrier mobility offsetting the benefit of a large reduction in total thermal conductivity. Recently, the concept of band-engineering at the matrix-nanoinclusions interfaces has been introduced as an effective strategy to achieve efficient electronic transport simultaneously with large reductions in the lattice thermal conductivity of bulk nanostructured semiconductors [3, 5, 7, 11, 71-72]. This concept exploits structural similarities between the matrix and inclusion phases to create matrix/inclusion interfaces with arrangements (aligned or offset) of their valence band (VB) and/or conduction band (CB) favorable to efficient carrier transport. For instance, a small mismatch between unit cell dimensions is necessary to achieve the formation of coherent matrix/inclusion phase boundaries, while a similarity in the positional distribution of at least one type of atom within both structures (matrix and inclusion) is expected to increase the degree of similarity between the electronic band structure of both phases facilitating their suitable arrangement at their interface. Minimal disruption of the electronic transport and in few cases even some enhancements in the

carrier mobility and thermopower, have been reported in such bulk nanostructured materials[3-7, 11, 32, 70-71, 73-81]. For example, we have recently observed that large enhancements in the carrier mobility and thermopower can be achieved simultaneously with large reductions in the thermal conductivity in both n-type and p-type half-Heusler alloys when nanometer scale FH nanostructures are coherently embedded within their matrices [3-4, 7, 82].

CHAPTER 2

EXPERIMENTAL TECHNIQUES

2.1 Synthesis

All composites were synthesized either via solid-state reaction of the elements in a regular tube furnace or induction melting. Mechanical alloying was also applied to reduce the impurity and grain size in order to further decrease thermal conductivity.

2.1.1 Solid-State Synthesis

The nanocomposites with general composition $Ti_{0.1}Zr_{0.9}Ni_{1+x}Sn$, $Ti_{0.1}Zr_{0.9}Ni_{1+x}Sn_{0.975}Sb_{0.025}$, $Zr_{0.25}Hf_{0.75}NiSn_{1-x}Sb_x$ and $Zr_{0.25}Hf_{0.75}NiCo_xSn$ were synthesized by solid-state reaction of high purity (99.99%) elemental powders in the desired ratio. The elemental powders were thoroughly mixed using an agate mortar and pestle under an inert Ar atmosphere, and the resulting activated powder mixture was then sealed into a quartz tube under a residual pressure of 10^{-3} Torr and subsequently heated at 300 and 900 °C for 3 and 7 days, respectively. The heat profile was separated into two steps in order to decrease the evaporation of Sn element, which melting point is lower than that of Ti, Zr, Ni, Sn and Ge.

2.1.2 Induction Melting

Induction melting is an efficient rapid heating non-contact method for synthesizing alloys, metals and electrically-conductive materials. The main working parts of an induction heating system include an induction power supply and work coil. The work coil is water-cooled, and does not touch the sample when heat is produced in the sample. This method can be applied in metals such as steel, copper, aluminum or semiconductors. For our composites, the melting point of most elements is above 1000°C. So it is difficult to melt these elements in the normal tube furnace and will take a long time. However, the induction melting can heat elements in the temperature range from 100 °C to 3000 °C in a short time[83] . So the induction melting is a good choice to synthesize FH/HH composites.

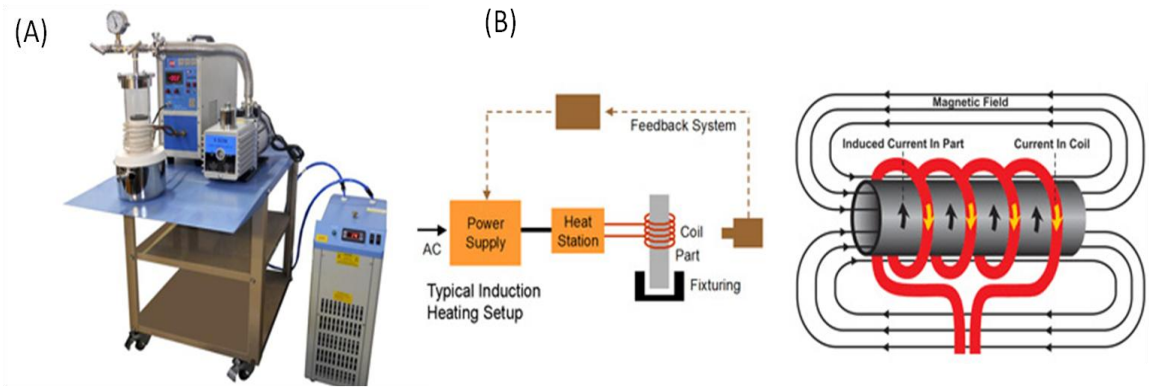

Figure 2.1 (A) Picture of the induction heating system in our lab; (B) The working principle of induction heating system and the work coil.

The principle of induction melting is shown in Figure 2.1[84]. In the induction heating system, the alternating current (AC) on the work coil creates an electromagnetic field. The sample as the secondary of the transform is loaded into this field; the heat is produced due to eddy current heating. In this process, the work coil induces current flow in the sample, which is the main reason for heating in the electromagnetic field. The operating frequency for induction melting

depends on the size of the sample and the material it is made from[83] . In the synthesized composites $Ti_xZr_{1-x}NiSn_{0.975}Ge_{0.025}$, induction melting was used under two different operating frequencies and durations. In the first step, a low operating frequency, 350 kHz, was used for 1 min in order to reduce the evaporation of Sn element. This step is repeated 2 times. After that, the operation frequency was increased to 720 kHz for 20 sec. This step was repeated 3 times to improve homogeneity of the melt.

2.1.3 Mechanical Alloying

In order to reduce thermal conductivity, reduction in the grain size is a simple and effective method. Ball milling has been applied in the synthesis process of thermoelectric composites since the 1960s[85] . The mechanical alloying approach utilizes two types of ball milling systems: the low-energy planetary ball-milling and the high-energy shaker ball-milling (Figure 2.2). The planetary ball milling can mix and ground powder at the same time. The grain size of composites can be reduced from several hundred micrometers to below a hundred micrometers. By utilizing high-energy shaker ball-milling, the grain size of composites can be decreased to the nanometer scale facilitating the formation of large quantity nanoparticles. From the commercial point of view, high-energy ball milling is usually combined with hot pressing to generate low thermal conductivity nanoparticles in a short time. From a research point of view, this combined method is used to synthesize composites with different elements and doping levels[86] . Furthermore, bulk pellets with high densification can be obtained through the ball milling and hot pressing processing techniques. For example, the densification of the hot pressed nanocomposites can reach 98%[87] which is comparable than that of the single crystalline materials[86, 88] .

$Ti_xZr_{1-x}NiSn_{0.975}Ge_{0.025}$ composites were synthesized by mechanical alloying using high-energy shaker ball milling. The powder composites were loaded into a stainless-steel jar with

stainless-steel balls using a SPEX Sample Prep Mixer/Mill. In order to prevent oxidization, the stainless-steel jar is filled with Ar atmosphere. The milling time depends on the type of mill used, the intensity of milling, the ball-to-powder ratio, and the temperature of milling. Contamination will increase when the time of milling increases [89]. So according to these factors, the ball-to-powder weight ratio of 1:4 was used for the synthesis of the composites, and the time of milling was kept constant at 2 hr.

After mechanical alloying, the activated powders were consolidated into a pellet at 950 °C under 100 MPa using a uniaxial hot pressing.

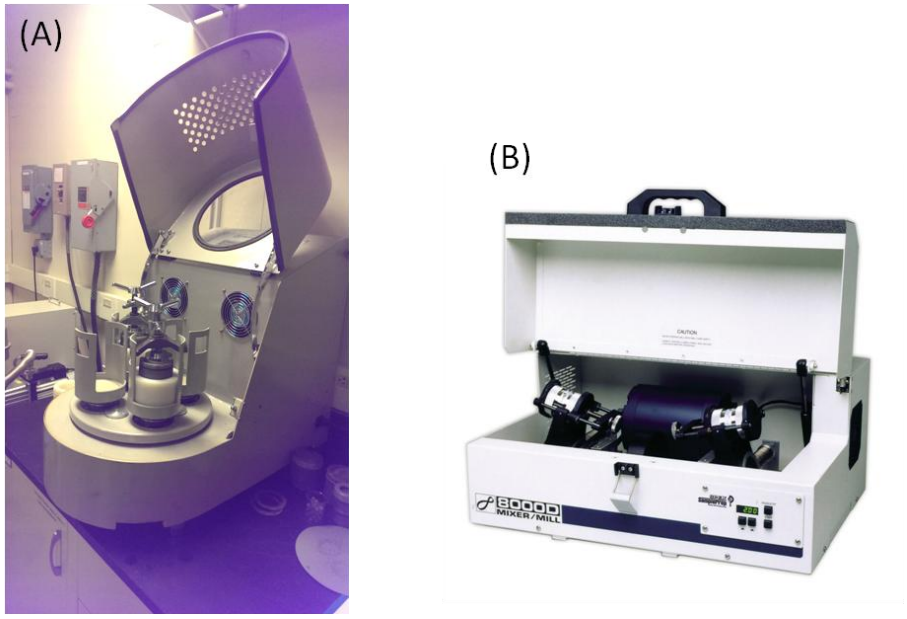

Figure 2.2 Pictures of ball milling: (A) Planetary ball milling, and (B) high energy ball milling.

2.2 Structural Characterization

The crystalline structure and internal structure play important roles in the material properties. The nanoparticle dispersion, size and phase fraction can bring more details to the analysis and

understanding of changes in the thermoelectric and physical properties in the synthesized composites. In this section, some of the structural characterization techniques used will be summarized.

2.2.1 Powder X-ray Diffraction (PXRD)

Powder X-ray diffraction (PXRD) is a basic way to characterize the phase purity of crystalline structures. For our composites, powder X-ray diffraction (PXRD) patterns were collected on a rotating anode Rigaku powder diffractometer operated at 40 kV and 100 mA using monochromatic Cu Kα radiation.

2.2.2 High Resolution Transmission Electron Microscope

High-resolution transmission electron microscopy (HRTEM) enables imaging of materials on the atomic scale. All composite samples in our research were examined under the standard HRTEM (JEOL 3011). Samples for HRTEM were prepared using grinding/polishing and focused ion beam (FIB). For the grinding/polishing method, a small piece sample was cut from selected pellets. Then this small piece sample is glued on grinding tool[90] (Figure 2.3) and polished using sand paper with different roughness. As the thickness of the sample is polished to 3.5 microns, a grid is used to move the sample out from polishing tool. The resulting sample is loaded into the SEM/FIB for ion-milling as part of the final thinning procedure[91] .

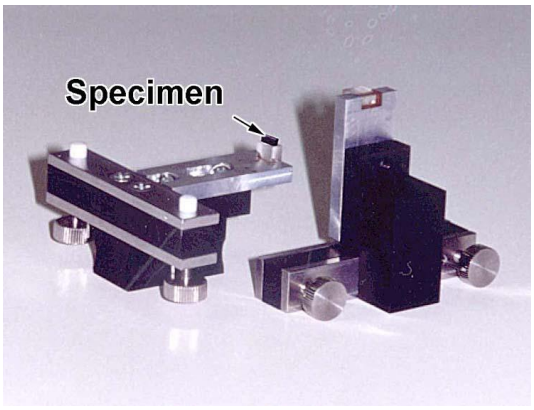

Figure 2.3 Picture of TEM sample grinding tool in our lab.

2.2.3 Scanning Electron Microscope

Scanning Electron Microscope can provide the information of a sample's surface topography and composition using a focused beam of electrons. For the $Ti_xZr_{1-x}NiSn_{0.975}Ge_{0.025}$ compounds, SEM was used to analyze the phase separation and composition. The BSE image of $Ti_xZr_{1-x}NiSn_{0.975}Ge_{0.025}$ showed a two-tone contrast indicating Ti-rich and Zr-rich phases. Energy dispersive spectrometer (EDS) attached to the SEM system provides the information on the composition. From the analysis of the EDS spectra, no impurity or other elements were observed.

2.3 Thermoelectric Properties Characterization

Thermoelectric properties such as thermal conductivity, Seebeck coefficient, electrical conductivity and Hall Effect were measured on various HH/FH composites.

2.3.1 Thermal Conductivity

Thermal conductivity is the capacity of a material to conduct heat, which depends on temperature. Thermal conductivity can be calculated by $\kappa = AC_p\rho$, where A is the thermal diffusivity, C_p is the heat capacity, ρ is the density. In our research, the laser flash method (Linseis, LFA 1000) was applied to measure the thermal diffusivity. In the measurement process, one side of the disc shape sample is exposed to a laser burst leading to an increase of the surface temperature. A liquid-nitrogen-cooled detector measures the temperature rise on the other side of the pellet. The thermal diffusivity is then computed from the heat flow versus time. The thermal conductivity is calculated using the thermal diffusivity data. The thermal conductivity of various HH/FH samples in this study was measured from room temperature to 500 °C under dynamic vacuum (~ 10^{-3} Torr). The instrument precision on thermal diffusion data is ± 5%.

2.3.2 Seebeck Coefficient and Electrical Conductivity

The Seebeck effect, Thomson effect and Peltier effect are three basic phenomena observed in thermoelectric materials. Based on these effects, thermoelectric materials can directly convert heat to electric energy. When a temperature gradient is applied to a circuit with two dissimilar conductors, a voltage between A and B is produced (Figure 2.4 A). The Seebeck coefficient is defined as the instantaneous rate of the Seebeck effect to temperature, $S = \Delta V/\Delta T$[92]. The Peltier effect produces an inverse effect to the Seebeck effect. When a voltage is added to the circuit, the temperature difference will form (Figure 2.4 B).

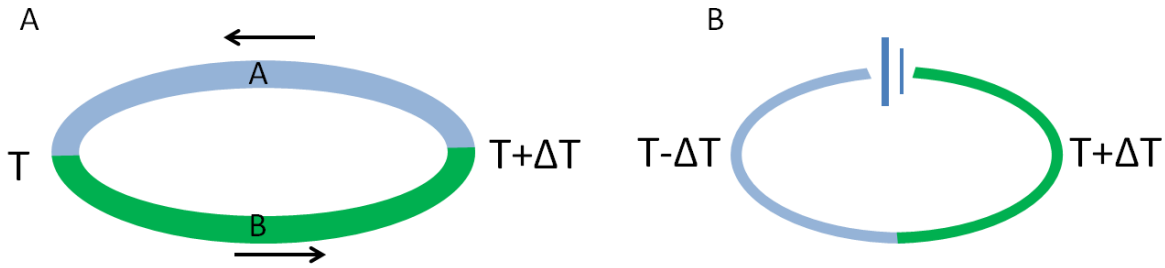

Figure 2.4 Scheme to (A) The Seebeck effect; and (B) the Peltier effect

Based on the definition of the Seebeck effect, the instrument ZEM-3 (Figure 2.5) was invented to simultaneously measure the Seebeck coefficient and electrical resistivity. The measured sample is vertically loaded between two blocks in the furnace. When the lower block heats the sample, the temperature gradient is formed. The Seebeck coefficient is measured using the upper and lower temperature T_1 and T_2, and the thermal electromotive force dE comes from the thermocouples. Electrical resistivity was being measured through a four-terminal method. When a constant current, I, is applied to both ends of sample, the electrical resistivity can be measured through a voltage drop dV between the thermocouples[93] .

In this work, the Seebeck coefficient and electrical conductivity were simultaneously measured from room temperature to 500°C under a low pressure He atmosphere using a commercial ZEM-3 system from ULVAC-RIKO. The instrument precision on the Seebeck coefficient and electrical conductivity data is ±4%.

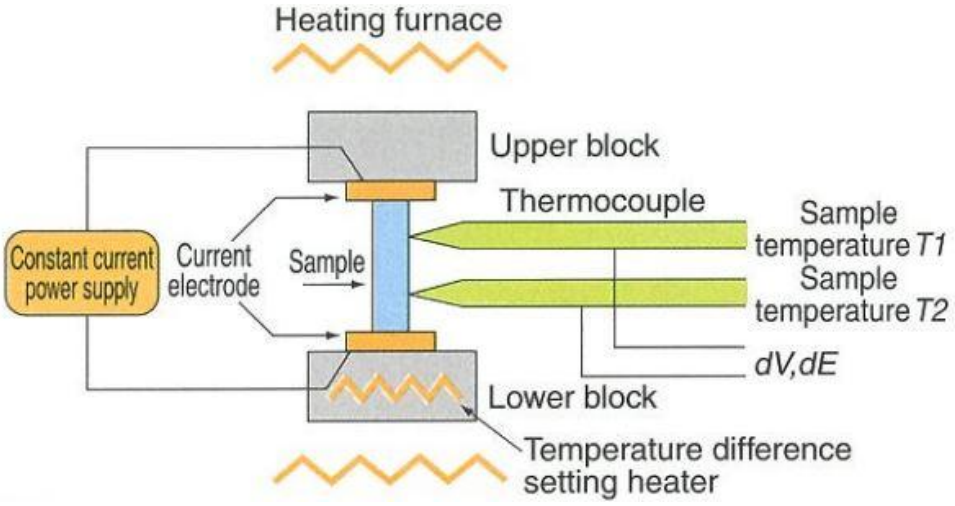

Figure 2.5 The principle of ZEM-3.

2.3.3 Hall Coefficient

The Hall coefficients data were measured in the temperature range from 300K to 775K under the magnetic field of 1T using a large Oxford air-bore superconducting magnet cryostat that accommodates a small tubular oven and a Hall insert[3]. The instrument uncertainty on Hall coefficient data is ±5%.

CHAPTER 3

LARGE ENHANCEMENTS OF THERMOPOWER AND CARRIER MOBILITY IN QUANTUM DOTS ENGINEERED BULK SEMICONDUCTORS

3.1 Objective

Here, we show that the thermopower and carrier mobility (μ) within a bulk semiconducting half-Heusler (HH) matrix with known composition ($Ti_{0.1}Zr_{0.9}$)NiSn (constant carrier density), are gradually enhanced by embedding in a coherent fashion, various fractions of full-Heusler (FH) quantum dots (QDs) within the crystal lattice of the HH matrix. The endotaxial formation of the FH quantum dots within the HH matrix was confirmed by transmission electron microscopy (TEM) studies. Using electrical conductivity and Hall effect data, we demonstrate the effectiveness of quantum dots in tailoring the effective charge carrier density, mobility and effective mass (m*) within the bulk HH matrix. The concept of carrier culling at the HH/ FH-QD conduction bands minima offset energy, ΔE, is introduced as a rational mechanism by which the embedded FH-QDs alter electronic transport within the HH matrix. A gradual decrease in the effective carrier density and an increase in the effective mass with increasing content of the FH-QD resulted in a drastic increase in the thermopower, whereas a simultaneous large increase in

the carrier mobility minimizes the drop in the electrical conductivity leading to an unprecedented enhancement of the power factor (PF). This ability to enhance the power factor of thermoelectric materials using coherently embedded quantum dots coupled with the reduction in thermal conductivity via nanostructuring strategy opens up new ways to design atomic-scale structurally engineered counterparts of existing *n*-type and *p*-type thermoelectric materials with drastically enhanced figures of merit.

3.2 Results and Discussion

3.2.1 Fabrication and Characterization of Quantum Dots Engineered HH Semiconductors

Quantum dots (QD) engineered half-Heusler (HH) semiconducting composite materials consisting of $Ti_{0.1}Zr_{0.9}NiSn$ (HH) matrix with various mole fractions of quantum dots (QDs) with full-Heusler (FH) structure (nominal composition $Ti_{0.1}Zr_{0.9}Ni_2Sn$) coherently embedded within the crystal lattice of the HH matrix was achieved by direct solid-state reaction of a mixture of high purity elemental powders of Zr, Ti, Sn and Ni in the desired stoichiometry, at 900 °C for seven days. The mole ratio of Zr, Ti, Ni and Sn is calculated to form a pure HH phase, and various amount of excess elemental Ni (0 at.%, 2 at.%, 4 at.% and 10 at.%) is added to the initial mixture to program a simultaneous partial solid state transformation of the resulting HH phase into a FH structure according to reaction (1). Structural characteristics of the resulting $Ti_{0.1}Zr_{0.9}Ni_{1+x}Sn$ nanocomposites were investigated using X-ray powder diffraction (XRD) and transmission electron microscopy (TEM). XRD data (Figure 3.1A) of the as-synthesized $Ti_{0.1}Zr_{0.9}Ni_{1+x}Sn$ (x = 0.02, 0.04 and 0.1) materials suggested the formation of a single phase HH product as all diffraction peaks were indexed in the cubic MgAgAs structure type (space group:

F-43*m*). No additional peak that could be assigned to the anticipated FH secondary phase or to any other impurity phase could be observed on the diffractions patterns, even for samples with the expected FH mole fraction of up to 10% (x = 0.1). This suggests according to reaction (1) the formation of FH precipitates that are on the order of atomic to nanometer scale and do not form aggregates large enough to diffract. Alternatively, the absence of additional peaks on the XRD patterns may indicate the formation of impurity phases that are soluble within the HH matrix. However, the unit cell parameter of the HH matrix in various $Ti_{0.1}Zr_{0.9}Ni_{1+x}Sn$ (x = 0.02, 0.04 and 0.1) materials refined using diffraction peaks from the XRD patterns showed a constant value (Table 3.1) suggesting that the composition and structure of the HH matrix remain unchanged upon addition of various fractions of excess elemental Ni.

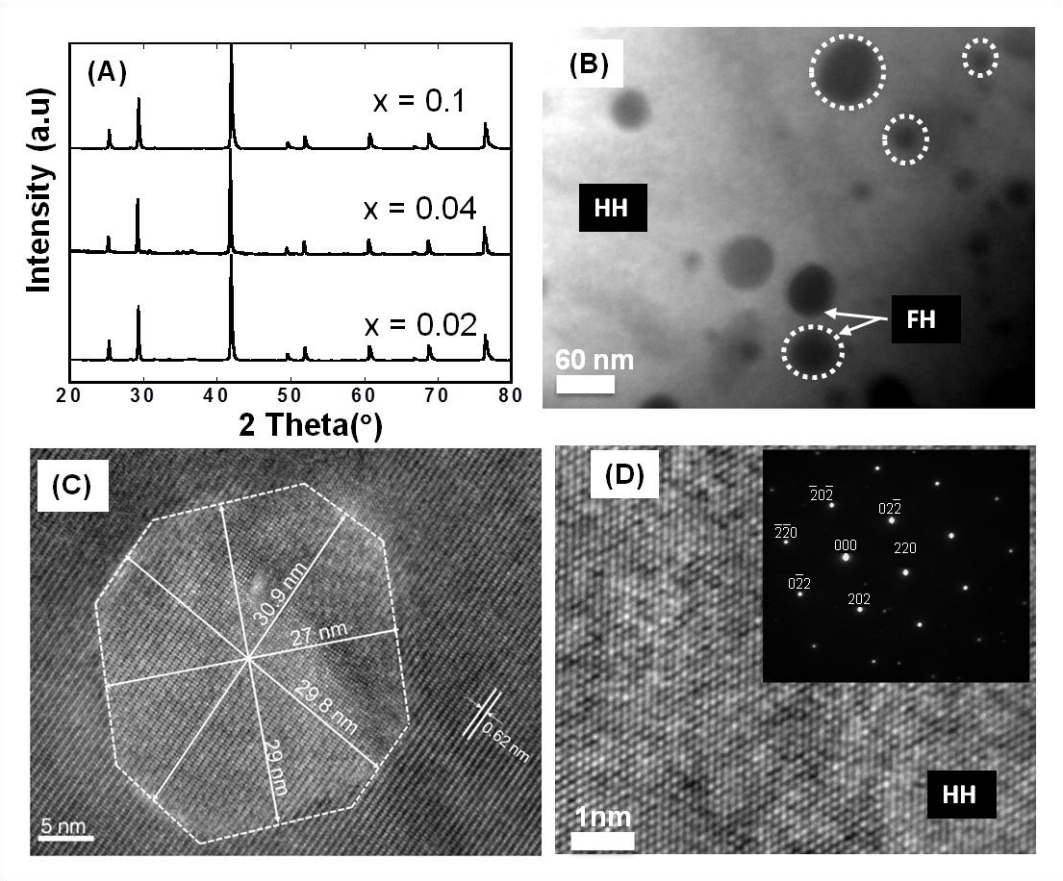

Figure 3.1 Structural characteristic of Ti0.1Zr0.9Ni1+xSn nanocomposites. (A) XRD patterns of the as-synthesized $Ti_{0.1}Zr_{0.9}Ni_{1+x}Sn$ materials showing only diffraction peaks of the pure half-Heusler (HH) phase. No additional peaks corresponding to the anticipated full-Heusler (FH) secondary phase could be observed. (B) Low-magnification image of the nanocomposite with x = 0.04 showing FH nanoparticles with broad size distribution (10 nm to 60 nm) coherently embedded inside the HH ($Ti_{0.1}Zr_{0.9}NiSn$) matrix. (C) High magnification image of a typical nearly spherical FH nanoparticle (quantum dot) from the nanocomposite with x = 0.1, showing detailed lattice structure. No noticeable strain is observed at the interface between the particle and the matrix suggesting endotaxial insertion with minimal lattice distortion of the FH particle within the HH matrix. (D) High magnification image of the HH matrix showing its excellent crystallinity and selected-area electron diffraction pattern (inset of D) indicating the FCC structure of the HH matrix.

To further assess the compositional stability of HH matrix in various $Ti_{0.1}Zr_{0.9}Ni_{1+x}Sn$ (x = 0.02, 0.04 and 0.1) composites, careful analysis of the atomic fraction of Ti, Zr, Ni and Sn in various specimens was performed using wavelength dispersive spectroscopy. The atomic fraction of various elements (Ti, Zr, Ni, Sn) in each specimen (Table 3.1) was calculated by averaging thirty

data points collected from various locations on the specimens. For each sample, the observed atomic fraction of Ti, Zr, Ni, and Sn is within ± 2 at.% of the expected nominal matrix composition (Ti: 3 at.%; Zr: 30 at.%; Ni: 33 at%; Sn: 33 at.%). The nearly constant values of the atomic fraction of Ti, Zr, Ni and Sn observed in various specimens strongly indicate that the chemical composition of the HH matrix remains constant in the synthesized $Ti_{0.1}Zr_{0.9}Ni_{1+x}Sn$ composites, in accord with the chemical equation (1).

$$0.1Ti + 0.9Zr + (1+x)\,Ni + Sn \rightarrow (1-x)\,Ti_{0.1}Zr_{0.9}NiSn\ (HH) + xTi_{0.1}Zr_{0.9}Ni_2Sn\ (FH) \qquad (1)$$

Table 3.1: Wavelength dispersive spectroscopy (WDS) elemental analysis of the matrix composition in $Ti_{0.1}Zr_{0.9}Ni_{1+x}Sn$ samples, and unit cell parameter of HH matrix

Sample	Ti (at.%)	Zr (at.%)	Ni (at.%)	Sn (at.%)	Unit cell parameter (Å)
Matrix (x = 0)	1.8	30.3	33.0	34.6	6.095(4)
HH (98%)/FH (2%) (x= 0.02)	1.8	30.7	32.7	34.8	6.115(8)
HH (96%)/FH (4%) (x = 0.04)	1.7	31.0	32.9	34.6	6.098(4)
HH (90%)/FH (10%) (x = 0.1)	1.8	30.5	33.3	34.5	6.104(5)

To probe the presence of the FH secondary phase within the synthesized nanocomposites and also to determine their characteristics (average size, size distribution and morphology), high resolution transmission electron microscopy (HRTEM) study was performed on selected

specimens. TEM images from the sample containing 4 at.% excess Ni ($Ti_{0.1}Zr_{0.9}Ni_{1.04}Sn$), which corresponds to a nanocomposite system consisting of 96 mole% HH and 4 mole % FH (96%HH/4%FH), reveal that the FH precipitates have nearly spherical morphology with size ranging from 10 to 60 nm (Figure 3.1B). The spherical shape of the nanodots suggests endotaxial nucleation of the precipitate seed crystals within the HH crystal lattice followed by their isotropic growth. Careful inspection of a high magnification image of a typical nanoparticle (Figure 3.1C) from the sample with an 10 at.% excess Ni ($Ti_{0.1}Zr_{0.9}Ni_{1.1}Sn$), reveals that the precipitates are single crystalline spherical particles with average diameter of ~29 nm. No noticeable strain was observed at the phase boundary between the particle and the HH matrix. The absence of strained domains at the matrix/ inclusion interface suggests close structural relationships (e.g. similarity in the lattice constant) between both phases as well as a high level of coherency between lattice planes in both crystals. High magnification TEM images of a portion of the HH matrix (Figure 3.1 C and D) showed its excellent crystallinity with lattice parameter of ~ 0.62 nm and selected-area electron diffraction pattern (Figure 3.1 D, inset of D) confirmed that it is *fcc* structure. Therefore, we predict based on the above structural details as well as on the chemical equation (1) that the observed precipitates are full-Heusler nanodots (quantum dots). Observation of spherical shaped FH nanodots and their high lattice coherency with the HH matrix suggests a co-nucleation and growth of both HH and FH seed crystals during the solid-state reaction from the mixture of elemental powers. Under this synthesis condition, high similarity in the composition and atomic arrangement within the HH and FH structures favors competing formation of the two phases. Therefore, the composition and structure (FH or HH) of seed crystals nucleating at various locations within the reaction mixture depend on the local stoichiometry (Zr:Ti:Ni:Sn ratio). The volume fraction of seed crystals with FH structure and

composition depend on the amount of excess Ni (x) used in the starting mixture. Because only a small excess of Ni (x = 2%, 4% and 10%) was used in this study, the largest fraction of seed crystals nucleating in the reaction mixture are of HH structure. Therefore, large grains with HH structure containing small domains with FH structure coherently embedded in the HH grain are expected. The formation of such HH/FH composites grains likely arises from the merging of several neighboring seed crystals with HH composition and structure surrounding a small fraction of seed crystals with FH composition and structure. This growth mechanism is facilitated by the three dimensional structural similarity between the FH and HH structure which also favors endotaxial growth of spherically shaped FH inclusions within the HH matrix leading to the formation of coherent HH/FH interfaces within the composites. This formation mechanism is consistent with the characteristics of the precipitates observed from TEM studies. The final size and dispersion of the FH inclusions within individual grain of the polycrystalline powder of HH/FH composite strongly depend on the population density of FH seed crystals as well as their proximity within the reaction mixture. Because of the relatively facile interchange between HH and FH structures through solid state Ni diffusion into available vacant sites of the HH structure, the concentration gradient of Ni atoms between FH seed crystals and the surrounding HH crystals as well as the large number of available vacant sites in the HH crystals is likely the driving force for Ni diffusion within individual grains of the HH/FH composite. Through this Ni diffusion process, small unstable FH seed crystals within an individual grain of the HH/FH composites, separated by relatively short distances, can migrate and merge into larger and more stable FH particles (Figure 3.1B). This co-nucleation and growth mechanism can therefore lead to HH/FH composite grains in which FH inclusions with sizes as small as 2nm to 3nm (3 to 5 unit cells of FH) are coherently integrated within the surrounding HH matrix. The resulting

highly coherent atomic-scale phase boundaries between the HH matrix and the FH inclusion allow a close crystallographic registry between both structures. These coherent phase boundaries between the matrix and inclusion phases (Figure 3.1C) are expected to promote the transfer of charge carriers across the matrix/inclusion interfaces.

3.3.2 Electronic Transports in Quantum Dot Engineered HH Semiconductors

3.3.2.1 Carrier Density

Figure 3.2A to D show the high temperature electronic transport properties of $Ti_{0.1}Zr_{0.9}NiSn$ (HH) materials containing various mole fractions of the FH nanostructures embedded within the HH matrix. At 300K, the density of charge carriers in the $Ti_{0.1}Zr_{0.9}NiSn$ (HH) matrix is ~ 6 × $10^{19}/cm^3$ (Figure 3.2A). This value of the carrier density decreases to ~5.2× $10^{19}/cm^3$ at 300K, upon addition of 2 at.% excess elemental Ni in the starting mixture, which corresponds to the formation of $Ti_{0.1}Zr_{0.9}Ni_{1.02}Sn$ bulk nanocomposite containing 98 mol % HH and 2 mol % FH (98%HH/2%FH) according to eq 1. Increasing the excess of elemental Ni to 4 at.% results in a larger decrease of the carrier density (57%) at 300K within the corresponding 96%HH/4%FH nanocomposites. In the 90%HH/10%FH, a 70% reduction in the carrier density is observed at 300 K when compared to that of the pristine of $Ti_{0.1}Zr_{0.9}NiSn$ (HH) matrix. Careful analysis of temperature dependent carrier density curves for various $Ti_{0.1}Zr_{0.9}Ni_{1+x}Sn$ (HH(1-x)/FH(x)) nanocomposites revealed some difference in their shape. For the nanostructure-free composition (x = 0), the carrier density remains almost constant up to 550 K. This behavior is typical for extrinsic semiconductors. As the content of FH nanoinclusion increases, the carrier density becomes progressively more temperature dependent. It should be noted that, regardless of the temperature, the carrier density within the (HH(1-x)/FH(x)) remains lower or equal to the $Ti_{0.1}Zr_{0.9}NiSn$ (HH) matrix carrier density. Although the gradual increase in the carrier density

with temperature observed for the (HH(1-x)/FH(x)) nanocomposites is similar to the behavior typically expected for doped semiconductors, the fact that the overall carrier density within the HH(1-x)/FH(x)) nanocomposites at a given temperature remains lower than that of the $Ti_{0.1}Zr_{0.9}NiSn$ (HH) matrix indicates that no additional carriers were added to the existing ensemble of carriers within the $Ti_{0.1}Zr_{0.9}NiSn$ (HH) matrix upon embedding the FH nanostructures. Such reductions in the carrier concentration of the HH/FH composite could be associated with a gradual increase in the band gap of the HH matrix with increasing FH content. However, this simple explanation is not consistent with the thermopower data in which the gradual decrease in the temperature of maximum thermopower with increasing FH content suggests a reduction in the band gap of the HH matrix (Figure 3.2B). Therefore, the traditional doping concept is not applicable in this system and an alternative mechanism that accurately describes the observed data must be explored.

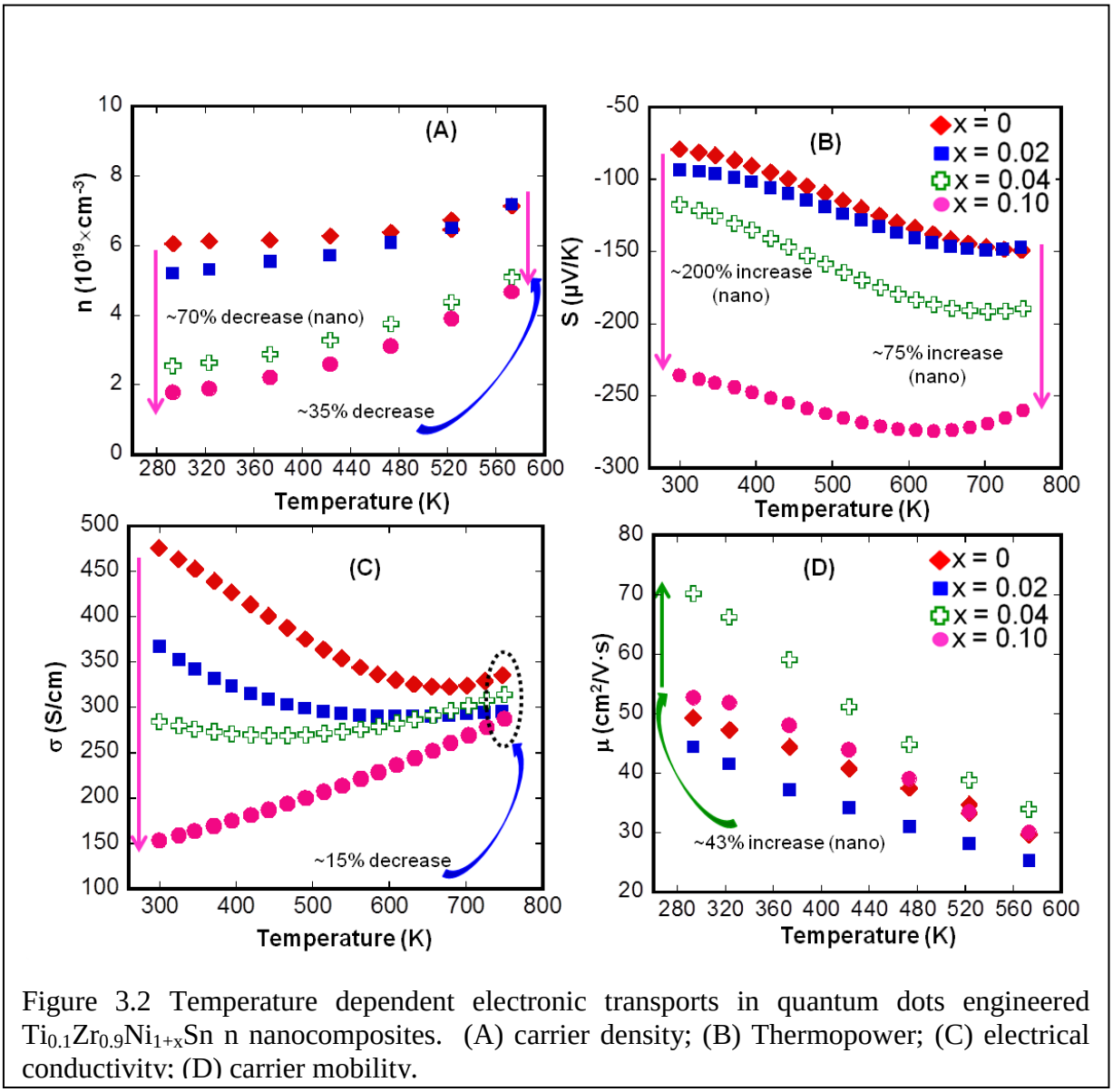

Figure 3.2 Temperature dependent electronic transports in quantum dots engineered $Ti_{0.1}Zr_{0.9}Ni_{1+x}Sn$ n nanocomposites. (A) carrier density; (B) Thermopower; (C) electrical conductivity; (D) carrier mobility.

The systematic gradual decrease in the carrier density in $Ti_{0.1}Zr_{0.9}Ni_{1+x}Sn$ (HH(1-x)/FH(x)) nanocomposites with increasing mole fraction of the FH phase is quite surprising. It is well known that the introduction of large metallic inhomogeneities such as full-Heusler (FH) phases into a semiconductor such as the half-Heusler (HH) alloys generally lead to electronic doping of the semiconducting HH matrix by the FH inclusion phase resulting in drastic increases in the carrier density . However, the observed decrease in the carrier density in $Ti_{0.1}Zr_{0.9}Ni_{1+x}Sn$

(HH(1-x)/FH(x)) nanocomposites with increasing mole fraction of FH inclusions is consistent with our recent results from the Bi-doped HH(1-x)/FH(x) ($0 \leq x \leq 0.1$) (HH = $Zr_{0.25}Hf_{0.75}NiSn_{0.975}Bi_{0.025}$) systems . Drop in the carrier density with the increasing FH content in Bi-doped HH(1-x)/FH(x) ($0 \leq x \leq 0.1$) was ascribed to the formation of energy barriers, ΔE, at the HH-matrix/FH-inclusion interfaces, which act as an energy filter for conduction electrons within the HH matrix[7] . Here, we use a similar mechanism to rationalize the electronic transport data observed in $Ti_{0.1}Zr_{0.9}Ni_{1+x}Sn$ nanocomposites. The gradual increase in the carrier density with temperature observed in the HH(1-x)/FH(x)) nanocomposites can be associated with some forms of charge carriers "culling" within the conduction band (CB) of the $Ti_{0.1}Zr_{0.9}NiSn$ (HH) matrix, based on their relative energy distribution (e.g. low energy carrier versus high energy carrier), using the embedded FH nanostructures.

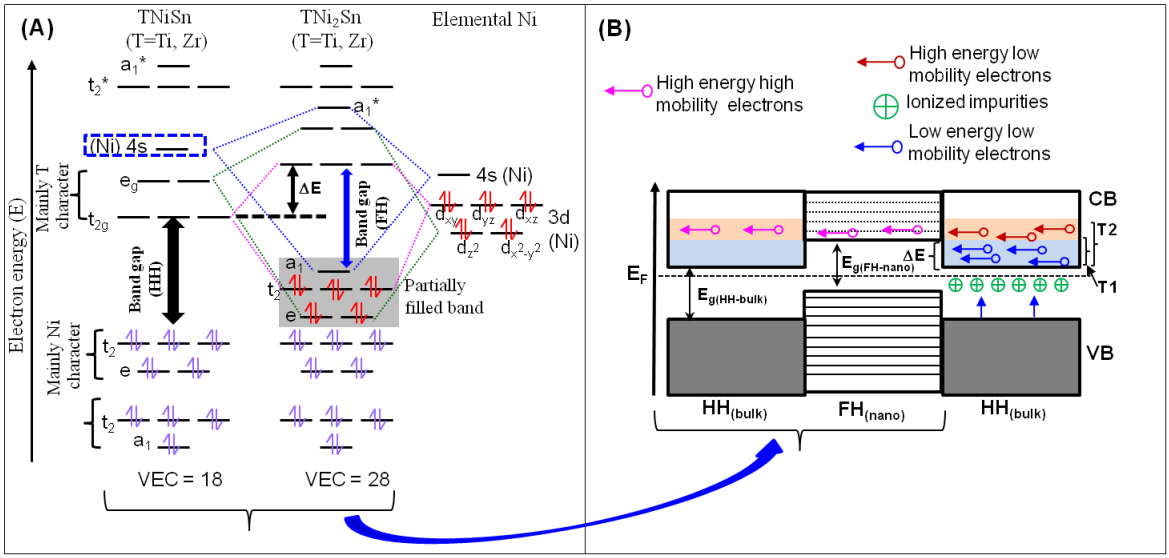

Figure 3.3 Illustrations of the HH and FH band structures alignment at the HH/FH interfaces. (A) Molecular orbital diagram of full-Heusler (TNi_2Sn) generated from that of half-Heusler phase (TNiSn) upon insertion of elemental Ni into vacant tetrahedral site. Comparison of the HH and FH molecular orbital diagrams reveals energy offset of both the valence band maxima (VBM) and the conduction band minima (CBM) leading to nanometer scale type-II (staggered gap) heterojunctions at the HH/FH interface. The conduction band energy offset, ΔE, acts as an energy filter for conduction electrons within the HH matrix. (B) Proposed mechanism of the filtering of low energy electrons (from CB of HH) at the potential barrier, ΔE, (reducing effective carrier density) and spatial separation of high-energy electrons (within CB of FH) from ionized-impurities at nanometer scale HH/FH heterojunctions. Cyan and orange colors represent distributions of low and high-energy electrons at temperatures T1 and T2 (T2 > T1) within the CB of the HH matrix.

As depicted in Figure 3.3A, the band structure of the FH phase is related to that of the HH phase with similar chemical composition and only differs by the presence of a partially filled band with Ni character on top of the FH valence band (VB). This additional partially filled band pushes the valence band maxima (VBM) and the conduction band minima (CBM) of the FH inclusion to higher energy compared to that of the corresponding HH phase. Therefore, one can anticipate the formation of a type-II (staggered gap) heterojunctions at the nanometer scale HH/FH interfaces within the $Ti_{0.1}Zr_{0.9}Ni_{1+x}Sn$ (HH(1-x)/FH(x)) nanocomposites (Figure 3.4B).

The energy offset, ΔE, between CBM in both the HH and FH phases acts as an energy filter for conduction electrons within the CB of the HH matrix. The heights of the energy barrier, ΔE, depends on the position of the CBM of the FH inclusion, which in turn, under quantum confinement regime, depends on the size of the FH nanoinclusion. Therefore, the relative reductions in carrier density measured in various $Ti_{0.1}Zr_{0.9}Ni_{1+x}Sn$ (HH(1-x)/FH(x)) nanocomposites at 300 K correspond to the fraction of low energy conduction electrons from the CB of the HH matrix trapped by the potential barrier, ΔE, at the HH/FH interfaces. The gradual increase in the carrier density with temperature observed in $Ti_{0.1}Zr_{0.9}Ni_{1+x}Sn$ (HH(1-x)/FH(x)) nanocomposites can thus be attributed to "low energy"(LE) carriers, which are trapped at the energy barrier around 300K, gradually overcoming the ΔE potential barrier due to thermal excitation. The fraction of LE electrons trapped by the potential barrier increases with the population density of HH/FH interfaces within the $Ti_{0.1}Zr_{0.9}Ni_{1+x}Sn$ (HH(1-x)/FH(x)) nanocomposites, but also decreases with increasing size of FH nanostructures (decreasing ΔE). Under our synthesis conditions, increasing the percentage of excess elemental Ni atoms in the starting compositions can lead to the formation of: (1) a large number of small FH quantum dots with narrow size distribution or (2) a mixture of small and large FH quantum dots. This explains the observed irregularities in the drops of carrier density within the $Ti_{0.1}Zr_{0.9}Ni_{1+x}Sn$ (HH(1-x)/FH(x)) nanocomposites when going from the 4 at.% excess elemental Ni to the compositions with 10 at.% excess Ni (Figure 3.2A).

3.3.2.2 Thermopower

The above described FH quantum dots induce changes in the effective carrier density within the $Ti_{0.1}Zr_{0.9}NiSn$ (HH) matrix as well as their temperature dependence, are also expected to result in large alterations of the thermopower of $Ti_{0.1}Zr_{0.9}Ni_{1+x}Sn$ (HH(1-x)/FH(x)) nanocomposites

(Figure 3.2B). All $Ti_{0.1}Zr_{0.9}Ni_{1+x}Sn$ (HH(1-x)/FH(x)) nanocomposites showed negative values of the thermopower in the measured temperature range, suggesting electrons as the majority charge carriers. At 300 K, the thermopower values of $Ti_{0.1}Zr_{0.9}Ni_{1+x}Sn$ nanocomposites increase from -78 μV/K (for x = 0) to -94 μV/K (for x = 0.02). This corresponds to about 20% increase in the thermopower of HH(98%)/FH(2%) nanocomposite compared to the $Ti_{0.1}Zr_{0.9}NiSn$ (HH) matrix. The room temperature values of the thermopower further increase to -118 μV/K (for x = 0.04) and -235 μV/K (for x = 0.1), which correspond to ~50% and ~200% enhancements, respectively, when compared to the thermopower value of the $Ti_{0.1}Zr_{0.9}NiSn$ (HH) matrix at 300K. Regardless of the composition, the absolute values of the thermopower of $Ti_{0.1}Zr_{0.9}Ni_{1+x}Sn$ nanocomposites increase with rising temperature, reaching maximum values at 775K (x = 0), 700K (x = 0.04), and 600K (x = 0.1) and slowly decrease thereafter with further increase in temperature. Although the observed increase in the thermopower with increasing mole fraction of FH content seems to be consistent with the decreasing carrier density, the decrease in the temperature of maximum thermopower of the $Ti_{0.1}Zr_{0.9}Ni_{1+x}Sn$ nanocomposites with increasing FH content suggest a decrease in the band gap which should normally lead to a increase in the carrier density. In addition, careful examination of both the temperature dependent carrier density (Figure 3.2A) and thermopower (Figure 3.2B) plots revealed anomalous changes in the magnitude of thermopower upon altering the carrier density within the $Ti_{0.1}Zr_{0.9}Ni_{1+x}Sn$ (HH(1-x)/FH(x)) nanocomposites using FH quantum dots. For instance, the thermopower value of HH(90%)/FH(10%) nanocomposite (x = 0.1) at 300K is twice that of the HH(96%)/FH(4%) nanocomposite, despite their very similar carrier density. This behavior is maintained regardless of the temperature. Also, it is observed that the thermopower value of the HH(98%)/FH(2%)

nanocomposite at 700K is almost equal to that of the $Ti_{0.1}Zr_{0.9}NiSn$ (HH) matrix despite the noticeable difference in their carrier density at the same temperature.

To fully understand these surprising changes in the thermopower upon alteration of the effective carrier density of the $Ti_{0.1}Zr_{0.9}Ni_{1+x}Sn$ (HH(1-x)/FH(x)) nanocomposites using FH quantum dots, we have constructed Pisarenko plots describing the relationship between the thermopower and carrier density for each of the $Ti_{0.1}Zr_{0.9}Ni_{1+x}Sn$ (HH(1-x)/FH(x)) nanocomposites, $S = [(8\pi^2(k_B)^2)/3eh^2]m^*T(\pi/3n)^{2/3}$ (k_B is the Boltzmann constant, e is the carrier charge, h is the Planck's constant, m^* is the effective mass of the charge carrier, T is the absolute temperature, n is the carrier concentration), assuming parabolic bands and an energy independent relaxation time[94] (Figure 3.4A) . Under these assumptions, the thermopower at a given temperature can be described by a unique value of the effective mass (m*). Figure 3.4A shows the Pisarenko plots (*S* versus *n*) at 300K for various $Ti_{0.1}Zr_{0.9}Ni_{1+x}Sn$ (HH(1-x)/FH(x)) nanocomposites. No single value of the effective mass that allows fitting of all the data could be obtained, suggesting that the embedded FH quantum dots, in addition to reducing the effective carrier density within the $Ti_{0.1}Zr_{0.9}NiSn$ (HH) matrix, also significantly alter its electronic band structure close to the Fermi level. This is confirmed by large variations in the carrier effective mass (m*) values extracted from the fitting of S(n) curves under the approximation of the parabolic bands and an energy independent relaxation time for each $Ti_{0.1}Zr_{0.9}Ni_{1+x}Sn$ (HH(1-x)/FH(x)) nanocomposite. At 300K, the values of the effective mass are m* = 0.6, 0.62, 0.5 and 0.8 for $Ti_{0.1}Zr_{0.9}Ni_{1+x}Sn$ (HH(1-x)/FH(x)) nanocomposite with x = 0, 0.02, 0.04 and 0.1, respectively (Figure 3.4A). The observed changes in the carrier effective mass (m*) with increasing mole fraction of FH quantum dots in the $Ti_{0.1}Zr_{0.9}NiSn$ (HH) matrix, explain very well

the large difference between the thermopower values of the HH(90%)/FH(10%) (x = 0.1) and HH(96%)/FH(4%) (x = 0.04) nanocomposites, despite their very similar carrier density.

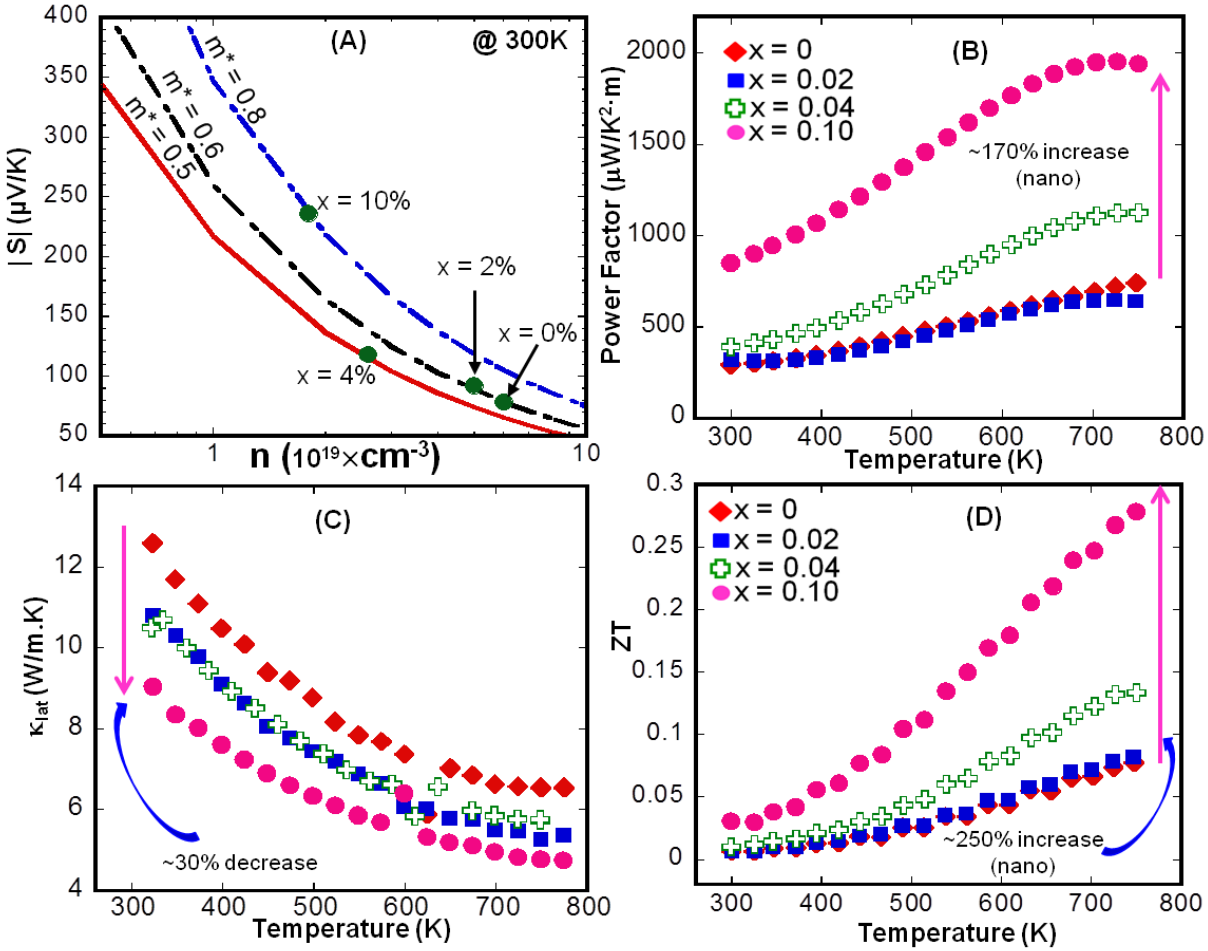

Figure 3.4 Pisarenko plot and temperature dependence of the thermoelectric performance of $Ti_{0.1}Zr_{0.9}Ni_{1+x}Sn$ nanocomposites. (A) Pisarenko plot showing large enhancements of the thermopower (S) due to simultaneous decrease in carrier concentration and increase in the carrier effective mass (m*) with increasing excess Ni. Temperature dependent (B) Power factor; (C) Lattice thermal conductivity; and (D) thermoelectric figure of merit (ZT) of HH(1-x)/FH(x) bulk nanocomposites (x= 0; 0.02; 0.04; 0.1).

An increase in the effective mass is generally associated with an increase in the energy band gap, E_g [95]. Indeed, the plot of the temperature dependent carrier density of various $Ti_{0.1}Zr_{0.9}Ni_{1+x}Sn$ (HH(1-x)/FH(x)) nanocomposites suggests the presence of a potential barrier (ΔE) at the HH/FH

interfaces and the trapped electrons must know gained sufficient energy to overcome this barrier in order to participate to the electrical conduction. The addition of the potential barrier ΔE corresponds to an increase in the band gap of the HH/QD nanocomposites compared to the HH matrix, since an electron from the valence band (VB) of the HH matrix will now need higher thermal energy to overcome both the intrinsic energy gap (E_g) of the pristine HH matrix and the added potential barrier (ΔE), in order to participate to the electrical conduction. Therefore, the "apparent" band gap of the HH/QD nanocomposite can be expressed as $E_{g(HH/QD)} = E_{(CBM-QD)} - E_{(VBM-HH)} = E_{g(HH)} + \Delta E$ (where $E_{(CBM-QD)}$ and $E_{(VBM-HH)}$ are the energies of the conduction band minima for the FH QD and the valence band maxima for the HH matrix. Noting that the decrease in the thermopower of various $Ti_{0.1}Zr_{0.9}Ni_{1+x}Sn$ nanocomposites at high temperatures can be ascribed to electron-hole compensation arising from thermal excitation of electrons from the valence band (VB) to the conduction band (CB) of the HH matrix, a reduction in the temperature of maximum thermopower of $Ti_{0.1}Zr_{0.9}Ni_{1+x}Sn$ nanocomposites with increasing FH content suggests a reduction in the band gap, which not in alignment with the observed change in the carrier density. One possible explanation of this anomalous behavior can be obtained by considering thermal excitation of electrons from the VB to the CB within the FH inclusions occur and at lower temperature as the size of the FH inclusion increases. For instance, an increase in the excess of elemental Ni in the HH matrix can result in the formation of a large number of FH inclusions with a slightly larger average size. The increase in the size of the FH inclusions corresponds to a decrease in the band gap of the FH inclusion and therefore reduction in the energy required to excite electrons from the VB to the CB of FH.

From the analysis above, one can conclude that embedding FH quantum dots into a semiconducting HH matrix, results in a new material with distinct electronic band structure,

when compared to that of the HH matrix. This means that the embedded FH quantum dots become an integral part of the atomic structure of the HH matrix. This is consistent with the absence of FH diffraction peaks in the XRD patterns of the synthesized HH(1-x)/FH(x) material (Figure 3.1A). The electronic characteristics (e.g. band gap, carrier density and carrier effective mass) of the resulting HH(1-x)/FH(x) material strongly depend on the mole fraction, average size and distribution for FH quantum dots within the semiconducting HH matrix. The drastic positive changes in the electronic properties (S, n and m*) of the bulk HH matrix associated with the atomic-scale integration of FH quantum dots, sharply discriminate this novel method of enhancing the electronic transport of a bulk semiconducting matrix from the traditional doping strategy where the alteration of carrier density generally maintains the carrier effective mass more or less constant. The ability to simultaneously decrease the carrier density and increase the carrier effective mass within the $Ti_{0.1}Zr_{0.9}NiSn$ (HH) matrix, using FH quantum dots lead to thermopower enhancements superior in magnitude compared to values expected from similar alteration in the carrier density using simple doping methods (Figure 3.4A).

3.3.2.3 Carrier Mobility

The mobility of charge carriers, in a conventional semiconductor is related to the relaxation time, τ, between scattering events (phonon-electron scattering, ionized-impurity scattering and electron – electron scattering, etc.) and the carrier effective mass (m^*) by the equation $\mu = e(\tau/m^*)$. Therefore, the above described alteration of the effective mass of the HH matrix upon embedding the FH quantum dots is expected to significantly alter the carrier mobility within the resulting $Ti_{0.1}Zr_{0.9}Ni_{1+x}Sn$ (HH(1-x)/FH(x)) nanocomposites (Figure 3.2D). Assuming constant relaxation time, τ, the carrier mobility μ_i in various $Ti_{0.1}Zr_{0.9}Ni_{1+x}Sn$ (HH(1-x)/FH(x)) nanocomposites can be related to the carrier mobility μ_0 in the HH matrix by the simple relation

$\mu_i = \mu_0 (m^*_0/m^*_i)$ (m^*_0 is the carrier effective mass in the HH matrix and m^*_i is the carrier effective mass in a given (HH(1-x)/FH(x)) nanocomposite). At 300K, the carrier mobility slightly decreases from $\mu_0 = 50$ cm^2/V·s for the $Ti_{0.1}Zr_{0.9}NiSn$ (HH) matrix to $\mu_i = 45$ cm^2/V·s for the HH(98%)/FH(2%) nanocomposite. This 10% reduction in the mobility can be associated with the small increase in the carrier effective mass in the HH(98%)/FH(2%) sample, assuming a constant relaxation time, τ. Upon increasing the mole fraction of FH quantum dots to x = 0.04, the carrier mobility in the resulting HH(96%)/FH(4%) nanocomposite drastically increases to 70 cm^2/V·s. The observed carrier mobility is 16% larger than the value $\mu_i = 60$ cm^2/V·s expected for constant relaxation approximation. Therefore, the observed large increase in the carrier mobility within the HH(96%)/FH(4%) nanocomposite can be attributed to both an increase in the relaxation time and a reduction in the carrier effective mass (Figure 3.4A). Further increase in the mole fraction of FH quantum dots to x = 0.1 results in a reduction of the room temperature value of the carrier mobility to 53 cm^2/V·s due to a large increase in the carrier effective mass (m* = 0.8). However, the observed carrier mobility in the HH(90%)/FH(10%) nanocomposite is still 41% higher than the $\mu_i = 37.5$ cm^2/V·s value expected from constant relaxation time approximation, suggesting a large increase in the relaxation time (τ), simultaneously with the increase in the effective mass within the HH(90%)/FH(10%) nanocomposite. The carrier mobility in all $Ti_{0.1}Zr_{0.9}Ni_{1+x}Sn$ (HH(1-x)/FH(x)) nanocomposites decreases almost linearly with rising temperature. An increase in the relaxation time within the $Ti_{0.1}Zr_{0.9}Ni_{1+x}Sn$ (HH(1-x)/FH(x)) nanocomposites can be attributed to the drop in the effective carrier density arising from the trapping at 300K, of low energy carriers by the potential barrier, $\triangle$E at the HH/FH interfaces (Figure 3.3B). Such reduction in the effective carrier density implies a reduction in the frequency of electron-electron collisions leading to a larger relaxation time between scattering

events. However, this reduction in the frequency of electron-electron collisions alone does not explain why the observed carrier mobility within the HH(90%)/FH(10%) nanocomposite is 41% larger than the expected value, whereas in the HH(96%)/FH(4%) nanocomposite, the observed carrier mobility is only 16% higher than the expected value, although both HH(90%)/FH(10%) and HH(96%)/FH(4%) nanocomposites have similar carrier densities. This suggests that additional contributing factors such as charge carrier – ionized impurity scattering and charge carrier scattering by structural defects (dislocations, vacancies) play a significant role in the alteration of the relaxation time within $Ti_{0.1}Zr_{0.9}Ni_{1+x}Sn$ (HH(1-x)/FH(x)) nanocomposites.

3.3.2.4 Electrical Conductivity

The above described alterations of the magnitude and the temperature dependence of carrier density and mobility within the bulk semiconducting $Ti_{0.1}Zr_{0.9}NiSn$ (HH) matrix induced by coherently embedded FH quantum dots inside its atomic structure, drastically change the semiconducting behavior of the $Ti_{0.1}Zr_{0.9}Ni_{1+x}Sn$ (HH(1-x)/FH(x)) nanocomposites. For instance, the electrical conductivity of the $Ti_{0.1}Zr_{0.9}NiSn$ (HH) matrix decreases with rising temperature from 480 S/cm at 300K, reaches a minimum of 320 S/cm at 680K and increases thereafter with further increase in temperature (Figure 3.2C). This behavior is typical of heavily doped semiconductors in which intrinsic excitations set in at higher temperature, above about 650 K in this case. A similar trend is observed in HH(98%)/FH(2%) and HH(96%)/FH(4%) samples except that the minima in the conductivity occur at lower temperatures of 580 K and 450 K, respectively. The HH(90%)/FH(10%) nanocomposite displays the intrinsic-like semiconducting behavior (σ rises with T) in the entire temperature range measured. This indicates that the nature of the carrier transport in $Ti_{0.1}Zr_{0.9}Ni_{1+x}Sn$ (HH(1-x)/FH(x)) nanocomposites change from that of a heavily, extrinsic-doped semiconductor to an intrinsic semiconductor-like behavior with the

increasing mole fraction of FH quantum dots in the $Ti_{0.1}Zr_{0.9}NiSn$ (HH) matrix. At room temperature, as a function of FH content, the electrical conductivity decreases from 480 S/cm to 370 S/cm, to 280 S/cm, and finally to 150 S/cm for 0, 2%, 4%, and 10% FH concentrations in the HH matrix, respectively. The observed drop in the electrical conductivity of $Ti_{0.1}Zr_{0.9}Ni_{1+x}Sn$ (HH(1-x)/FH(x)) nanocomposites at 300 K with the increasing mole fraction of FH quantum dots can be rationalized by the large decrease in the carrier density (Figure 3.2A). This gradual change of the conducting behavior towards an intrinsic" semiconductor-like regime with the increasing mole fraction of the FH quantum dots, suggests a gradual increase in the energy band gap (E_g) of the $Ti_{0.1}Zr_{0.9}Ni_{1+x}Sn$ (HH(1-x)/FH(x)) nanocomposites. The apparent increase in the energy band gap of $Ti_{0.1}Zr_{0.9}Ni_{1+x}Sn$ (HH(1-x)/FH(x)) nanocomposites and the observed changes in the carrier effective mass strongly point to profound alteration of the electronic band structure of the $Ti_{0.1}Zr_{0.9}NiSn$ (HH) matrix by the embedded FH quantum dots leading to a new and fundamentally distinct material. The observed fast increase in the electrical conductivity of $Ti_{0.1}Zr_{0.9}Ni_{1+x}Sn$ (HH(1-x)/FH(x)) nanocomposites with temperature results from the nearly exponential increase in the carrier density and the linear decrease in the mobility with increasing temperature. This temperature dependence of the carrier density and mobility leads to a marginal (15%) decrease in the electrical conductivity of $Ti_{0.1}Zr_{0.9}Ni_{1+x}Sn$ (HH(1-x)/FH(x)) nanocomposites at high temperatures (Figure 3.2D).

3.3.2.5 Power Factor

The large enhancements (up to 200% at 300K) of the thermopower at all temperatures and the observed minimal reduction (15%) in the electrical conductivity at high temperatures discussed above, result in large improvements in the power factor ($PF = \sigma S^2$) of $Ti_{0.1}Zr_{0.9}Ni_{1+x}Sn$ (HH(1-x)/FH(x)) nanocomposites (Figure 3.4B). At 300K, the power factor of the $Ti_{0.1}Zr_{0.9}NiSn$ (HH)

matrix is 300 μW/K^{2}m and slowly increases with temperature to 750 μW/K^{2}m at 780K. Only marginal change in the power factor is observed for the HH(98%)/FH(2%) nanocomposite compared to the $Ti_{0.1}Zr_{0.9}NiSn$ (HH) matrix. Upon increasing the mole fraction of FH quantum dots to 4 mole%, the power factor of the resulting HH(96%)/FH(4%) nanocomposite increases from 390μW/K^{2}m at 300K to 1150 μW/K^{2}m at 780K, which corresponds to ~ 53% increase at 780 K when compared to the $Ti_{0.1}Zr_{0.9}NiSn$ (HH) matrix. The largest enhancement of the power factor was obtained for the HH(90%)/FH(10%) nanocomposite. At 300K, a power factor value of 850μW/K^{2}m was observed. As the temperature increases, the PF of the HH(90%)/FH(10%) nanocomposite rapidly rises to a maximum value of 1960 μW/K^{2}m at 780 K. This represents ~ 160% enhancement when compared to the PF of the $Ti_{0.1}Zr_{0.9}NiSn$ (HH) matrix. This large enhancement of the power factor of the HH(90%)/FH(10%) nanocomposite at 780 K arises from the observed 70% increase in the thermopower and a marginal (15%) decrease in the electrical conductivity.

Another interesting finding in this study is the ability of the embedded FH quantum dots to scatter thermal phonons to reduce the thermal conductivity of the synthesized $Ti_{0.1}Zr_{0.9}Ni_{1+x}Sn$ (HH(1-x)/FH(x)) nanocomposites. Figure 3.5C shows the temperature dependence of the lattice thermal conductivity (κ_L) obtained by subtracting the electronic component κ_e from the total thermal conductivity, κ. $\kappa_e = L_o \sigma T$ was estimated using the Wiedemann-Franz law where the Lorenz number taken as its fully degenerate value of $L_o = 2.45 \times 10^{-8}$ WΩK^{-2}. The lattice thermal conductivities of the $Ti_{0.1}Zr_{0.9}Ni_{1+x}Sn$ (HH(1-x)/FH(x)) nanocomposites at all temperatures decrease with the increasing mole fraction of the FH quantum dots. For instance, the lattice thermal conductivity of the $Ti_{0.1}Zr_{0.9}NiSn$ (HH) matrix at 300K is 12.6 Wm^{-1}K^{-1} and gradually decreases to 9.05 Wm^{-1}K^{-1} for HH(90%)/FH(10%) nanocomposite (Figure 3.4C). This

corresponds to a ~30% reduction in the lattice thermal conductivity at 300K. Regardless of the composition, the lattice thermal conductivity monotonically decreases with increasing temperature (Figure 3.4C). At 775 K, the lattice thermal conductivity of $Ti_{0.1}Zr_{0.9}NiSn$ (HH) matrix decreases down to 6.56 $Wm^{-1}K^{-1}$ whereas that of the HH(90%)/FH(10%) nanocomposite drops to 4.75 $Wm^{-1}K^{-1}$, which corresponds to a 23% reduction when compared to that of the HH matrix (Figure 3.4C). The observed reductions in the thermal conductivities of the $Ti_{0.1}Zr_{0.9}Ni_{1+x}Sn$ (HH(1-x)/FH(x)) nanocomposites are attributed to the enhancement of thermal phonons scattering by the multiple nanometer scale HH/FH phase boundaries introduced by the insertion of FH quantum dots within the HH matrix, in addition to the mid- to long-wavelength phonons scattering at grains boundaries .

The simultaneous large enhancements in the power factor and the associated reductions in the lattice thermal conductivity of $Ti_{0.1}Zr_{0.9}Ni_{1+x}Sn$ (HH(1-x)/FH(x)) nanocomposites, result in drastic improvements in their thermoelectric figure of merit ZT when compared to the $Ti_{0.1}Zr_{0.9}NiSn$ (HH) matrix (Figure 3.4D). For instance, starting with a semiconducting $Ti_{0.1}Zr_{0.9}NiSn$ (HH) matrix with ZT ~ 0.08 at 775K, we found that coherent integration of 10 mole% of FH quantum dots within the crystal lattice of the semiconducting HH matrix dramatically enhances the thermoelectric performance of the resulting HH(90%)/FH(10%) nanocomposite to ZT~0.28 at 775K, a factor of 3.5 times higher ZT as compared to the $Ti_{0.1}Zr_{0.9}NiSn$ (HH) matrix.

3. 3 Conclusion

In summary, we found that quantum dots coherently embedded within a semiconducting matrix, tailor the electronic behavior of existing ensembles of charge carriers within the matrix, leading to a spectacular increase in the thermopower as well as a large enhancement in the carrier mobility within the resulting bulk nanocomposite. One plausible rationalization of the observed data can be obtained by considering that the embedded quantum dot forms a potential barrier at the matrix/ quantum dot interface due to the offset of their conduction band minima (CBM). This potential barrier, the height of which increases with the decreasing size of the QD, discriminates existing charge carriers from the conduction band of the matrix with respect to their relative energy. Therefore, carriers with energy higher than the potential barrier height (High energy carriers) are transmitted to the CB of the QD whereas carriers with energy lower than the potential barrier height are trapped at the matrix/QD interface and require additional thermal energy to cross the potential barrier. The above described charge carrier culling results in a reduction of the effective carrier density within the matrix at all temperatures and in their strong temperature dependence. Furthermore, the addition of a potential barrier at the matrix/QD interface induces an apparent increase in the band gap of the HH/FH-QD nanocomposites leading to larger carrier effective mass .The simultaneous decrease in the carrier density and the increase in the carrier effective mass within the HH/FH-QD nanocomposites yield a drastic enhancement of their thermopower without a significant alteration of the electrical conductivity. The marginal decrease in the electrical conductivity is associated with an increase in the carrier mobility arising presumably from a large increase in the carrier scattering relaxation time which compensates for the increase in the carrier effective mass. The above results evidently demonstrate that atomic-scale crystal structure engineering of a semiconductor matrix using

endotaxially embedded quantum dots drastically enhances the thermopower and carrier mobility in the composite material. The discovery of this novel approach to enhance thermopower and carrier mobility is expected to pave the way towards larger figures of merit in thermoelectric materials intended for high performance energy conversion application.

CHAPTER 4

ELECTRONIC AND PHONON TRANSPORTS IN Sb-DOPED $Ti_{0.1}Zr_{0.9}Ni_{1+X}Sn_{0.975}Sb_{0.025}$ NANOCOMPOSITES

4.1 Objective

In this work, we explore the effect of the HH/FH interfacial potential, ΔE, on the electronic transport in heavily doped $Ti_{0.1}Zr_{0.9}Ni_{1+x}Sn_{0.975}Sb_{0.025}$ (x = 0, 0.02, 0.04, 0.1) nanocomposites. The formation of the FH nanoinclusions within the HH matrix was confirmed by high-resolution transmission electron microscopy (HRTEM) studies. We found that the substitution of Sn by 2.5% Sb results in large increases of the carrier density from ~6×10^{19} cm^{-3} ($Ti_{0.1}Zr_{0.9}NiSn$) to ~6×10^{20} cm^{-3} ($Ti_{0.1}Zr_{0.9}NiSn_{0.975}Sb_{0.025}$). The formation FH precipitates in the Sb-doped $Ti_{0.1}Zr_{0.9}NiSn_{0.975}Sb_{0.025}$ matrix maintains the carrier density nearly constant for composition with x= 0.02 and 0.04 where a large fraction of the FH inclusions are small (< 20 nm) and well dispersed, whereas the clustering for FH inclusions into large particles (20 nm to 100 nm) in the sample with x = 0.1, resulted in a large increase of the carrier density to ~9×10^{20} cm^{-3}. Surprisingly, only a marginal change is observed on the thermopower and electrical conductivity of all $Ti_{0.1}Zr_{0.9}Ni_{1+x}Sn_{0.975}Sb_{0.025}$ (x = 0, 0.02, 0.04, 0.1) samples despite the large increase in the carrier density observed for the sample with x = 0.1. It is remarkable to note that the carrier mobility in the samples with x = 0.02 and 0.04 is very similar to the carrier mobility

of the matrix. The observed constant values of the thermopower and electrical conductivity for various $Ti_{0.1}Zr_{0.9}Ni_{1+x}Sn_{0.975}Sb_{0.025}$ (x = 0, 0.02, 0.04, 0.1) samples suggests that nanostructuring through coherent insertion of FH inclusions within the HH matrix does not disrupt electronic transport resulting in a constant power factor (PF) for various samples. Interestingly, a reduction in the thermal conductivity was observed for various nanocomposites when compared to the Sb-doped HH matrix. These results clearly suggest that band engineering through atomic-scale engineering of the structure and chemistry of the matrix-inclusion interfaces is an efficient strategy to achieve large reductions in the thermal conductivity of the semiconducting matrix with minimal disruption of its electronic transports.

4.2 Results and analysis

4.2.1 Crystal structure and microstructure

Careful analysis of the X-ray diffraction patterns (Figure 4.1A) of the synthesized

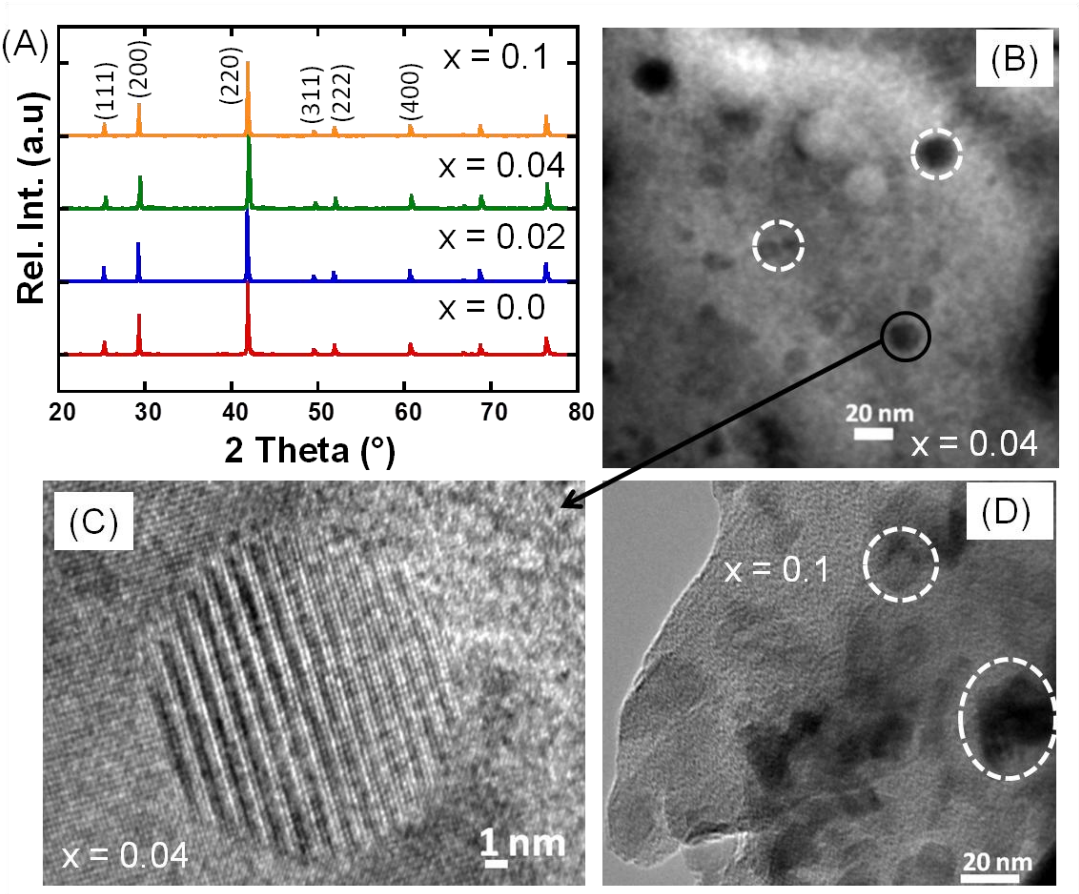

Figure 4.1 Structural characteristic of $Ti_{0.1}Zr_{0.9}Ni_{1+x}Sn_{0.975}Sb_{0.025}$ (x = 0, 0.02, 0.04, 0.1) nanocomposites. (A) Powder X-ray diffraction patterns showing only peaks corresponding to the HH matrix. (B) Low magnification TEM image of the sample with x = 0.04, revealing the presence of spherical FH precipitates embedded in the HH matrix. (C) High magnification image of a typical FH nanostructure from the sample with x = 0.04 showing the highly coherent phase boundary with the surrounding HH matrix. (D) Low magnification TEM image of the sample with x = 0.1 showing high agglomeration of FH nanostructures into large particles.

$Ti_{0.1}Zr_{0.9}Ni_{1+x}Sn_{0.975}Sb_{0.025}$ (x = 0, 0.02, 0.04, 0.1) suggested the formation of single phase HH alloys. All diffraction peaks were indexed in the cubic MgAgAs structure type (space group: *F*-43*m*). No additional peak that could be assigned to the anticipated FH secondary phase or to any

other impurity phase could be observed on the diffractions patterns, even for samples with the expected FH mole fraction of up to 10% (x = 0.1). This suggests that the excess elemental Ni added in the starting mixture is dissolved into interstitial sites in the structure of the HH matrix to form interstitial solid-solution or are located on the vacant (3/4, 3/4, 3/4) site in the HH structure to form FH phases that are too small to strongly diffract X-ray radiation. In the event of the formation of interstitial solid-solution, one should observe a graduate increase in the unit cell parameter of the HH matrix with increasing excess Ni (x value). However, the refinement of the unit cell parameter of the HH phase in various $Ti_{0.1}Zr_{0.9}Ni_{1+x}Sn_{0.975}Sb_{0.025}$ (x = 0, 0.02, 0.04 and 0.1) compositions using diffraction peaks from the XRD patterns showed a constant value (a ~ 6.096(2) Å) for all samples suggesting that interstitial solid-solution between HH and excess elemental Ni is unlikely. To investigate the anticipated formation of small precipitates in various $Ti_{0.1}Zr_{0.9}Ni_{1+x}Sn_{0.975}Sb_{0.025}$ (x = 0.02, 0.04 and 0.1) samples and to characterize their morphology, average size and dispersion, high resolution transmission electron microscopy (HRTEM) study was carried out on selected specimens. A low magnification TEM image of the sample with x = 0.04 is shown in Figure 4.1B. It can be seen clearly that spherical precipitates of the FH phase with size ranging from < 5 nm to 20 nm are well dispersed within the HH matrix. These FH precipitates are coherently embedded within the HH matrix (Figure 4.1C) as no obvious strained domain could be observed at the matrix/ inclusion interface. The spacings between neighboring lattice planes in the HH matrix and FH inclusions are ~ 0.30 nm and ~ 0.32 nm, respectivelt, This indicates a coherent alignment of the (200) planes of the HH matrix and FH inclusions at the matrix/inclusion interfaces. The observed coherent phase boundaries between the matrix and inclusion phases (Figure 4.1C) are expected to promote charge carrier transfer across the matrix/inclusion interfaces. Increasing the concentration of excess Ni to x = 0.1 resulted in the

precipitation and agglomeration of the FH nanophase into large particles with size ranging from 20 nm to 100 nm (Figure 4.1D).

4.2.2 Thermoelectric properties

The temperature dependence of the electronic transport properties of the synthesized $Ti_{0.1}Zr_{0.9}Ni_{1+x}Sn_{0.975}Sb_{0.025}$ (x = 0, 0.02, 0.04, 0.1), HH(1-x)/FH(x) bulk nanocomposites is shown in Figure 4.2. At 300K the carrier density of the Sb-doped $Ti_{0.1}Zr_{0.9}NiSn_{0.975}Sb_{0.025}$ HH matrix is ~ 6.8×10^{20} cm^{-3}, (Figure 4.2A) which corresponds to 870% increase compared to the carrier density measured on the undoped $Ti_{0.1}Zr_{0.9}NiSn$ sample[3] . This is consistent with the expected increase in the density of electrons upon substituting 2.5% Sn by Sb in $Ti_{0.1}Zr_{0.9}NiSn$. The carrier density remains constant in $Ti_{0.1}Zr_{0.9}Ni_{1+x}Sn_{0.975}Sb_{0.025}$ nanocomposites with x = 0.02 (HH(98%)/FH (2%)) and x = 0.04 (HH(96%)/FH(4%)). This suggests that the FH nanostructures incorporated in the HH (98%)/FH (2%) and HH (96%)/FH (4%) samples are not electronically active. However, increasing the concentration of excess Ni to x = 0.1 (HH(90%)/FH(10%)) resulted in a 38% increase (~9.4×10^{20} cm^{-3}) in the carrier density when compared to the Sb-doped matrix. This increase in the carrier density is attributed to electronic doping of the HH matrix by the FH inclusions. Regardless of the x values, the carrier density remains nearly constant with increasing temperature, indicating that the synthesized samples are heavily doped semiconductors.

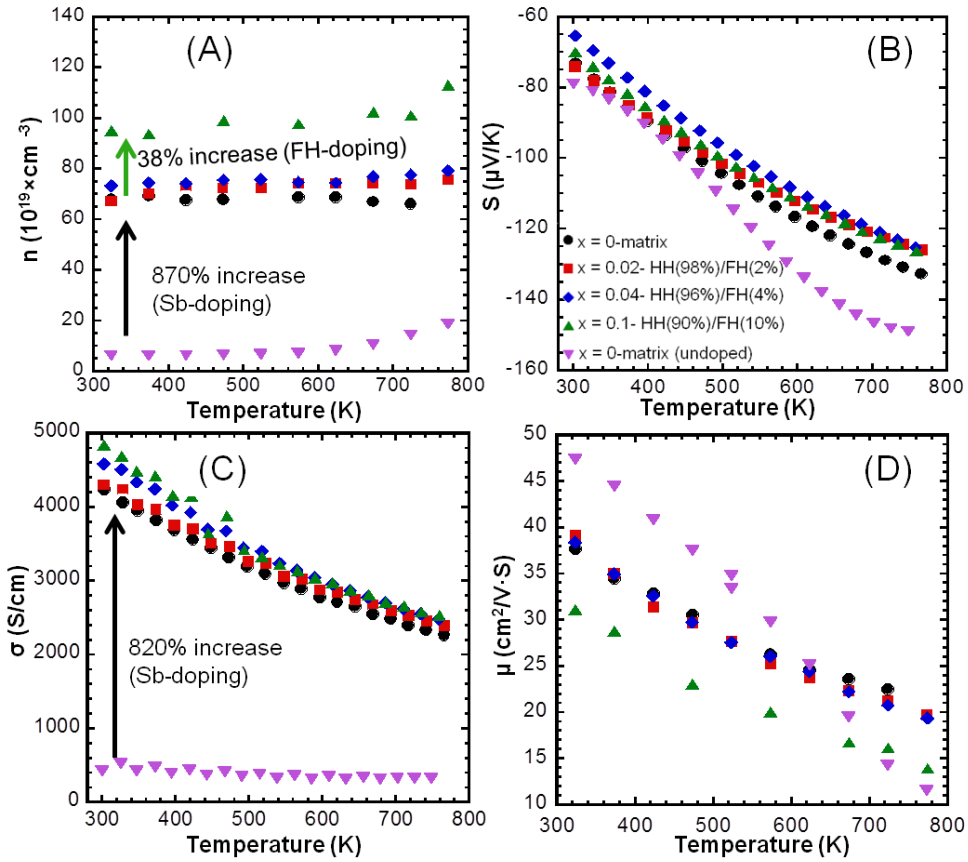

Figure 4.2 Temperature dependence of the electronic transport properties of HH(1-x)/FH(x) bulk nanocomposites (x= 0; 0.02; 0.04; 0.1): (A) thermopower; (B) carrier density; (C) electrical conductivity; (D) carrier mobility.

To better understand the observed difference in the alteration of the carrier density by the FH inclusions in HH(98%)/FH(2%), HH(96%)/FH(4%) and HH(90%)/FH(10%), one must take into consideration the microstructures of various samples. TEM images of the HH(96%)/FH(4%) and (HH(90%)/FH(10%) samples showed that a large fraction of the FH inclusions in HH(96%)/FH(4%) are smaller than 20 nm and are well dispersed, whereas in HH(90%)/FH(10%) sample, the FH inclusions agglomerate in to large particles (Figure 4.1B and 1D). Considering that the FH phase in bulk form is metallic, one would anticipate a gradual increase in the carrier density with increasing mole fraction of FH inclusions in various HH(1-

x)/FH(x) samples due to electronic doping of the semiconducting HH matrix by the FH inclusions. Therefore, the constant carrier density observed in the HH(98%)/FH(2%) and HH(96%)/FH(4%) samples indicates that small (< 20 nm) FH inclusions are likely insulating or semiconducting and upon agglomeration into large (> 20nm) particles (Figure 4.1D), the bulk metallic character of the FH phases is recovered. This analysis is consistent with results from our previous investigations in comparable systems[3-4, 7] .

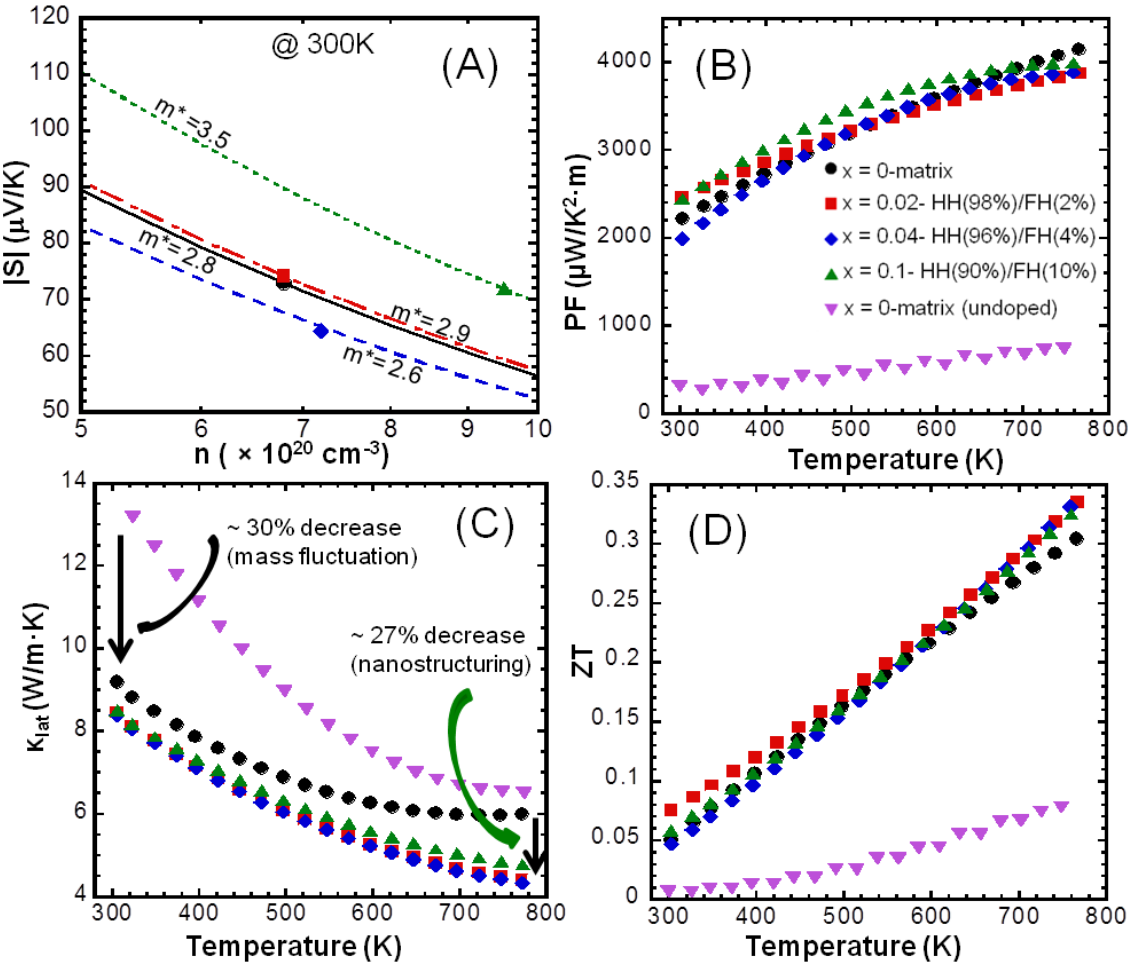

Figure 4.3 Pisarenko plot of $Ti_{0.1}Zr_{0.9}Ni_{1+x}Sn_{0.975}Sb_{0.025}$ at 300K and temperature dependence of the thermoelectric properties of HH(1-x)/FH(x) bulk nanocomposites (x = 0; 0.02; 0.04; 0.1): (A) Pisarenko plot of Ti0.1Zr0.9Ni1+xSn0.975Sb0.025, shows the relationship between the thermopower and carrier density at 300 K; (B) power factor; (C) lattice thermal conductivity; (D) figure of merit (ZT).

Figure 4.2B shows the temperature dependence of the thermopower in the synthesized $Ti_{0.1}Zr_{0.9}Ni_{1+x}Sn_{0.975}Sb_{0.025}$ nanocomposites. All samples show negative values of the thermopower in the whole temperature range indicating n-type semiconducting behavior. At 300K the thermopower of the sample with x = 0 (Sb-doped matrix) is ~ -74 μV/K, which is very similar to the value (~ -78 μV/K) measured for the undoped $Ti_{0.1}Zr_{0.9}NiSn$ matrix . Surprisingly, the thermopower at 300K of various $Ti_{0.1}Zr_{0.9}Ni_{1+x}Sn_{0.975}Sb_{0.025}$ nanocomposites remains nearly constant with increasing x values, despite the 38% increase in the carrier density obtained for the sample with x = 0.1. Regardless of the composition, the absolute values of the thermopower of $Ti_{0.1}Zr_{0.9}Ni_{1+x}Sn_{0.975}Sb_{0.025}$ nanocomposites increase with rising temperature reaching a value of ~-130 μV/K at 775K. The observed similar values of the thermopower of $Ti_{0.1}Zr_{0.9}Ni_{1+x}Sn_{0.975}Sb_{0.025}$ samples despite the difference in the carrier density for the sample with x = 0.1 can be explained by the change in the carrier effective mass (m*). From the Pisarenko plots (Figure 4.3A) describing the relationship between the thermopower and carrier density for each of the $Ti_{0.1}Zr_{0.9}Ni_{1+x}Sn_{0.975}Sb_{0.025}$ samples at 300K, $S = [(8\pi^2(k_B)^2)/3eh^2]m^*T(\pi/3n)^{2/3}$ (k_B is the Boltzmann constant, e is the carrier charge, h is the Planck's constant, m^* is the effective mass of the charge carrier, T is the absolute temperature, n is the carrier density)[94] , we observed that the high carrier density of the sample with x = 0.1 is compensated by an increase in the carrier effective mass $m^* = 3.5\ m_e$.

The temperature dependence of the electrical conductivity of the synthesized $Ti_{0.1}Zr_{0.9}Ni_{1+x}Sn_{0.975}Sb_{0.025}$ nanocomposites is shown in Figure 4.2C. At 300K the $Ti_{0.1}Zr_{0.9}NiSn_{0.975}Sb_{0.025}$ (x = 0) matrix displays a large electrical conductivity, ~4200 S/cm. This corresponds to ~820% increase when compared to the electrical conductivity of undoped $Ti_{0.1}Zr_{0.9}NiSn$ matrix[3] . The observed electrical conductivity is consistent with the large increase

in the carrier density arising from the partial substitution of 2.5% Sn by Sb in $Ti_{0.1}Zr_{0.9}NiSn$. The electrical conductivity decreases with increasing temperature, which is consistent with heavily doped semiconducting behavior. Regardless of the x values (fraction of FH inclusions), the electrical conductivities of all $Ti_{0.1}Zr_{0.9}Ni_{1+x}Sn_{0.975}Sb_{0.025}$ nanocomposites remain nearly constant in the temperature range investigated. The observed comparable values of the electrical conductivities of the samples with x = 0, 0.02 and 0.04 resulted from the similarity in their carrier density and mobility (Figure 4.2D), whereas for the sample with x = 0.1, the large increase in the carrier density (Figure 4.2A) is compensated by a decrease in the carrier mobility. The observed constant carrier mobility in $Ti_{0.1}Zr_{0.9}Ni_{1+x}Sn_{0.975}Sb_{0.025}$ nanocomposites with x = 0.02 and 0.04 is quite surprising and suggests that the embedded FH inclusions do not alter charge carriers transport at the HH/FH interfaces. The fitting of the temperature dependence of the carrier mobility of $Ti_{0.1}Zr_{0.9}Ni_{1+x}Sn_{0.975}Sb_{0.025}$ nanocomposites using the power law $T^{-\lambda}$ resulted in λ values of 0.84 (x = 0), 0.77 (x = 0.02), 0.74 (x = 0.04) and 0.94 (x = 0.1). The observed values of the power exponent λ suggest that the temperature dependence of the carrier mobility at high temperature is affected by both acoustic phonon and optical phonon scattering.

Figure 4.3B shows the temperature dependence of the power factor ($PF = \sigma \cdot S^2$) of Sb-doped $Ti_{0.1}Zr_{0.9}Ni_{1+x}Sn_{0.975}Sb_{0.025}$ nanocomposites. At 300K the PF of the Sb-doped HH- matrix ($Ti_{0.1}Zr_{0.9}NiSn_{0.975}Sb_{0.025}$) is ~ 2200 $\mu W/K^2 \cdot m$. This value is six times larger than the value measured for the undoped HH-matrix ($Ti_{0.1}Zr_{0.9}NiSn$) and is consistent with the large increase in the electrical conductivity upon Sb doping at Sn sites in the structure of $Ti_{0.1}Zr_{0.9}NiSn$. The PF of the Sb-doped matrix increases monotonically with rising temperature reaching a value of 4000 $\mu W/K^2 \cdot m$ at 775K. Interestingly, the insertion of various fractions of FH nanoinclusions in the Sb-doped HH-matrix ($Ti_{0.1}Zr_{0.9}NiSn_{0.975}Sb_{0.025}$) maintains the PF of resulting

$Ti_{0.1}Zr_{0.9}Ni_{1+x}Sn_{0.975}Sb_{0.025}$ nanocomposites essentially unchanged at all temperatures (Figure 4.3B). This result is consistent with the observed comparable values of the electrical conductivity and thermopower of various $Ti_{0.1}Zr_{0.9}Ni_{1+x}Sn_{0.975}Sb_{0.025}$ nanocomposites. It also suggests that the embedded FH nanoinclusions are electronically inert (i.e. do not significantly alter the effective carrier density) with regards to the Sb-doped HH matrix and are transparent to charge carriers leading to marginal alteration of the carrier mobility at the HH/FH interfaces.

The temperature dependence of the lattice thermal conductivity of the synthesized Sb-doped $Ti_{0.1}Zr_{0.9}Ni_{1+x}Sn_{0.975}Sb_{0.025}$ nanocomposites is shown in Figure 4.3C. At 300K, the lattice thermal conductivity of the Sb-doped HH- matrix ($Ti_{0.1}Zr_{0.9}NiSn_{0.975}Sb_{0.025}$) is ~ 9 W/m·K. This corresponds to a 30% reduction from the lattice thermal conductivity of the undoped matrix ($Ti_{0.1}Zr_{0.9}NiSn$). The observed reduction in the lattice thermal conductivity of Sb-doped matrix at 300K is attributed to the scattering of phonon by mass fluctuation and point defects arising from the intermixing of Sn and Sb at various Sn sites in the structure of $Ti_{0.1}Zr_{0.9}NiSn$. Interestingly, additional reductions in the lattice thermal conductivity are obtained through the insertion of various fractions of FH nanoinclusions in the Sb-doped HH matrix. The lattice thermal conductivities of the Sb-doped $Ti_{0.1}Zr_{0.9}Ni_{1+x}Sn_{0.975}Sb_{0.025}$ nanocomposites decrease with increasing temperature reaching a value of 4.4 W/m·K at 775K for the sample with x = 0.04. This corresponds to 27% reduction when compared to the lattice thermal conductivity of the Sb-doped HH matrix ($Ti_{0.1}Zr_{0.9}NiSn_{0.975}Sb_{0.025}$) at 775K. We attribute the observed large reductions in the lattice thermal conductivity of $Ti_{0.1}Zr_{0.9}Ni_{1+x}Sn_{0.975}Sb_{0.025}$ nanocomposites at high temperatures to enhanced phonon scattering at multiple HH/FH coherent interfaces dispersed throughout the Sb-doped HH matrix.

Figure 4.3D shows the temperature dependence of the figure of merit, ZT, of various $Ti_{0.1}Zr_{0.9}Ni_{1+x}Sn_{0.975}Sb_{0.025}$ nanocomposites. The ZT value of ~ 0.05 was obtained at 300K for the Sb-doped HH matrix. However, upon increasing the temperature, the ZT values of the sample rapidly increase to ~ 0.3 at 775 K. This value is four times higher than the ZT ~ 0.08 measured for undoped HH matrix. The observed increase in the ZT is due to the optimization of the electronic properties through Sb doping at Sn sites in the structure of $Ti_{0.1}Zr_{0.9}NiSn$. The reduction in the lattice thermal conductivity of Sb-doped HH matrix, while maintaining the PF essentially unchanged achieved by introduction of coherent FH inclusions within the $Ti_{0.1}Zr_{0.9}NiSn_{0.975}Sb_{0.025}$ matrix resulted in an additional 13% increase in the overall ZT of the $Ti_{0.1}Zr_{0.9}Ni_{1+x}Sn_{0.975}Sb_{0.025}$ nanocomposites.

4.3 Conclusion

In summary, we have demonstrated the ability to combine in a HH semiconducting matrix with a given chemical composition, a large enhancement in the electronic properties (electrical conductivity and thermopower) using substitutional chemistry (Sb doping) with a significant reduction in the thermal conductivity via nanostructuring to drastically increase the figure of merit of the resulting HH nanocomposites. The key to this interesting independent manipulation of the power factor and lattice thermal conductivity of heavily doped HH(1-x)/FH(x) nanocomposites lies in the unique possibility of HH and FH compounds with similar chemical composition to form structurally coherent phase boundaries and suitable alignment of the their valence bands and conduction bands at the HH/FH interfaces. These essential structural and electronic features of the HH/FH interfaces enable efficient carrier transfer across, while blocking the propagation of thermal phonon. From our earlier work on undoped $Ti_{0.1}Zr_{0.9}NiSn$

HH matrix, we found that the introduction of coherent FH nanoinclusions resulted in large decreases in the effective carrier density due to the filtering of low energy carriers at the HH/FH interfacial potential energy . As a consequence, large increase in the thermopower and carrier mobility was observed for the resulting HH/FH nanocomposites simultaneously with large reductions in the lattice thermal conductivity. However, results from the current study show that under heavily doped conditions where the electronic conduction is likely controlled by a large fraction of extrinsic carriers with energy higher that the potential barrier at the HH/FH interfaces, the effect of filtering of low energy intrinsic carriers at the HH/FH interfaces on the overall carrier density of the sample is marginal. As a consequence, the thermopower and carrier mobility remain unchanged upon introduction of coherent FH nanoinclusions in a heavily doped semiconducting HH matrix. This explains the observed constant value of the PF for samples with various fractions of FH inclusions. It derives from the present work that one can efficiently reduce the thermal conductivity of heavily doped HH semiconductor using coherent FH nanostructures with marginal alteration of the PF. Such strategy can be easily applied to optimized HH matrices to further increase their thermoelectric figure of merit.

CHAPTER 5

THERMOELECTRIC PROPERTIES OF GE DOPED N-TYPE $Ti_XZr_{1-X}NiSn_{0.975}Ge_{0.025}$ HALF-HEUSLER ALLOYS

5.1 Objective

Most studies in *n-type* MNiSn HH systems are focused on the intermixing of two or three elements at the M site, or the substitution of Sn by a small amount of a heavier element, such as Sb or Bi, to enhance phonon scattering[55, 96-100]. However, studies exploring mass fluctuation at both M and Sn positions in MNiSn HH alloys are scarce. In this work, we explore the effect of band gap engineering through isoelectronic substitution of Sn by Ge and mass fluctuation arising from the intermixing of Ti and Zr on the thermoelectric properties of $Ti_xZr_{1-x}NiSn_{0.975}Ge_{0.025}$ (x = 0, 0.1, 0.15 and 0.25) composites synthesized by induction melting of the elements followed by mechanical alloying using high energy shaker ball milling. All samples were consolidated under the same condition using a uniaxial hot pressing system. Scanning electron microscopy (SEM) and high-resolution transmission electron microscopy (HRTEM) revealed the presence of Ti-rich and Zr-rich phases in bulk ingots obtained from composition with x = 0.25. We found that the substitution of 2.5% Sn by Ge in $Ti_{0.1}Zr_{0.9}NiSn_{0.975}Ge_{0.025}$ led to large reduction in the thermal conductivity and marginal change in the electrical conductivity and thermopower. This markedly differs from the effect of Sb-doping at Sn sites ($Ti_{0.1}Zr_{0.9}NiSn_{0.975}Sb_{0.025}$), where significant

increase in the electrical conductivity and large reduction in the thermopower was observed[101]. In addition, we found that increasing Ti concentration in $Ti_xZr_{1-x}NiSn_{0.975}Ge_{0.025}$ resulted in a simultaneous increase in the thermopower and additional reduction in the thermal conductivity. This large reduction in the thermal conductivity of $Ti_xZr_{1-x}NiSn_{0.975}Ge_{0.025}$ is attributed to the introduction of mass fluctuation at both M and Sn sites in MNiSn HH alloys.

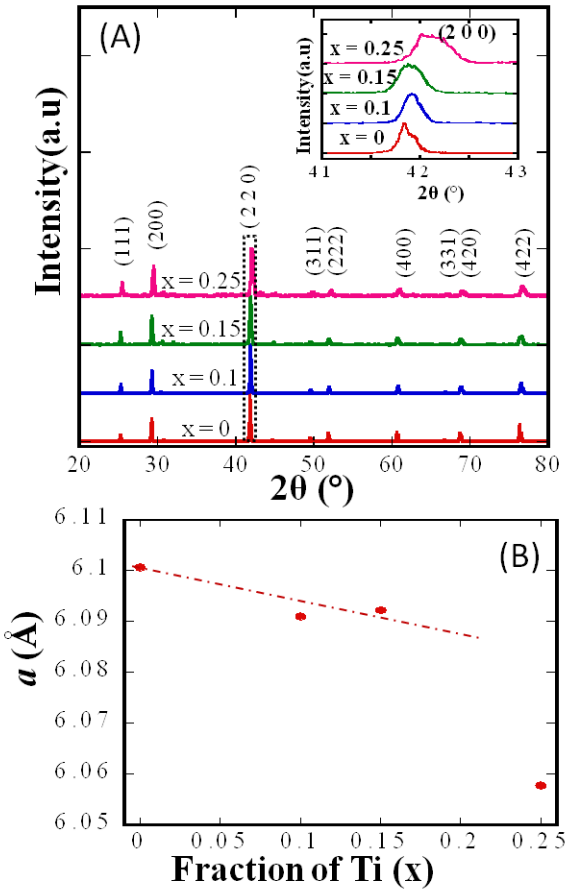

Figure 5.1 (A) X-ray diffraction pattern of $Ti_xZr_{1-x}NiSn_{0.975}Ge_{0.025}$ (x = 0, 0.1, 0.15 and 0.25) samples after heat treatment and mechanical alloying. The insert shows the broadening of the (220) peak with increasing Ti concentration, indicating intrinsic phase separation into Ti-rich and Zr-rich phases; (B) Lattice parameters calculated from the XRD patterns of TixZr1-xNiSn0.975Ge0.025 (x = 0, 0.1, 0.15 and 0.25) samples after heat treatment.

5.2 Results and discussion

5.2.1 Phase stability

Figure 5.1A shows the X-ray powder diffraction patterns of the synthesized $Ti_xZr_{1-x}NiSn_{0.975}Ge_{0.025}$ (x = 0, 0.1, 0.15 and 0.25) samples after heat treatment and after the mechanical alloying steps. All peaks from the XRD patterns can be indexed with the MgAgAs structure type suggesting the formation of HH alloys. A careful examination of XRD patterns of $Ti_xZr_{1-x}NiSn_{0.975}Ge_{0.025}$ (x = 0, 0.1, 0.15 and 0.25) reveals a shift of the (2 2 0) peak towards higher angles when Ti concentration increases. This indicates the substitution of

large Zr (155 ppm) atoms by smaller Ti (140 ppm) atoms in the ZrNiSn structure. This result is consistent with previous studies[9, 99, 102-103]. Figure 5.1B shows the change in the lattice parameter of all samples, after heat treatment, with increasing Ti concentration. The calculated lattice parameters slightly deviate from Vegard's law, which suggests the formation of multiple phases. This analysis is supported by the broadening of the (2 2 0) peak with increasing Ti concentration, which also indicates intrinsic phase separation into Ti-rich and Zr-rich phases (Figure 5.1A).

Figure 5.2A shows a back-scattered electron (BSE) SEM image of a specimen cut from a pressed pellet with nominal composition $Ti_{0.25}Zr_{0.75}NiSn_{0.975}Ge_{0.025}$ indicating the presence of two distinct phases within the bulk material. The light gray area is attributed to Zr-rich (heavy element) HH phase, whereas the dark gray area is believed to be Ti-rich (lighter element) HH phase. This result is also consistent with the broadening of (2 2 0) peaks, which suggests the coexistence of two HH phases with similar lattice parameters

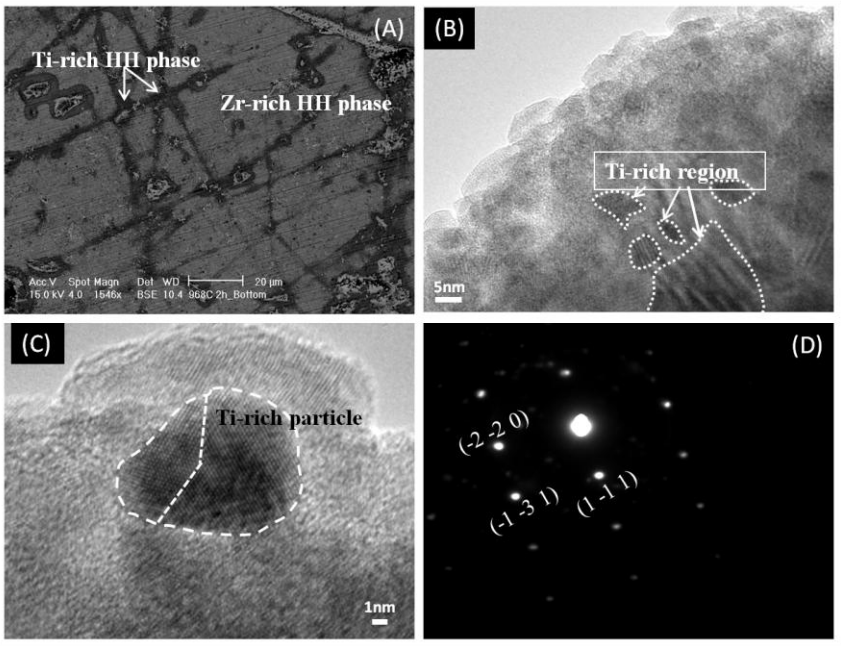

Figure 5.2 Electron microscopy study of $Ti_{0.25}Zr_{0.75}NiSn_{0.975}Ge_{0.025}$ (x = 0, 0.1, 0.15 and 0.25) composites. (A) Back scattering electron (BSE) of SEM image, showing micron size Ti-rich phase in Zr-rich matrix; (B) low magnification TEM image, showing 10 nm Ti-rich phase embedded inside Zr-rich matrix; (C) high magnification TEM image, showing the crystallization of the Ti-rich nanophase ; (D) selected area electron diffraction (SAED) pattern, indicating the fcc structure of Zr-rich HH matrix.

(Ti-rich and Zr-rich HH phases). It is interesting to note the formation, for the sample with x = 0.25, of nanometer-scale phases within the matrix, contrary to previous studies[104-105]. The formation of such fine nanometer scale features results from the mechanical alloying steps following the formation of $Ti_xZr_{1-x}NiSn_{0.975}Ge_{0.025}$ samples through induction melting of elemental powders. As can be observed from the low magnification TEM imaging (Figure 5.2B), these features appear as dark particles dispersed in a bright matrix. These nanoscale dark spots are believed to be Ti-rich particles, which are separated in the nanometer range by Zr-rich regions. Some of the Ti-rich nanostructures overlap to form large agglomerates. From Figure 5.2C, it can be seen that particles of a Ti-rich phase is formed by agglomeration of small crystals with different orientations. The lattice parameter, a = 6.12 Å, calculated from the SAED pattern (Figure 5.2D) is comparable to the lattice parameter of $ZrNiSn_{0.975}Ge_{0.025}$ further confirming that the matrix is Zr-rich.

5.2.2 Thermoelectric properties

In our earlier work [3, 101], we demonstrated that the substitution of a small amount (2.5%) of Sb at Sn site in the structure of $Ti_{0.1}Zr_{0.9}NiSn$ led to the heavily doped $Ti_{0.1}Zr_{0.9}NiSn_{0.975}Sb_{0.025}$ semiconductor with a slight improvement of the thermoelectric properties. In the current work, we assess the effect of band gap engineering through isoelectronic substitution of 2.5% Ge at Sn site on the thermoelectric behavior of $Ti_{0.1}Zr_{0.9}NiSn_{0.975}Ge_{0.025}$ system. Figure 5.3 shows a comparison of the temperature dependent the thermoelectric properties of $Ti_{0.1}Zr_{0.9}NiSn_{0.975}Ge_{0.025}$ samples with data previously reported for the $Ti_{0.1}Zr_{0.9}NiSn$ and $Ti_{0.1}Zr_{0.9}NiSn_{0.975}Sb_{0.025}$ samples synthesized by solid-state reactions of the elements. Regardless of the temperature, the highest electrical conductivity is observed for the Sb-doped sample, $Ti_{0.1}Zr_{0.9}NiSn_{0.975}Sb_{0.025}$. This is consistent with the expected increase in the carrier density upon

substituting Sn by Sb in the structure of $Ti_{0.1}Zr_{0.9}NiSn$. The electrical conductivity of the $Ti_{0.1}Zr_{0.9}NiSn_{0.975}Sb_{0.025}$ sample decreases with increasing temperature, which is consistent with heavily doped semiconducting behavior.

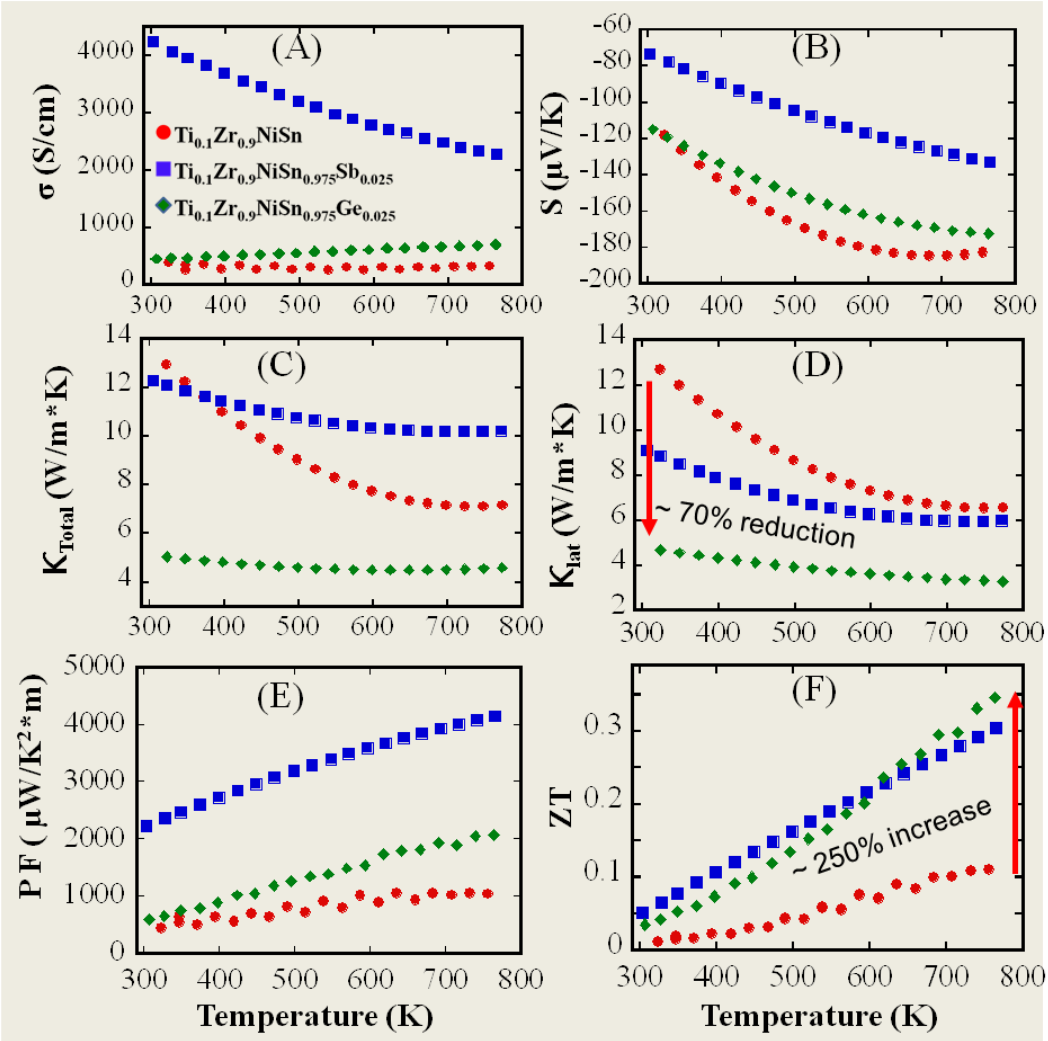

Figure 5.3: Temperature dependence of (A) electrical conductivity; (B) thermopower; (C) thermal conductivity; (D) lattice thermal conductivity; (E) power factor and (F) figure of merit of $Ti_{0.1}Zr_{0.9}NiSn$; $Ti_{0.1}Zr_{0.9}NiSn_{0.975}Sb_{0.025}$and $Ti_{0.1}Zr_{0.9}NiSn_{0.975}Ge_{0.025}$ samples.

Interestingly, the electrical conductivity of $Ti_{0.1}Zr_{0.9}NiSn_{0.975}Ge_{0.025}$ is higher than that of $Ti_{0.1}Zr_{0.9}NiSn$ at temperatures above 300 K. This is a quite surprising result. While the isoelectronic substitution of Ge at Sn sites in the structure of $Ti_{0.1}Zr_{0.9}NiSn$ is not expected to contribute additional carriers (i.e. constant carrier density) to the conduction band, a slight increase in the electrical band gap can be anticipated. This should result in a drop in the carrier density, at a given temperature, when compared to undoped $Ti_{0.1}Zr_{0.9}NiSn$ matrix. Therefore, lower electrical conductivity and higher thermopower would be expected for $Ti_{0.1}Zr_{0.9}NiSn_{0.975}Ge_{0.025}$ compared to $Ti_{0.1}Zr_{0.9}NiSn$ system. However, the observed higher electrical conductivity and lower thermopower for $Ti_{0.1}Zr_{0.9}NiSn_{0.975}Ge_{0.025}$ imply a reduction in the electrical band gap $Ti_{0.1}Zr_{0.9}NiSn$ upon isoelectronic substitution of Sn by Ge. One possible explanation of the reduction of the electrical band gap is that the substitution of Sn by Ge instead of modifying the band structure of the matrix creates impurity states within the band gap. This results in lower activation energy and an increase in the concentration of thermally excited carriers at a given temperature. This is consistent with the lower thermopower values observed at high temperatures for Ge-substituted samples. The electrical conductivity of $Ti_{0.1}Zr_{0.9}NiSn$ and $Ti_{0.1}Zr_{0.9}NiSn_{0.975}Ge_{0.025}$ increases with rising temperature, indicating intrinsic semiconducting behavior.

Figure 5.3 C and D show the temperature dependence of total thermal conductivity and lattice thermal conductivity of $Ti_{0.1}Zr_{0.9}NiSn$, $Ti_{0.1}Zr_{0.9}NiSn_{0.975}Sb_{0.025}$ and $Ti_{0.1}Zr_{0.9}NiSn_{0.975}Ge_{0.025}$ samples. The thermal conductivity of all samples decreases with increasing temperature. Regardless of the temperature, the Ge-substituted sample exhibits the lowest total thermal conductivity. At 300 K, the total thermal conductivity decreases from 13 $Wm^{-1}K^{-1}$ for the undoped sample to 5 $Wm^{-1}K^{-1}$ upon substitution of Sn by 2.5 % Ge. The lattice

thermal conductivity (κ_L) was obtained by subtracting electronic thermal conductivity (κ_e) from total thermal conductivity, κ. κ_e was estimated through Wiedemann-Franz law, $\kappa_e = L_o \sigma T$, where $L_o = 2.45 \times 10^{-8}$ $W\Omega K^{-2}$ is Lorenz number. The lattice thermal conductivity of all samples also follows similar trend with the total thermal conductivity. At 300 K, the lattice thermal conductivity of $Ti_{0.1}Zr_{0.9}NiSn$ is 12.6 $Wm^{-1}K^{-1}$. Upon substituting of 2.5% Sn by Sb, the lattice thermal conductivity of $Ti_{0.1}Zr_{0.9}NiSn_{0.975}Sb_{0.025}$ decreases to 9 $Wm^{-1}K^{-1}$. Interestingly, the substitution of Sn by 2.5 % Ge in $Ti_{0.1}Zr_{0.9}NiSn$ results in a remarkable reduction in the lattice thermal conductivity to ~5 $Wm^{-1}K^{-1}$ at 300 K. At 775 K, $Ti_{0.1}Zr_{0.9}NiSn$ and $Ti_{0.1}Zr_{0.9}NiSn_{0.975}Sb_{0.025}$ have similar values of the lattice thermal conductivity (~ 6 $Wm^{-1}K^{-1}$), whereas the lattice thermal conductivity of $Ti_{0.1}Zr_{0.9}NiSn_{0.975}Ge_{0.025}$ reaches 2.7 $Wm^{-1}K^{-1}$. The drastic reduction in the total thermal conductivity is due to high phonon scattering arising from the combination of (1) mass fluctuation due to Ge/Sn substitution and (2) high-density grain boundaries from particle size refinement by mechanical alloying. This large difference in the thermal conductivity of $Ti_{0.1}Zr_{0.9}NiSn_{0.975}Ge_{0.025}$ and $Ti_{0.1}Zr_{0.9}NiSn$ samples results from the grain size refinement of the synthesized $Ti_{0.1}Zr_{0.9}NiSn_{0.975}Ge_{0.025}$ powders by mechanical alloying.

The temperature dependence of the power factor calculated using the electrical conductivity and thermopower data for $Ti_{0.1}Zr_{0.9}NiSn$; $Ti_{0.1}Zr_{0.9}NiSn_{0.975}Sb_{0.025}$ and $Ti_{0.1}Zr_{0.9}NiSn_{0.975}Ge_{0.025}$ is shown in Figure 5.3E. It can be seen that the substitution of Sn by 2.5 % Sb leads to a drastic increase in the power factor, which is mostly due to the large increase in the carrier concentration. However, the substitution of Sn by Ge is isoelectronic; therefore, the increase in the power factor on the Ge-substituted sample cannot be explained only by considering the increase in the carrier concentration arising from the reduction in the band gap as discussed above. This is due to the fact that an increase in the electrical conductivity through

thermal excitation of electrons from the valence band (or impurity band) to the conduction band would normally be offset by a reduction in the thermopower. Therefore, the observed enhancement of the power factor of Ge-substituted sample compared to the undoped Sn sample suggests that the observed increase in the electrical conductivity is not completely offset by a reduction in the thermopower. This can be explained by considering an enhancement in the overall carrier mobility for Ge-substituted sample. One can speculate that the substitution of Ge at Sn sites brings higher mobility electrons to the system, which increases the overall mobility of carrier in the sample. The *ZT* value at 775 K for the Ge-substituted sample is slightly larger than that of Sb-doped sample. This is due to the combination of drastic reduction in the thermal conductivity and marginal increase in the power factor which leads to a 250 % increase in the figure of merit (0.35 at 775 K) compared to undoped sample.

In order to probe the effect of the Ti/Zr ratio on the thermoelectric properties of $Ti_xZr_{1-x}NiSn_{0.975}Ge_{0.025}$ alloys, various compositions with x = 0, 0.1, 0.15 and 0.25 were synthesized and their thermoelectric properties were measured from 300 K to 775 K (Figure 5.4). The electrical conductivity of all these samples increased with rising temperature indicating intrinsic semiconducting behavior. Regardless of the temperature, the largest electrical conductivity is observed for the sample with x = 0 ($ZrNiSn_{0.975}Ge_{0.025}$). At 300 K, the electrical conductivity initially decreases from 680 S/cm for the sample with x = 0 to 440 S/cm for the sample with x = 0.1 and 0.15 then slightly increase to 520 S/cm for the sample with x = 0.25 (Figure 5.4A).

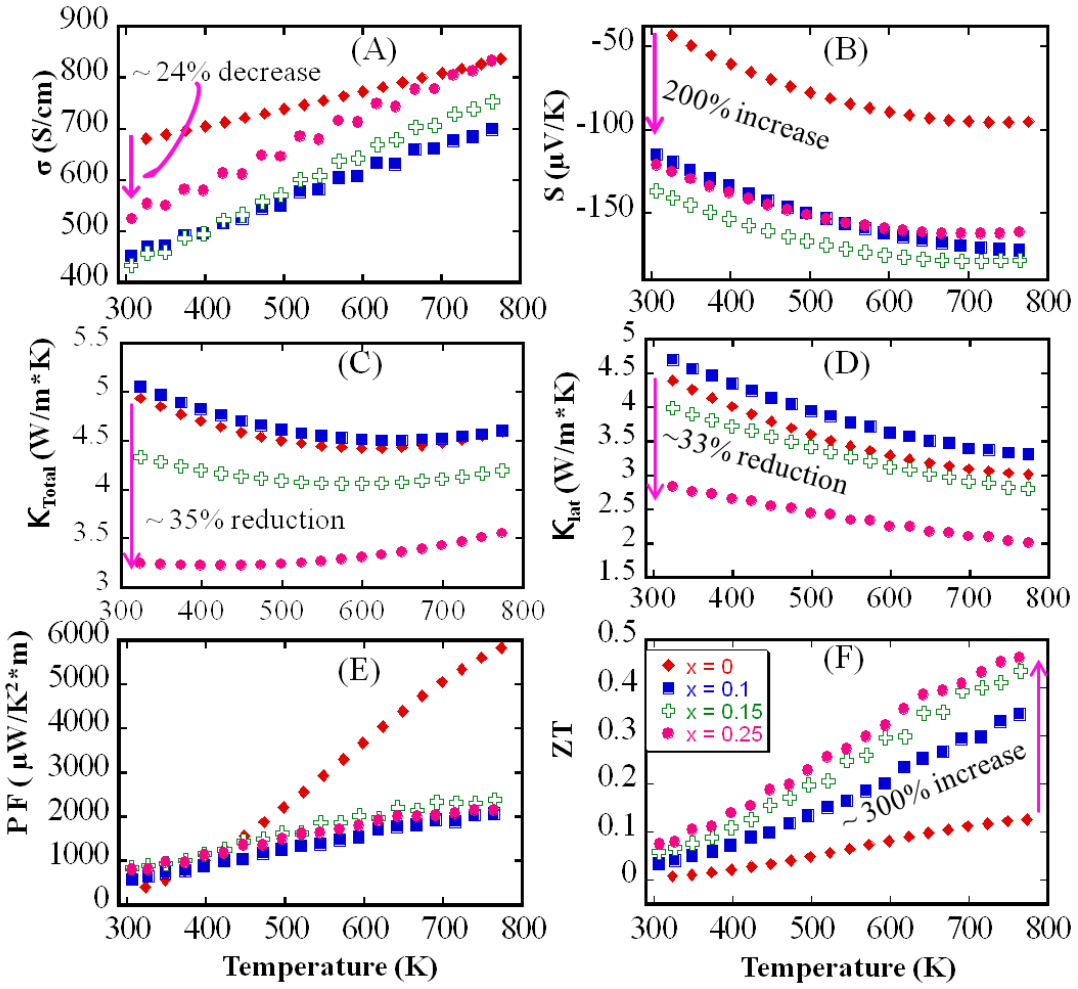

Figure 5.4: Temperature dependence of (A) electrical conductivity; (B) thermopower; (C) thermal conductivity; (D) lattice thermal conductivity; (E) power factor and (F) figure of merit of $Ti_xZr_{1-x}NiSn_{0.975}Ge_{0.025}$ (x = 0, 0.1, 0.15 and 0.25) samples.

To better understand the reason behind the change of the electrical conductivity, the band gap (E_g) was calculated by fitting the conductivity curve using the Arrhenius equation, $\sigma = \sigma_0 exp^{-\frac{E_g}{2kT}}$. It was found that the band gap increases with increasing Ti concentration (Figure 5.5), reaching the highest value (E_g = 81 meV) for the sample with x = 0.15 and decreasing to 41 meV with further increase in Ti concentration to x = 0.25. Therefore, the observed decrease in the electrical conductivity upon increasing the Ti content from 0 to 0.15 can be associated with the drop in the

carrier concentration at a given temperature due to an increase in the band gap. Interestingly, this trend is broken for the sample with x = 0.25, in which an increase in the carrier concentration (smaller band gap) is observed. This deviation from the general trend can be associated to the phase separation into Zr-rich matrix with Ti-rich nanostructures observed in the sample with x = 0.25 (Figure 5.2), instead of the solid-solutions observed for samples with x ≤ 0.15. In such composites, both the Zr-rich phase with high electrical conductivity and the Ti-rich phase with poor electrical conductivity contribute to the observed overall electrical conductivity of the sample. The electrical conductivity of the sample with x = 0.25 rapidly increases with rising temperature reaching a value similar to that of $ZrNiSn_{0.975}Ge_{0.025}$ at 775 K.

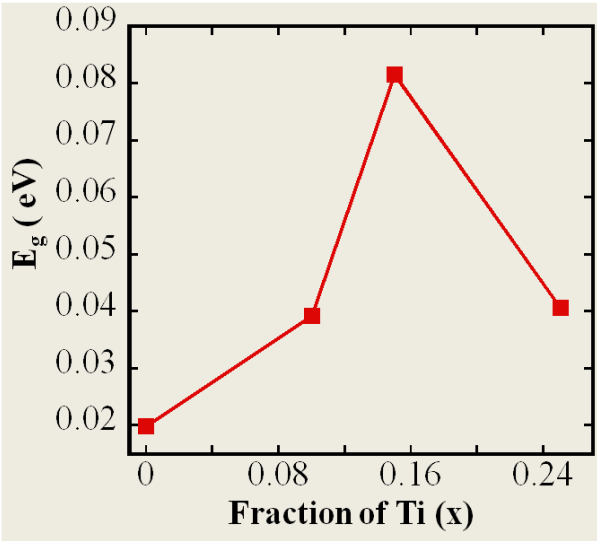

Figure 5.5: Band gap calculated from the electrical conductivity of $Ti_xZr_{1-x}NiSn_{0.975}Ge_{0.025}$ (x = 0, 0.1, 0.15 and 0.25) samples.

Figure 5.4B shows the temperature dependence of the thermopower of $Ti_xZr_{1-x}NiSn_{0.975}Ge_{0.025}$ samples. All samples show negative thermopower indicating *n-type* semiconducting behavior. At 300 K, the thermopower increases with Ti concentration from -40 μV/K for the sample with x = 0 to -140 μV/K for the sample with x = 0.15, then decreases to -120 μV/K upon increasing the Ti concentration to x = 0.25. Regardless of the composition, the absolute themopower increases with increasing temperature. At 775 K, the largest thermopower value of -180 μV/K is observed for the sample with x = 0.15. The most surprising result here is the large difference in the thermopower values of samples with x = 0 and 0.25 at 775 K, despite the similarity in their

electrical conductivity. To rationalize this result, one must take into account the role of Ti-rich nanostructures on the electronic transport within the Zr-rich matrix. As demonstrated above, the substitution of 25% Zr by Ti results in a phase separation into microscale and nanometer-scale Ti-rich inclusions within the Zr-rich half-Heusler matrix. At 300K, we observed a small reduction (~24%) in the electrical conductivity (from 680 S/cm for x = 0 to 520 S/cm for x = 0.25) and drastic increase (~200%) in the thermopower (from -40 μV/K for x = 0 to -120 μV/K for x = 0.25) of the sample with x = 0.25 when compared to the pure matrix.

The total thermal conductivity and lattice thermal conductivity of $Ti_xZr_{1-x}NiSn_{0.975}Ge_{0.025}$ samples are plotted in Figure 5.4C and D. The total thermal conductivity at a given temperature decreases with increasing Ti concentration. At 300 K, the total thermal conductivity decreases from ~ 5 $Wm^{-1}K^{-1}$ for x = 0 to ~3.25 $Wm^{-1}K^{-1}$ for x = 0.25. Regardless of the composition, the total thermal conductivity initially decreases with rising temperature to reach a minimum then increases with further increase in temperature. This trend can be ascribed to the effect of bipolar conduction at temperatures above the temperature of minimum thermal conductivity. The lattice thermal conductivity of the $Ti_xZr_{1-x}NiSn_{0.975}Ge_{0.025}$ samples decrease with increasing temperature (Figure 5.4D). The lowest lattice thermal conductivity (2 $Wm^{-1}K^{-1}$ at 775 K) is observed for the sample with x = 0.25. The observed large reduction in the lattice thermal conductivity with increasing Ti concentration can be explained by (1) mass fluctuation phonon scattering due to intermixing of Ti/Zr at the same atomic site and (2) enhanced phonon scattering at the nanometer scale and micrometer scale phase boundary between the Zr-rich HH matrix and Ti-rich HH inclusions in $Ti_{0.25}Zr_{0.75}NiSn_{0.975}Ge_{0.025}$ composite.

Figure 5.4E displays the temperature dependence of the power factor of all $Ti_xZr_{1-x}NiSn_{0.975}Ge_{0.025}$ samples. At 300 K, all samples show a similar power factor of ~ 900 $\mu W/K^2m$.

As the temperature increases, the power factor of the sample with x = 0 rapidly increases to ~ 6000 $\mu W/K^2m$ at 775 K. However, the samples with x = 0.1, 0.15 and 0.25 show much lower power factor (~ 2100 $\mu W/K^2m$) at 775 K. Despite the relatively low power factor of Ti containing samples, the observed low thermal conductivity results in large enhancements of the figure of merit when compared to the sample with x = 0 (Figure 5.4F). At 300 K, *ZT* values increase with Ti concentration from 0.05 to 0.08. As the temperature increases, the *ZT* values of various samples increase, reaching a maximum of 0.48 at 775 K for the sample with x = 0.25.

5.3 Conclusion

In summary, we have examined the effects of Ge substitution at Sn sites and of Ti substitution at Zr sites (varying Ti/Zr ratios) on the thermoelectric properties of $Ti_xZr_{1-x}NiSn_{0.975}Ge_{0.025}$ (x = 0, 0.1, 0.15 and 0.25) series of samples produced by induction melting and mechanical alloying. We found that increasing the Ti concentration above x = 0.15 led to a phase separation in the bulk $Ti_xZr_{1-x}NiSn_{0.975}Ge_{0.025}$ samples with the formation of Ti-rich inclusions embedded into the Zr-rich matrix. This combination of partial solid solution and phase separation in $Ti_xZr_{1-x}NiSn_{0.975}Ge_{0.025}$ resulted in a large reduction in the thermal conductivity. In addition, we observed an increase in the thermopower with increasing Ti concentration leading to an improvement in the power factor when compared to the sample with x = 0. The simultaneous increase in the power factor and large reduction in the thermal conductivity of $Ti_xZr_{1-x}NiSn_{0.975}Ge_{0.025}$ samples resulted in a large increase in the *ZT* with a maximum value of 0.48 observed at 775 K for $Ti_{0.25}Zr_{0.75}NiSn_{0.975}Ge_{0.025}$ composites. This work demonstrates that by manipulating the band gap of half-Heusler alloys through isoelectronic substitution at Ti/Zr and

Sn/Ge sites, simultaneous enhancement of thermopower and reduction in thermal conductivity can be achieved leading to a significant increase in the *ZT* value.

CHAPTER 6

NANOSTRUCTURING AND CHARGE TRANSPORT IN BULK DOPED HALF-HEUSLER COMPOSITES

6.1 Objective

Here, we explore the behavior of FH phase in the HH matrix with decreasing doping level in heavily doped $Zr_{0.25}Hf_{0.75}Ni_{1+x}Sn_{1-y}Sb_y$ (x= 0~0.15 and y= 0.025, 0.01 and 0.005) composites. The thermoelectric properties with samples with different doping level were compared to demonstrate the effect of FH phase coherently embedded in the HH matrix on the electronic and phonon transports. We found that the energy filtering effect was enhanced when the doping level decreased. It strongly blocked the charge carrier density in samples with the lowest doping level. The formation of FH particle was observed through HRTEM and it was found that these particles aggregated together with increasing Ni content. Although interface potential of FH/HH was formed upon introduction of FH phase in the HH matrix, the energy filtering effect is very strong only for a small amount of Sb doping.

6.2 Result and Discussion

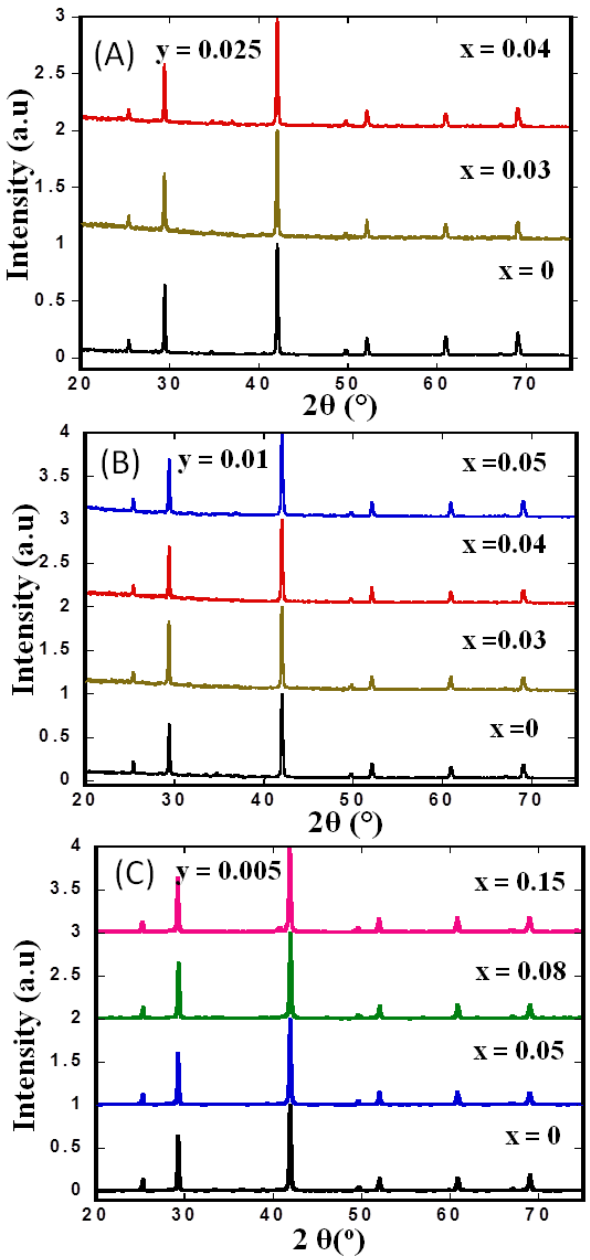

Figure 6.1 Powder XRD pattern of the synthesized composites for $Zr_{0.25}Hf_{0.75}Ni_{1+x}Sn_{1-y}Sb_y$ composites.

6.2.1 Phase characterization

Powder X-ray diffraction patterns of as-synthesized FH/HH composites of $Zr_{0.25}Hf_{0.75}Ni_{1+x}Sn_{0.975}Sb_{0.025}$, $Zr_{0.25}Hf_{0.75}Ni_{1+x}Sn_{0.99}Sb_{0.01}$ and $Zr_{0.25}Hf_{0.75}Ni_{1+x}Sn_{0.995}Sb_{0.005}$ are shown in Figure 6.1. All peaks on the XRD patterns can be indexed in the cubic MgAgAs-type structure suggesting the formation of single-phase HH alloys. Surprisingly, the addition of excess Ni in various HH matrices does not create additional diffraction peaks on the XRD patterns that could be assigned to the formation of FH phase or other impurity phases in the samples. This suggests that the size of FH phase is too small to diffract X-ray or that impurities are soluble in the HH matrix. However, the unit cell parameter of

$Zr_{0.25}Hf_{0.75}Ni_{1+x}Sn_{1-y}Sb_y$ samples remains constant, a = 6.15 (8) Å, regardless of the excess Ni or Sb doping level. This suggests that the structure of the HH phase remains unchanged upon addition of excess Ni element or substitution of Sb at Sn sites.

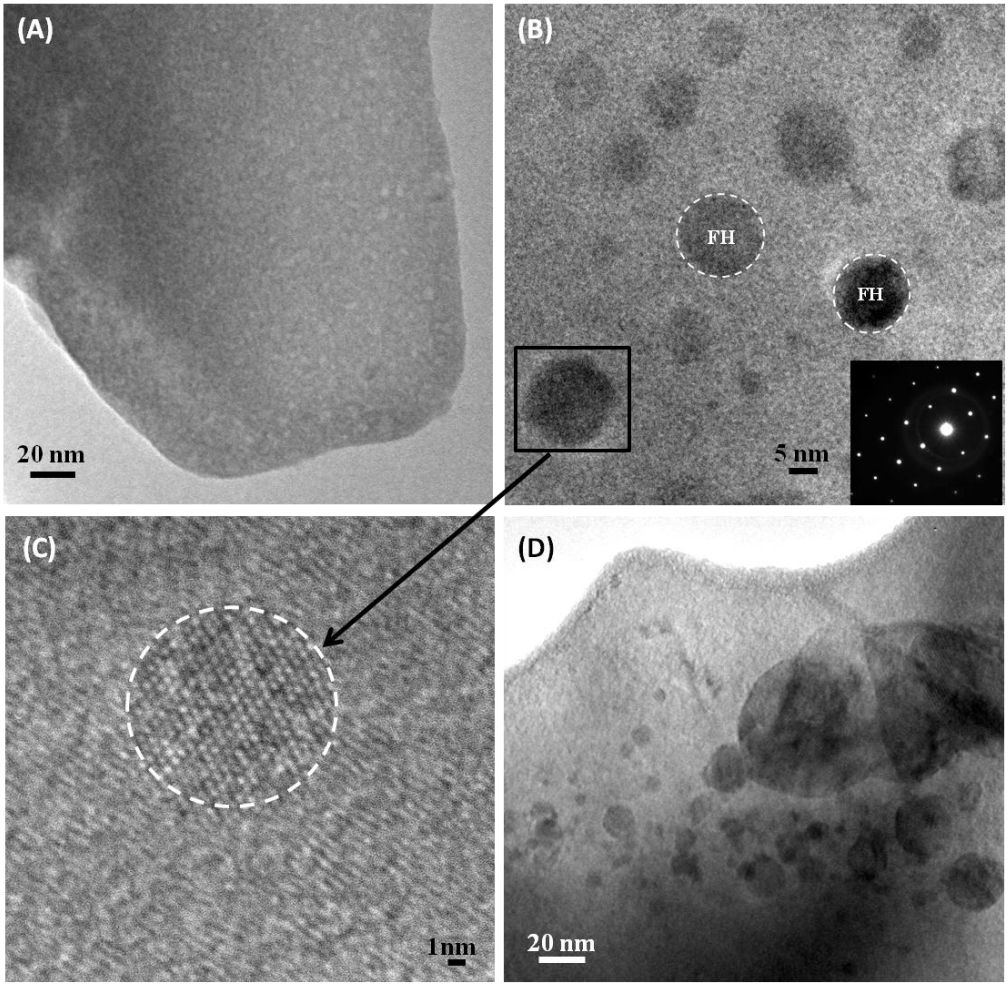

Figure 6.2 Structural characteristics of $Zr_{0.25}Hf_{0.75}Ni_{1+x}Sn_{0.995}Sb_{0.005}$ nanocomposites. (A) Low magnification TEM image of the HH matrix, revealing the matrix is clear and no inclusion or impurities. (B) Medium magnification TEM image of the sample with x= 0.05 showing FH particles with size range 5~ 20 nm coherently embedded inside the HH matrix and selected-area electron diffraction pattern (inset of B) indicating the fcc structure of the HH matrix. (C) High magnification TEM image of selected FH particle from the sample with x = 0.05, showing nearly spherical FH nanoinclusion lattice details. (D) Low magnification TEM image of the sample with x= 0.15, showing high agglomeration of FH nanophase into large particle.

Figure 6.2 shows high-resolution TEM images highlighting microstructural characteristics of selected $Zr_{0.25}Hf_{0.75}Ni_{1+x}Sn_{0.995}Sb_{0.005}$ nanocomposites. A low magnification TEM image of the HH matrix (Figure 6.2A) suggests the formation of single-phase HH structure. No inclusion or impurities phase are found on the TEM image (Figure 6.2A). However, the addition of excess elemental Ni into the HH matrix leads to the formation of small dark precipitates (Figure 6.2B and 6.2D). These nanoinclusions are believed to adopt FH structure and composition given the high degree of coherency with the HH matrix (Figure 6.2C). As can be observed from the TEM images of the sample with x = 0.05, y = 0.005, the FH nanoprecipitates formed as small spherical particles with size ranging from 5 nm to 20 nm (Figure 6.2B). Increasing the concentration of excess Ni resulted in the formation of a large fraction of FH precipitates. Some precipitates agglomerate into larger nanoparticles with size of up to 100 nm as can be observed on the TEM image of $Zr_{0.25}Hf_{0.75}Ni_{1.15}Sn_{0.995}Sb_{0.005}$ (Figure 6.2D). Similar microstructural characteristics are expected in $Zr_{0.25}Hf_{0.75}Ni_{1+x}Sn_{0.975}Sb_{0.025}$ and $Zr_{0.25}Hf_{0.75}Ni_{1+x}Sn_{0.99}Sb_{0.01}$ samples.

6.2.2 Thermoelectric properties

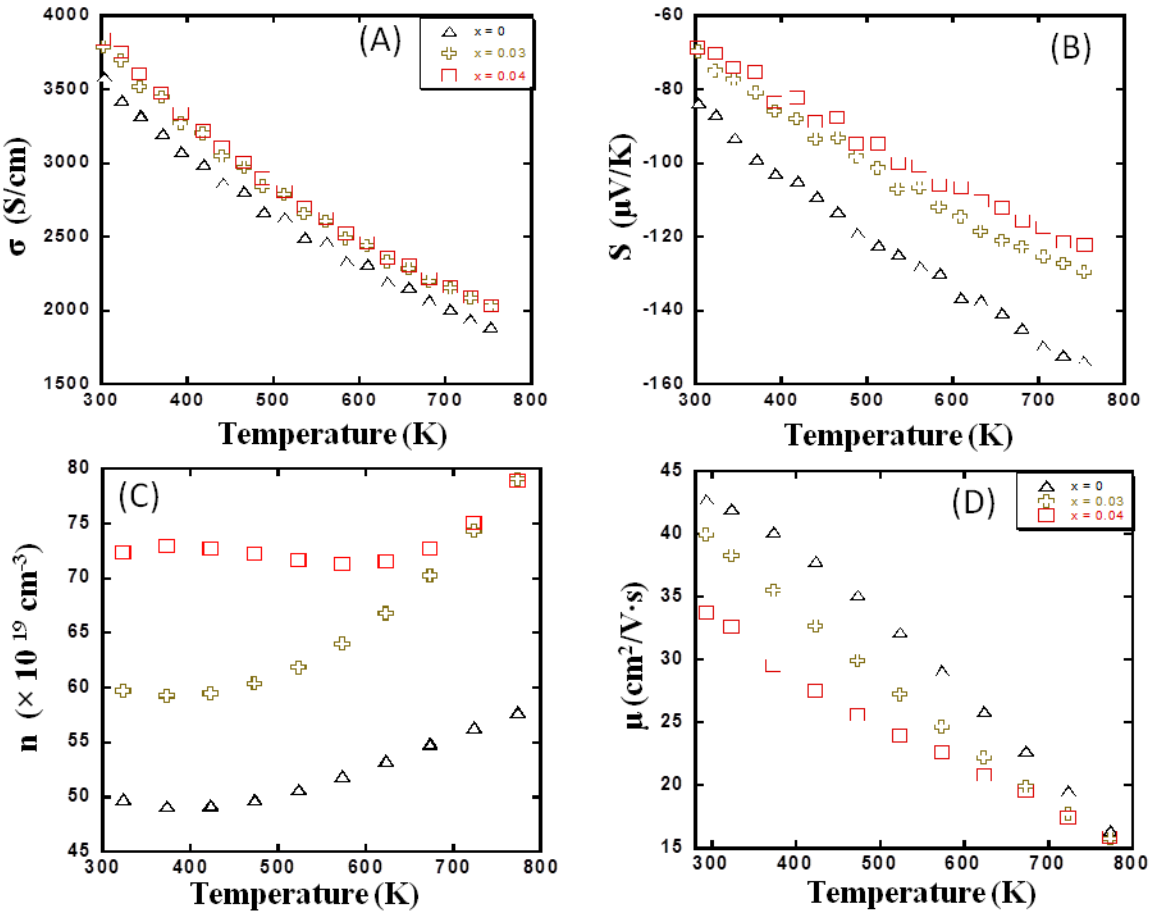

Figure 6.3 Temperature dependence of (A) electrical conductivity; (B) thermopower; (C) carrier concentration; and (D) mobility for $Zr_{0.25}Hf_{0.75}Ni_{1+x}Sn_{0.975}Sb_{0.025}$.

Figure 6.3A and 6.3B show the temperature dependence of the electrical conductivity and thermopower for $Zr_{0.25}Hf_{0.75}Ni_{1+x}Sn_{0.975}Sb_{0.025}$ FH/HH composites. In the temperature range 300K to 775 K; the electrical conductivity decreases with increasing temperature, which is consistent with heavily doped semiconducting behavior. Regardless of the temperature, the electrical conductivity increases with increasing Ni concentration. At 300K, the electrical conductivity for the matrix is ~3500 S/cm and increases to 3800 S/cm for samples with x = 0.03 and 0.04 is. At 775 K, the matrix still shows the lowest electrical conductivity ~ 1800 S/cm;

whereas the electrical conductivity for the samples with x = 0.03 and 0.04 decreases to 2000 S/cm.

All samples exhibit negative values of the thermopower (Figure 6.3B) in the measured temperature range indicating n-type semiconducting behavior. Within this temperature range, the thermopower for all samples increases almost linearly with increasing temperature, which is also consisting with heavily doped semiconducting behavior. Regardless of the temperature, the thermopower decreases with increasing Ni concentration. At 300K, the thermopower of the HH matrix (x = 0, y = 0.025) is -80 μV/K and increases to -160 μV/K at 775K. Upon increasing Ni concentration to x = 0.03 and 0.04, the thermopower drops to ~ -70 μV/K at 300K. However, the thermopower of samples with x = 0.03 and 0.04 increases to -125 μV/K and -110 μV/K, respectively, at 775K. The observed marginal difference in the thermopower of samples with x = 0.03 and 0.04 is surprising given the similarity in their electrical conductivity. To better understand the nature of electronic transport in $Zr_{0.25}Hf_{0.75}Ni_{1+x}Sn_{0.975}Sb_{0.025}$, Hall effect data are collected in the temperature range from 300K to 775K.

Figure 6.3C and 6.3D show the temperature dependence of carrier concentration and mobility for $Zr_{0.25}Hf_{0.75}Ni_{1+x}Sn_{0.975}Sb_{0.025}$ FH/HH composites extracted from Hall effect data. Regardless of the temperature, the carrier concentration increases with the excess Ni concentration. At 300K, the carrier concentration increases from 50 $\times 10^{19}$ cm^{-3} for the Sb-doped matrix to 60×10^{19} cm^{-3} for the sample with x = 0.03 and to 73×10^{19} cm^{-3} for the sample with x = 0.04. This increase in the carrier concentration with Ni content suggests the formation of metallic FH nanoparticles upon addition of excess elemental Ni in the Sb-doped HH matrix. Interestingly, the temperature above which thermal excitation of carriers from the valence to the conduction band occurs increase with increasing Ni content from 373K (x = 0) to 423K (x = 0.03) and 623K (x = 0.04).

At 775K, the carrier concentration is 57 $\times 10^{19}$ cm^{-3} for the HH matrix (x = 0) and ~ 80×10^{19} cm^{-3} for the samples with x = 0.03 and 0.04. The increased carrier concentration with excess Ni concentration is consistent with the electrical conductivity and suggests that metallic FH phase brings additional charge carrier to the HH matrix. Similar behavior was reported in various FH/HH composites containing large particles of the FH inclusions [11, 15]. It is interesting to note the large difference in the carrier concentration of samples with x = 0.03 and 0.04 at the temperature below 673K despite the similarity in their thermopower values in the same temperature range. This abnormal trend suggests larger carrier effective mass (m*) for the sample with x = 0.04 compared to the sample with x = 0.03. The mobility for all samples decreases with increasing temperature and increasing Ni concentration (Figure 6.3D). At 300K, the mobility for the matrix (x = 0), samples with x = 0.03 and 0.04 are 43 $cm^2/V \cdot s$, 40 $cm^2/V \cdot s$ and 35 $cm^2/V \cdot s$, respectively. The observed reduction in the mobility is consistent with the increase in carrier concentration with increasing Ni content. The above discussion suggests that under heavily doped condition electronic conduction in $Zr_{0.25}Hf_{0.75}Ni_{1+x}Sn_{0.975}Sb_{0.025}$ is controlled by the large fraction of high-energy extrinsic carriers. Similar behavior was reported in $Ti_{0.1}Zr_{0.9}Ni_{1+x}Sn_{0.975}Sb_{0.025}$ nanocomposites. In the $Zr_{0.25}Hf_{0.75}Ni_{1+x}Sn_{0.975}Sb_{0.025}$ nanocomposites, extrinsic carriers are provided by both Sb doping at Sn sites and additional doping from metallic FH inclusions. These dopants presumable occupy high-energy states in the conduction bands of HH matrix facilitating their transmission across the potential barrier at the nanoscale interface between HH matrix and sub-ten nanometer scale FH inclusion. Therefore, no significant reduction in the overall carrier concentration results from the anticipated filtering of low energy carriers at the FH/HH interfaces.

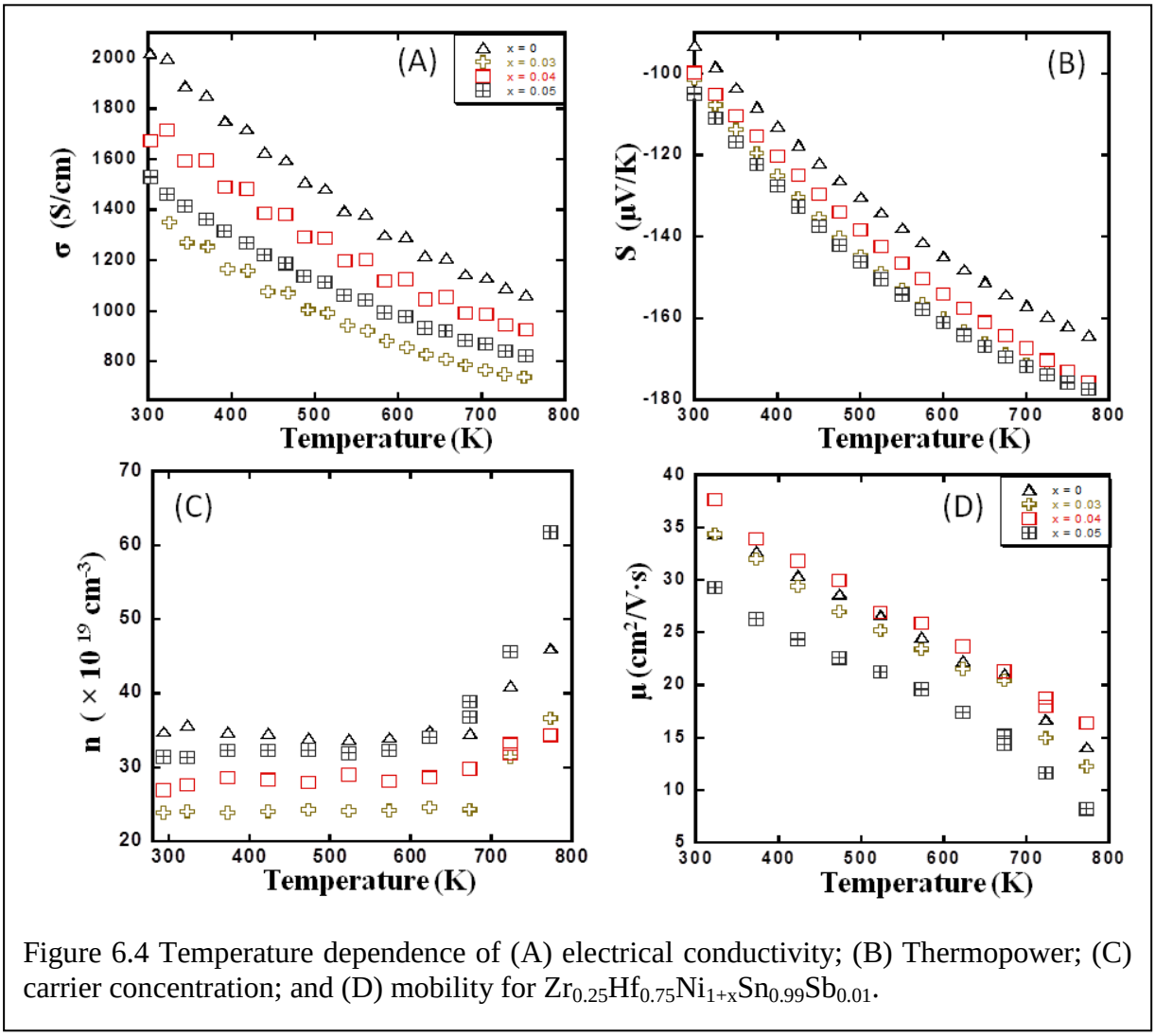

Figure 6.4 Temperature dependence of (A) electrical conductivity; (B) Thermopower; (C) carrier concentration; and (D) mobility for $Zr_{0.25}Hf_{0.75}Ni_{1+x}Sn_{0.99}Sb_{0.01}$.

To further explore the effect of FH/HH interface on the behavior of extrinsic carriers in bulk HH matrix, we have reduced the doping level to 1% Sb doping at Sn sites. Figure 6.4A shows the temperature dependence of the electrical conductivity for $Zr_{0.25}Hf_{0.75}Ni_{1+x}Sn_{0.99}Sb_{0.01}$ FH/HH composites. Compared to FH/HH composites with 2.5% Sb, analogous samples with 1% Sb has lower electrical conductivity. The electrical conductivity decreases with increasing temperature in the measured temperature range suggesting that the samples are heavily doped semiconductors. Regardless of the temperature, the electrical conductivity for $Zr_{0.25}Hf_{0.75}Ni_{1+x}Sn_{0.99}Sb_{0.01}$ samples

decreases with increasing Ni concentration, except for the sample with x = 0.03, which shows the lowest electrical conductivity (~ 1400 S/cm at 300K and 700 S/cm at 775K) in the measured temperature range. For instance, the electrical conductivity of 1% Sb doped HH matrix (x = 0) is 2000 S/cm at 300K. Upon addition of 4% excess Ni, the electrical conductivity at 300K decrease to ~1700 S/cm and further decreases to 1550 S/cm for the composition with x = 0.05.

The reduction in the electrical conductivity of $Zr_{0.25}Hf_{0.75}Ni_{1+x}Sn_{0.99}Sb_{0.01}$ samples compared to $Zr_{0.25}Hf_{0.75}Ni_{1+x}Sn_{0.975}Sb_{0.025}$ samples can be associated to: (1) decrease in the density of extrinsic carriers due to the reduction of the concentration of Sb dopant from 2.5% to 1%; and (2) additional reductions in the carrier concentration, for compositions with varying x values, due to energy filtering of carrier on the FH/HH interfaces. This analysis is supported by the carrier concentration measurement (Figure 6.4C) for various $Zr_{0.25}Hf_{0.75}Ni_{1+x}Sn_{0.99}Sb_{0.01}$ samples. At 300K, the carrier concentration for the 1% Sb-doped HH matrix is 35×10^{19} cm^{-3}, which is 30% lower than the value measured for the 2.5% Sb doped HH matrix. Upon addition of 3% excess Ni in the 1% Sb-doped HH matrix, the carrier concentration at 300K decreases to ~ 23×10^{19} cm^{-3}, which is 34% lower compared to 1% Sb doped HH matrix. Increasing the excess of elemental Ni to 4% and 5% resulted in a marginal increases at 300K to ~26×10^{19} cm^{-3} and 30×10^{19} cm^{-3}, respectively. Careful analysis of the temperature dependent carrier concentration curves for $Zr_{0.25}Hf_{0.75}Ni_{1+x}Sn_{0.99}Sb_{0.01}$ samples reveals that the carrier concentration initially remains unchanged upon increasing temperature up to a critical value, T_c, beyond which a nearly exponential increase in the carrier concentration with temperature is observed.

For the 1% Sb-doped HH matrix, thermal excitation of carriers from the valence band (VB) to the conduction band (CB) is observed at temperatures above T_c = 675 K. Interestingly, the critical temperature, T_c, for samples containing excess Ni decreases with increasing Ni content,

while the carrier concentration below T_c increases. However, the overall carrier concentration within samples with excess Ni concentration at a given temperature maintains lower than that of the 1% Sb-doped HH matrix indicating that no additional carriers were added to the matrix. For instance, the carrier concentration for the sample with x = 0.03 remains constant at 23 $\times 10^{19}$ cm^{-3} up to T_c = 675 K, upon increasing Ni content to x = 0.04, the carrier concentration increases to 26 $\times 10^{19}$ cm^{-3} and remains constant up to T_c = 625 K. Further increasing excess Ni content to x = 0.05 results in carrier concentration of 30 $\times 10^{19}$ cm^{-3} which remains constant up to T_c = 575 K. The observed change in the carrier concentration of $Zr_{0.25}Hf_{0.75}Ni_{1+x}Sn_{0.99}Sb_{0.01}$ samples with increasing Ni content and the temperature dependence of the carrier concentration can be explained by talking into account the relative alignment of conduction band at the FH/HH interfaces. For instance, the addition of excess Ni into a HH matrix results in the formation of coherent FH phase with varying particle size. The energy difference of conduction band minima (CBM) between the HH matrix and the FH inclusion generates an energy barrier, ΔE, at the FH/HH interface, the height of which increases with the reduction in size of the FH inclusion. Such potential energy barrier acts as filter to extrinsic carrier with low energy (Figure 6.5) while enabling transmission of extrinsic carriers with high energy.

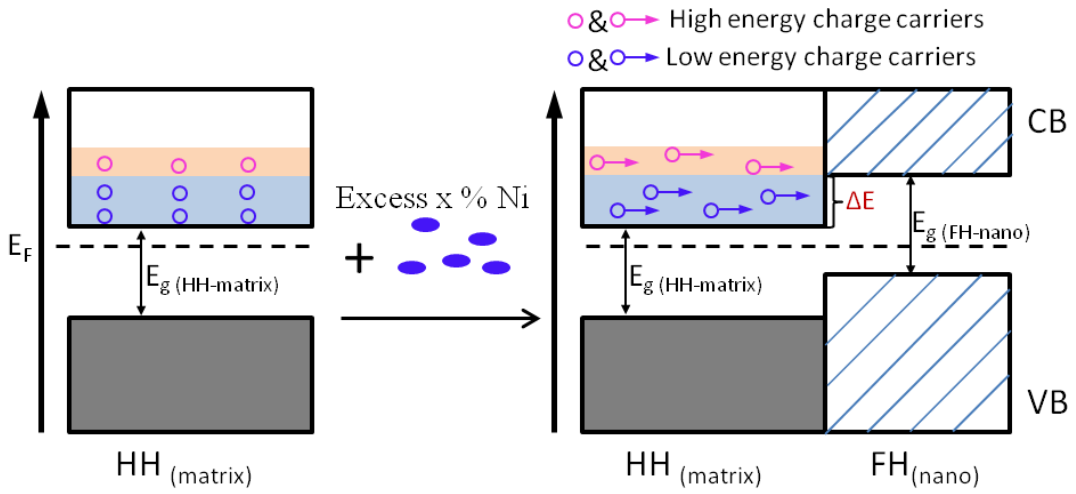

Figure 6.5 Proposed mechanism of excess Ni added into the HH matrix, the potential energy (ΔE) is formed at the interface between HH and FH.

Therefore, the temperature dependence of the carrier concentration for samples with x = 0.03, 0.04 and 0.05 at temperatures above T_c arises from the thermal excitation of existing extrinsic carriers with low energy across the potential barrier, ΔE, at the FH/HH interfaces, rather than from excitation of intrinsic carrier from valence band to conduction band as observed in the case of 1% Sb-doped HH matrix. This suggests that starting with the matrix with carrier concentration of 35 $\times 10^{19}$ cm^{-3}, the addition of increasing excess Ni results in the formation of FH nanostructures with increasing average particle size leading to the formation of potential energy barrier, ΔE, with decreasing height (Figure 6.5) at the heterojunction between HH matrix and FH nanoinclusions.

The observed reduction in the carrier concentration of $Zr_{0.25}Hf_{0.75}Ni_{1+x}Sn_{0.99}Sb_{0.01}$ with increasing Ni content results in an increase in the absolute value of the thermopower. For the thermopower (Figure 6.4B), the thermopower for all samples also exhibits negative value indicating n-type

semiconducting behavior. Regardless of the temperature, samples from $Zr_{0.25}Hf_{0.75}Ni_{1+x}Sn_{0.99}Sb_{0.01}$ shows larger thermopower value compared to corresponding samples (constant x) in $Zr_{0.25}Hf_{0.75}Ni_{1+x}Sn_{0.975}Sb_{0.025}$. This result is consistent with the reduction of the Sb doping level and carrier concentration. The thermopower of samples from the $Zr_{0.25}Hf_{0.75}Ni_{1+x}Sn_{0.99}Sb_{0.01}$ increases with rising temperature. At 300K, the thermopower of 1% Sb-doped matrix is -93 μV/K and rapidly increases to -163 μV/K at 775K. Upon addition of excess Ni, the thermopower value of samples with x = 0.03, 0.04 and 0.05 slightly increases to ~ -100 μV/K at 300K and -180 μV/K at 775K.

Figure 6.4D shows the temperature dependence of the mobility of 1% Sb-doped FH/HH samples. The mobility for all samples linearly decreases with increasing temperature. The matrix and samples with x = 0.03 shows similar value (35 $cm^2/V{\cdot}s$ at 300K) of the mobility in the temperature range. However, the sample with x = 0.04 displays a slightly higher (37 $cm^2/V{\cdot}s$ at 300K) carrier mobility compared to the 1% Sb-doped matrix, which is consistent with the observed decrease in the effective carrier concentration. Although the difference in the carrier concentration is clear, the changed in the mobility indicates the energy filtering effects in $Zr_{0.25}Hf_{0.75}Ni_{1+x}Sn_{0.99}Sb_{0.01}$ is weak which means the reduced carrier concentration did not significantly decrease electron - electron scattering in the samples. The sample with x = 0.05 has the lowest mobility value (30 $cm^2/V{\cdot}s$ at 300K) in the measured temperature range. This is consistent with the observed large carrier concentration. The fitting of the temperature dependence of the carrier mobility of $Zr_{0.25}Hf_{0.75}Ni_{1+x}Sn_{0.99}Sb_{0.01}$ using the power law $T^{-\lambda}$ results in λ values of 1.38 for the matrix, 1.30 for the sample with x = 0.03 and 1.60 for the sample with x = 0.05 indicating that optical phonon scattering dominates in these samples.

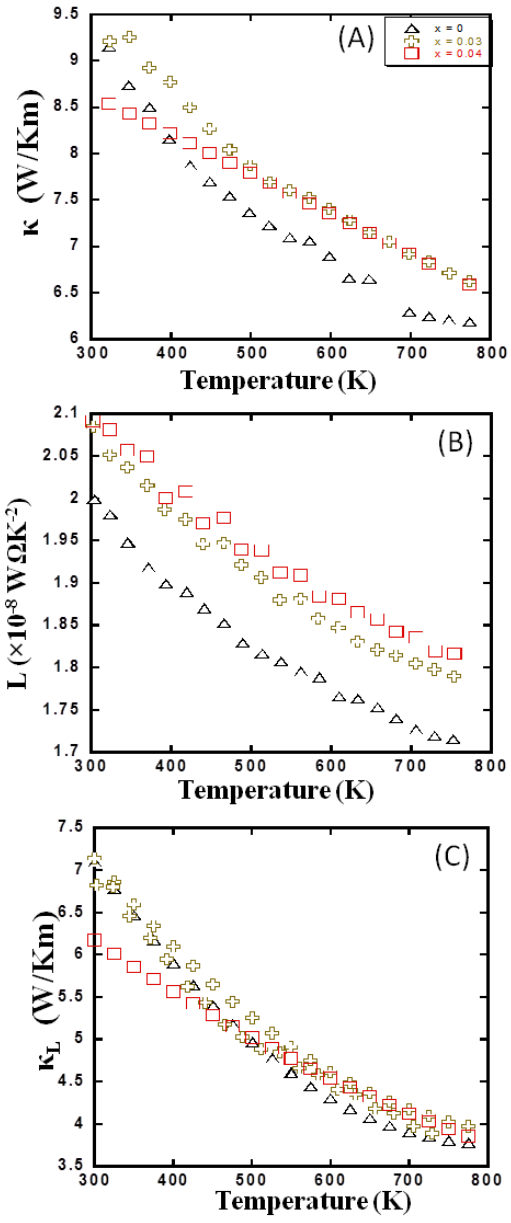

Figure 6.6 Temperature dependence of (A) total thermal conductivity; (B) Lorenz number and (C) lattice thermal conductivity for $Zr_{0.25}Hf_{0.75}Ni_{1+x}Sn_{0.975}Sb_{0.025}$.

Figure 6.6 shows the temperature dependence of the total thermal conductivity, Lorenz number and the lattice thermal conductivity for $Zr_{0.25}Hf_{0.75}Ni_{1+x}Sn_{0.975}Sb_{0.025}$ FH/HH composites. The total thermal conductivity for all samples decreases with increasing temperature (Figure 6.6A). At 300 K, sample with x = 0.04 has the lowest total thermal conductivity (~ 8.5 W/Km). Upon increasing the temperature above 500 K, similar values of the thermal conductivity is observed for samples with x =0.03 and 0.04. At 775K, a total thermal conductivity of 6.5 W/Km was observed for both compositions (x = 0.03 and 0.04); whereas the Sb-doped HH matrix shows the lowest thermal conductivity (6.2 W/Km).

The total thermal conductivity is the sum of electronic thermal conductivity (κ_{el}) and lattice thermal conductivity (κ_L). In order to determine the contribution of electronic thermal conductivity ($\kappa_e = L\sigma T$, where L is the Lorenz number, T is the absolute temperature), the Lorenz number is calculated from the experimental thermopower using a single parabolic band

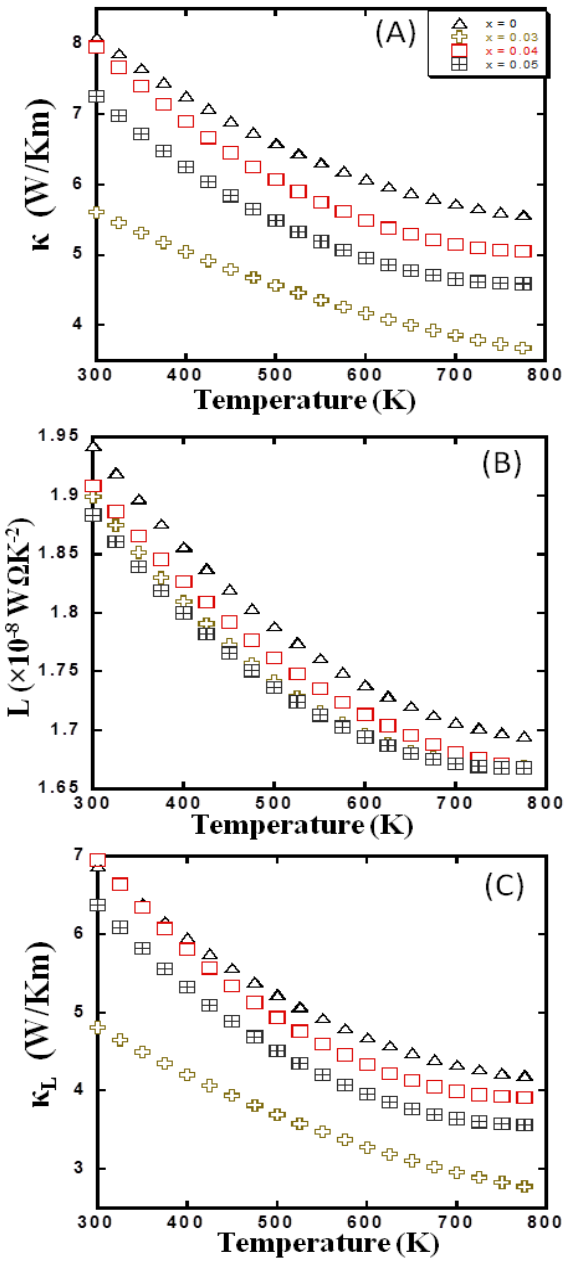

Figure 6.7 Temperature dependence of (A) total thermal conductivity; (B) Lorenz number and (C) lattice thermal conductivity for $Zr_{0.25}Hf_{0.75}Ni_{1+x}Sn_{0.99}Sb_{0.01}$.

(SPB) model (Figure 6.6B). The Lorenz number for all samples is lower than that of free electron model 2.45×10^{-8} $W\Omega K^{-2}$. Regardless of the temperature, the Lorenz number increases with increasing Ni concentration. At 300K, the Lorenz number for the matrix is 2×10^{-8} $W\Omega K^{-2}$; whereas a value of 2.1×10^{-8} $W\Omega K^{-2}$ was observed for the samples with x = 0.03 and 0.04. The lattice thermal conductivity (Figure 6.6C) was obtained by subtracting the electronic thermal conductivity from the total thermal conductivity. The matrix (x = 0) and the sample with x = 0.03 shows similar value of the lattice thermal conductivity at 300K (~7 W/Km); whereas the sample with x = 0.04 has the lowest lattice thermal conductivity at 300K (~ 6.2 W/Km). The reduction in the lattice thermal conductivity for the samples with x = 0.04 is probably due to the high density of FH/HH interfaces arising from increasing Ni content. Increasing the temperature results in a rapid drop of the lattice thermal conductivity of all samples to ~ 3.9 W/Km at 775K.

Figure 6.7 shows the temperature dependence of the total thermal conductivity, Lorenz number and the lattice thermal conductivity for $Zr_{0.25}Hf_{0.75}Ni_{1+x}Sn_{0.99}Sb_{0.01}$ FH/HH composites. The reduction in the concentration 1% Sb dopant results in lower total thermal conductivity for all $Zr_{0.25}Hf_{0.75}Ni_{1+x}Sn_{0.99}Sb_{0.01}$ samples when compared to the $Zr_{0.25}Hf_{0.75}Ni_{1+x}Sn_{0.975}Sb_{0.025}$ composites. This is due to the decrease in the density of extrinsic electrons (from Sb dopant), which will affect the electronic thermal conductivity. Regardless of temperature, the total thermal conductivity of $Zr_{0.25}Hf_{0.75}Ni_{1+x}Sn_{0.99}Sb_{0.01}$ composites first decreases to the lowest value as the Ni concentration increases to 3%, then the thermal conductivity increases with further increasing Ni concentration to 4% and 5%. The largest total thermal conductivity was observed

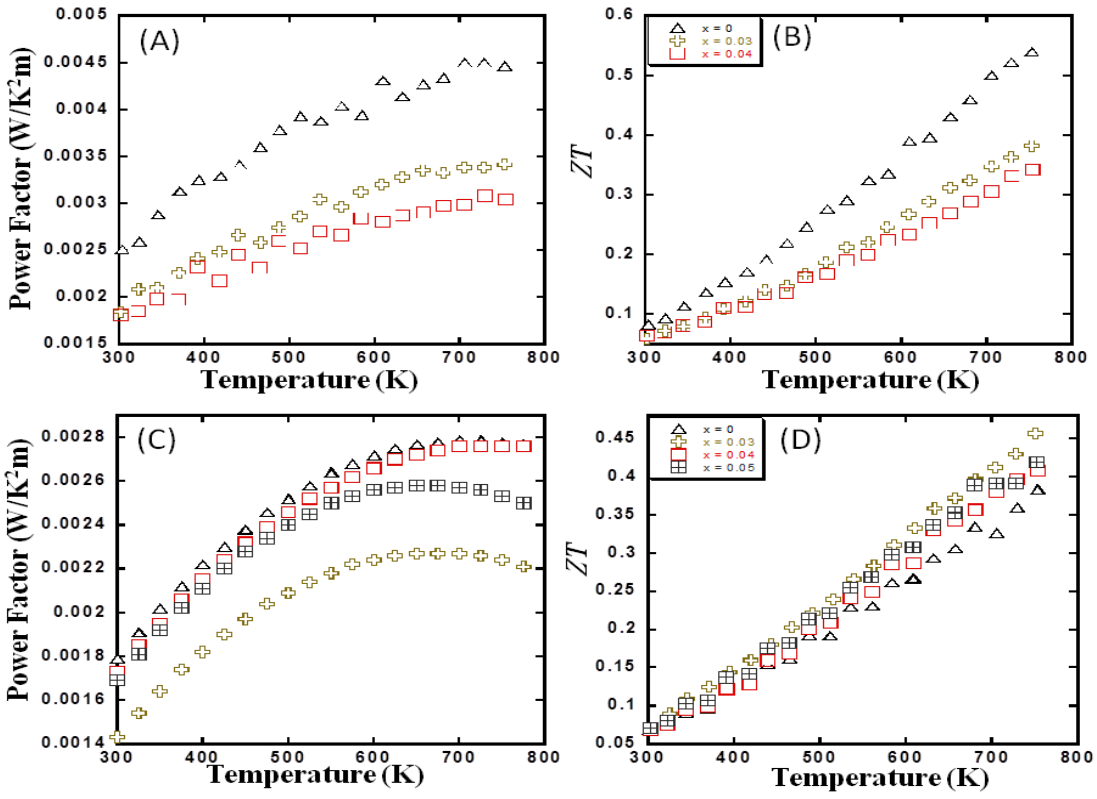

Figure 6.8 Temperature dependence of (A) Power factor, (B) ZT for the composites $Zr_{0.25}Hf_{0.75}Ni_{1+x}Sn_{0.975}Sb_{0.025}$; and (C) Power factor, (D) ZT for the composites $Zr_{0.25}Hf_{0.75}Ni_{1+x}Sn_{0.99}Sb_{0.01}$.

for the 1% Sb-doped HH matrix.

The Lorenz number was calculated according to the SPB model (Figure 6.7B) in order to extract the contribution from the electronic thermal conductivity. The Lorenz number for all 1% Sb-doped samples is lower than the values observed for $Zr_{0.25}Hf_{0.75}Ni_{1+x}Sn_{0.975}Sb_{0.025}$ composites. The matrix has the highest Lorenz number (1.95×10^{-8} $W\Omega K^{-2}$ at 300K) in the measured temperature range. Upon increasing Ni content to x = 0.03, 0.04 and 0.05, the Lorenz number decreases to 1.9×10^{-8} $W\Omega K^{-2}$ at 300K.

Regardless of the temperature, the lattice thermal conductivity (Figure 6.7C) decreases with increasing excess Ni concentration. At 300K, the sample with x = 0.03 shows the lowest value (~ 4.8 W/Km at 300K) of the lattice thermal conductivity. Although the lattice thermal conductivity for the samples with x = 0.04 and 0.05 slightly increases with increasing Ni content, the values remain lower than that of the matrix (7 W/Km at 300K). The reduction in the lattice thermal conductivity is attributed to phonon scattering from at the FH/HH interfaces.

The measured electrical conductivity and thermopower are used to evaluate the power factor for the $Zr_{0.25}Hf_{0.75}Ni_{1+x}Sn_{0.975}Sb_{0.025}$ composites (Figure 6.8A). The highest electrical conductivity and the thermopower observed for the 2.5% Sb-doped HH matrix resulted in the largest power factor in the measured temperature range. The combination of large power factor and low thermal conductivity for the 2.5% Sb-doped matrix leads to the largest ZT value of 0.55 at 775K (Figure 6.8B). Upon increasing Ni concentration to 3% and 4%, the power factor and ZT value decrease. The ZT value for the samples with x = 0.03 and 0.04 are respectively, 0.4 and 0.35 at 775K.

Samples of the $Zr_{0.25}Hf_{0.75}Ni_{1+x}Sn_{0.99}Sb_{0.01}$ composites show lower power factor than that of composites with 2.5% Sb substitution. This is due to the reduction in the electrical conductivity. At 300K, the matrix and the samples with x = 0.04 and 0.05 show similar power factor (18×10^{-4} $WK^{-2}m^{-1}$), while the sample with x = 0.03 exhibits the lowest power factor value (14×10^{-4} $WK^{-2}m^{-1}$. However, the ZT values for all 1% Sb-doped samples do not change significantly at low temperatures, despite large difference in the power factor. The highest ZT value of 0.46 is observed at 775K for the sample with x = 0.03.

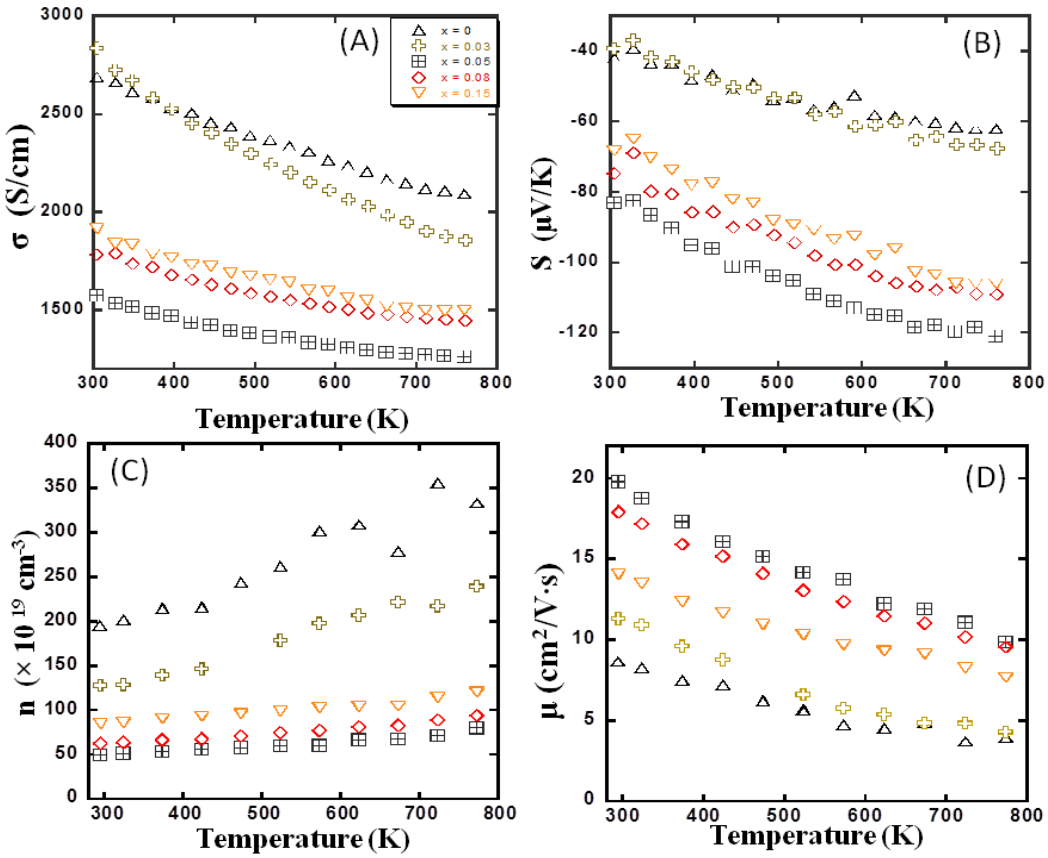

Figure 6.9 Temperature dependence of (A) electrical conductivity; (B) thermopower; (C) carrier concentration and mobility for $Zr_{0.25}Hf_{0.75}Ni_{1+x}Sn_{0.995}Sb_{0.00/5}$.

Figure 6.9A shows the temperature dependence of electrical conductivity for $Zr_{0.25}Hf_{0.75}Ni_{1+x}Sn_{0.995}Sb_{0.005}$. Regardless of the temperature, the electrical conductivity is lower than that of $Zr_{0.25}Hf_{0.75}Ni_{1+x}Sn_{0.975}Sb_{0.025}$. The electrical conductivity for all samples decreases with increasing temperature suggesting heavily doped semiconducting behavior. The electrical conductivity of $Zr_{0.25}Hf_{0.75}Ni_{1+x}Sn_{0.995}Sb_{0.005}$ samples in the measured temperature range decrease with Ni concentration. The matrix has the highest value of the electrical conductivity (2700 S/cm at 300K). When Ni concentration increases to 5%, the electrical conductivity reaches the lowest value (1500 S/cm at 300K); and remains nearly unchanged with further increasing Ni concentration to 8% and 15%. It should be noted that the electrical conductivity for the samples with excess Ni concentration keep the lower or equal value to the matrix in the measured temperature range.

The thermopower for all $Zr_{0.25}Hf_{0.75}Ni_{1+x}Sn_{0.995}Sb_{0.005}$ samples almost linearly decreases with increasing temperature and maintained negative values indicating n-type semiconducting behavior (Figure 6.9B). Regardless of temperature, the thermopower increases with Ni concentration. The matrix and the sample with x = 0.03 has similar thermopower (-40 μV/K at 300K and -65 μV/K at 775K). As the Ni concentration increases to 5%, the thermopower increases to -80 μV/K at 300 K, which corresponds to 200% enhancement compared to the 0.5%Sb-doped matrix. Further increasing the Ni concentration to 8% and 15% resulted in a slight drop in the thermopower to -75 μV/K and -70 μV/K at 300K, respectively. However, the observed values remain larger than that of the 0.5%Sb-doped matrix.

Figure 6.9C shows the temperature dependence of the carrier concentration for $Zr_{0.25}Hf_{0.75}Ni_{1+x}Sn_{0.995}Sb_{0.005}$. It is interesting to note that despite the low Sb-doping level, the carrier concentration in all $Zr_{0.25}Hf_{0.75}Ni_{1+x}Sn_{0.995}Sb_{0.005}$ samples is one-order of magnitude

higher than that of $Zr_{0.25}Hf_{0.75}Ni_{1+x}Sn_{0.975}Sb_{0.025}$ and $Zr_{0.25}Hf_{0.75}Ni_{1+x}Sn_{0.99}Sb_{0.01}$ samples. The measured carrier density of 200×10^{19} cm^{-3} at 300K is 20 times larger than the increase in the carrier density expected from the substitution of 0.5% Sn by Sb in $Zr_{0.25}Hf_{0.75}NiSn$ matrix. This suggests the formation of trace amount of metallic second phases in the 0.5% Sb-doped HH matrix during the mechanical alloying process. These metallic phases provide additional extrinsic carriers to the matrix leading to larger overall effective carrier concentration. Regardless of the temperature, the carrier concentration decreases with increasing Ni concentration. This suggests that a large fraction of the additional extrinsic carriers are affected by the energy filtering effect and the HH/FH interfaces, unlike extrinsic carriers from Sb-doping, which are generally not affected. The 0.5% Sb-doped matrix displays the highest carrier concentration in the measured temperature range (200×10^{19} cm^{-3} at 300K and 360×10^{19} cm^{-3} at 775K). As the excess Ni concentration increases to 3%, the carrier concentration drops to 125×10^{19} cm^{-3} at 300K. The carrier concentration further decreases to the lowest value, 50×10^{19} cm^{-3} at 300K as the excess Ni increases to 5%, which is corresponds to 75% drop compared to the 0.5% Sb-doped matrix. However, when the Ni concentration increases to 8% and 15%, the carrier concentration of the resulting composites slightly increases to 60×10^{19} cm^{-3} and 90×10^{19} cm^{-3} at 300K, respectively. Interestingly, these values of the carrier density remain lower than that of the 0.5% Sb-doped matrix. The marginal increase in the carrier density can be ascribed to additional doping arising from the formation of large FH metallic nanoinclusions in the matrix. These additional carriers from FH inclusions are presumably not affected by the potential barrier ate the HH/FH interfaces, whereas extrinsic carriers from impurities phases form during mechanical alloying are still subjected to the filtering effect.

The large increase in the carrier concentration in $Zr_{0.25}Hf_{0.75}Ni_{1+x}Sn_{0.995}Sb_{0.005}$ samples resulted in drastic drop in the carrier mobility when compared to $Zr_{0.25}Hf_{0.75}Ni_{1+x}Sn_{0.975}Sb_{0.025}$ and $Zr_{0.25}Hf_{0.75}Ni_{1+x}Sn_{0.99}Sb_{0.01}$ composites. The 0.5% Sb-doped matrix showed the lowest mobility (~ 8 $cm^2V^{-1}s^{-1}$) at 300K. However, the carrier mobility rapidly increases with increasing excess Ni, reaching a maximum of ~20 $cm^2V^{-1}s^{-1}$ at 300K for the composition with x = 0.05 and slightly decreases with further increase in excess Ni concentration to x = 0.08 (18 $cm^2V^{-1}s^{-1}$ at 300K) and 0.15 (14 $cm^2V^{-1}s^{-1}$ at 300K). This trend is consistent with the observed variation of carrier density with excess Ni. The reduction in the overall carrier density and enhancement of the carrier mobility observed in various $Zr_{0.25}Hf_{0.75}Ni_{1+x}Sn_{0.995}Sb_{0.005}$ samples (x = 0.03, 0.05, 0.08 and 0.15) compared to the 0.5% Sb-doped matrix, can be explained by the concept of energy filtering of low-energy charge carriers at the HH/FH interfaces, which provides a plausible description of the behavior of charge carriers in HH matrices containing sub-ten nanometer scale FH inclusions (Figure 6.2A)[3, 5, 7].

However, HH matrices containing sufficiently large FH inclusions generally display higher carrier density than the pristine HH matrix (without FH inclusion) due to the metallic behavior of large FH inclusions. Additional carriers arising from the doping of the HH matrix by the metallic FH inclusions presumably occupy states with energy higher than the potential barrier at the HH/FH interfaces resulting in their contribution to the electronic conduction [4].

This explains the slight increase in the carrier density and drop in the carrier mobility for samples with x = 0.08 and x = 0.15 (Figure 6.9C and 6.9D) in which the high population density of FH nanoinclusions lead to the agglomeration of some of them into large metallic FH particles.

Figure 6.10 shows the temperature dependence of the total thermal conductivity, Lorenz number and the lattice thermal conductivity for FH/HH composites $Zr_{0.25}Hf_{0.75}Ni_{1+x}Sn_{0.995}Sb_{0.005}$. The total thermal conductivity increases with increasing temperature suggesting bipolar conduction (Figure 10A). Regardless of the temperature, the total thermal conductivity decreases with increasing Ni concentration, which is consistent with the observed drop in the electrical conductivity. The total thermal conductivity for all samples is lower than that of composites with 1% and 2.5% Sb-doped HH matrix. The highest thermal conductivity, 7.2 $WK^{-1}m^{-1}$, is observed at 300K for the 0.5% Sb-doped matrix and the sample with x = 0.03. The total thermal conductivity drastically drops to 5.7 $WK^{-1}m^{-1}$ at 300K for samples with x = 0.05, 0.08 and 0.15.

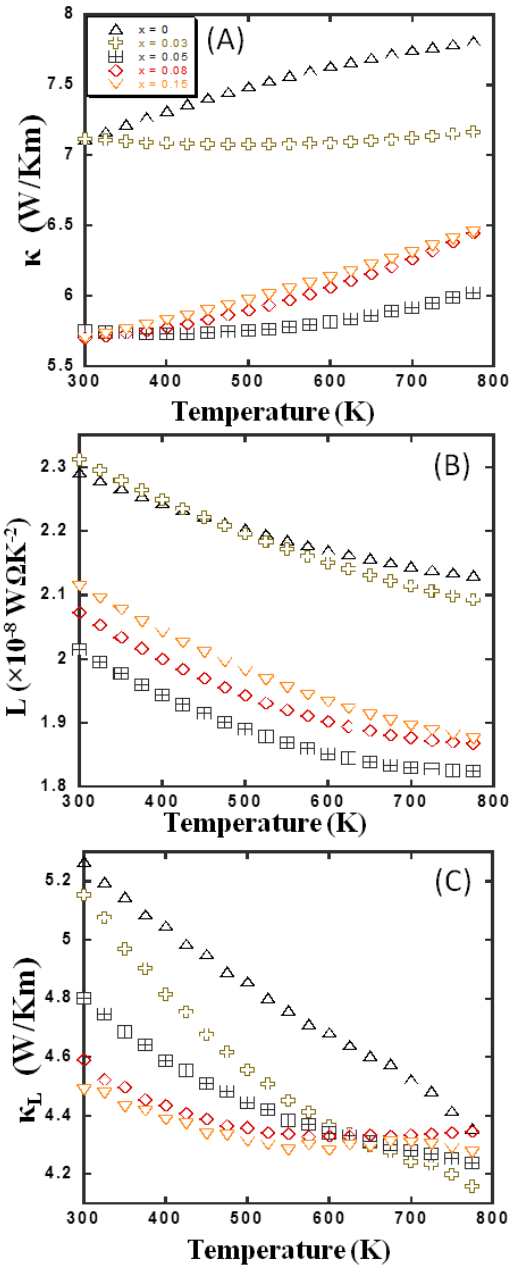

Figure 6.10 Temperature dependence of (A) total thermal conductivity; (B) Lorenz number and (C) lattice thermal conductivity for $Zr_{0.25}Hf_{0.75}Ni_{1+x}Sn_{0.995}Sb_{0.005}$.

In order to analysis the electronic thermal conductivity, Lorenz number was calculated using SPB model (Figure 6.10B). The matrix and the sample with x = 0.03 have higher Lorenz number (2.3×10^{-8} $W\Omega K^{-2}$) at 300K, which is closed to the Lorenz

number for free electron. When Ni concentration increases to 5%, the Lorenz number decreases to 2×10^{-8} $W\Omega K^{-2}$ at 300K. Further increasing Ni concentration to 8 % and 15 % resulted in a small increase of the Lorenz number respectively, to 2.08×10^{-8} $W\Omega K^{-2}$ and 2.1×10^{-8} $W\Omega K^{-2}$ at 300K.

The lattice thermal conductivity decreases with increasing Ni concentration. At 300K the lattice thermal conductivity for the matrix is 5.3 $WK^{-1}m^{-1}$ and drops to 4.5 $WK^{-1}m^{-1}$ at 300K for the sample with x = 0.15. This corresponds to 15% reduction compared to the 0.5% Sb-doped matrix. This reduction in the lattice thermal conductivity is attributed to enhance phonon scattering due to a large increase in the density of HH/FH interfaces with increasing excess Ni.

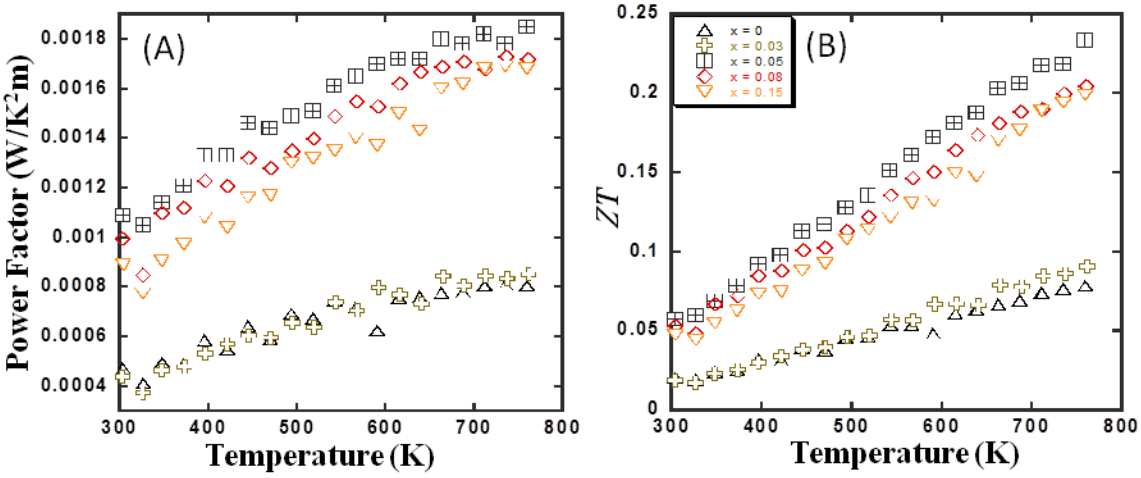

Figure 6.11 Temperature dependence of (A) power factor and (B) ZT for $Zr_{0.25}Hf_{0.75}Ni_{1+x}Sn_{0.995}Sb_{0.005}$.

Figure 6.11A shows the power factor calculated using the electrical conductivity and thermopower data. The large increase in the thermopower induced by the energy filtering of carriers at HH/FH nanointerfaces, offsets the reduction in the electrical conductivity leading to improvement in the overall powder factor for samples with x = 0.03, 0.05, 0.08 and 0.15. The sample with x = 0.05 showed the highest value of the PF in the measured temperature range. The combination of large improvement in the power factor and reduction in the thermal conductivity

in the sample with x = 0.05 resulted in drastic increase of the ZT at 775K from ~0.05 for 0.5% Sb-doped matrix to ~0.24, which corresponds to an enhancement of ~ 67%.

6.3 Conclusion

In summary, we have investigated the effectiveness of potential energy barrier, ΔE, at HH/FH interfaces in filtering charge carriers within HH matrix with various doping levels. We found that starting from HH matrices containing equal volume fraction of FH nanoinclusions with similar average size range, the filtering effect of the potential energy barrier at the HH/FH interfaces on the electronic transports of existing intrinsic and extrinsic charge carriers strongly depends on the relative fraction of extrinsic carriers as they energy distribution within the HH matrix. In the current study, extrinsic carriers in various HH matrices ($Zr_{0.25}Hf_{0.75}NiSn_{1-y}Sb_y$) were introduced either intentionally using Sb substitutions at Sn sites or unintentionally through doping of the matrix by (1) large metallic FH inclusions and/or (2) unknown impurities introduced during the mechanical alloying process. We observed that for $Zr_{0.25}Hf_{0.75}Ni_{1+x}Sn_{1-y}Sb_y$ samples in which electronic conduction is dominated by extrinsic carriers arising from doping through Sb substitutions at Sn sites and from doping by large metallic FH inclusions (y = 0.01 and 0.025), the introduction of HH/FH interfaces through addition of excess elemental Ni (x) resulted in constant or larger overall carriers density (y = 0.025) or to a marginal drop in the carrier density (y = 0.01) compared to the pristine HH matrix. This suggests that a large fraction of extrinsic carriers in these samples are located at energy levels higher than the potential energy barrier at the HH/FH interfaces. Therefore, the low-energy intrinsic carriers trapped at the HH/FH interfaces represent a very small fraction of conduction electrons leading to virtually no effect on

the overall effective carrier density. However, for the mechanically alloyed $Zr_{0.25}Hf_{0.75}Ni_{1+x}Sn_{0.995}Sb_{0.005}$ samples, we observed a drastic decrease in the effective carrier density upon introduction of HH/FH interfaces. This suggests that a large fraction of extrinsic carriers in these samples are located at low energy levels within the HH matrix and are therefore trapped by the potential energy barrier at the HH/FH interfaces. One can derive from this analysis that extrinsic carriers introduced by unknown impurities during the mechanical alloying process occupy lower energy states within the HH matrix, whereas extrinsic carriers from Sb doping at Sn sites or from the formation of metallic FH inclusions are located at higher energy states. This work demonstrates the effectiveness of the potential energy barrier at HH/FH interfaces to discriminate between dopants with various energy levels in heavily doped HH semiconductors. Therefore, the optimization of the thermoelectric properties of semiconductors through synergetic integration of the concepts of doping and energy-filtering through nanostructuring requires a good match between (1) the type of doping element (energy level occupied by contributed carriers) and (2) the average size and distribution (the heights of the potential energy barrier) of the nanostructures coherently embedded inside the semiconducting matrix.

CHAPTER 7

THERMOELECTRIC BEHAVIOR OF NANOSTRUCTURED $Zr_{0.25}Hf_{0.75}NiCo_XSn$ HALF-HEUSLER ALLOYS

7.1 Objective

In this work, we expand our investigation of carriers and thermal transports in HH (1-x)/FH(x) nanocomposites to systems in which Co-containing FH nanoinclusions are embedded in n-type Ni-based HH matrix $Zr_{0.25}Hf_{0.75}NiSn$. Starting from a HH matrix with composition $Zr_{0.25}Hf_{0.75}NiSn$, incremental amount of Co element was added through solid-state atomic interdiffusion during high temperature reaction. This results in the formation of FH phase with composition $Zr_{0.25}Hf_{0.75}NiCoSn$ as nanoinclusion in HH matrix. The synthesized $Zr_{0.25}Hf_{0.75}NiSn$/ $Zr_{0.25}Hf_{0.75}NiCoSn$ (HH/FH) composites were characterized by XRD and HRTEM. The effects of FH phase on the thermoelectric properties for HH + x Co nanocomposites were investigated. XRD pattern revealed the presence of FH peaks indicating the formation of large FH nanoparticles. We found that the FH nanoparticles are coherently embedded in the HH matrix, the size of nanoinclusion increased from 1~3 nm to 20~50 nm with increasing Co concentration. It is remarkable that the electrical conductivity significant increased (~ 792 S/cm at 300K) for Co concentration ≥ 5 wt%. Temperature dependent electrical conductivity for sample with various Co concentration indicated transitions from intrinsic

semiconducting behavior to heavily doped semiconducting behavior. The thermopower decreases with increasing Co concentration, which is consistent with the change in the electrical conductivity. However, the lattice thermal conductivity decreased with increasing Co concentration indicating enhanced phonon scattering at the multiple HH/FH interfaces within the nanocomposites.

7.2 Result and discussion

7.2.1 Phase characterization

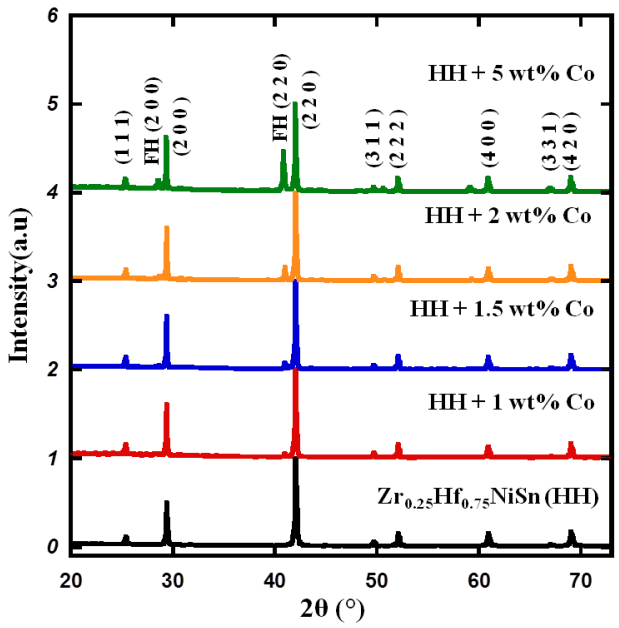

Figure 7.1 Powder XRD pattern of the synthesized composites compared to that of the half-Heusler matrix.

Powder X-ray diffraction of the as-synthesized $Hf_{0.25}Zr_{0.75}NiSn$ (HH) matrix and the FH/HH composites (HH + x wt% Co) samples are shown in Figure 7.1. All peaks of the HH matrix XRD pattern are consistent with the cubic MgAgAs-type structure, suggesting the formation of single phase. The calculated unit cell parameter is a = 6.165 Å. As excess Co is added to the matrix, additional peaks corresponding to the FH structure ($MnCu_2Al$-type) are observed. The refined unit cell parameter, a = 6.253 Å, is larger than that of the HH matrix, which is consistent with the insertion of additional Co into the vacant site of HH structure. Peaks of HH phase in the composites do not shift in position, indicating that the added Co elements do not form interstitial of substitutional solid-solution with the HH matrix.

In addition, peaks of the FH phase in the XRD patterns of samples with increasing Co concentrations also maintain at the same position (same 2θ value), but increase in intensity with Co concentration. This suggests that the reaction of Co element with $Hf_{0.25}Zr_{0.75}NiSn$ matrix does not lead to the formation of (1) an intermediate phase, $Hf_{0.25}Zr_{0.75}NiCo_xSn$, with increasing Co content or (2) two separate FH phases, $Hf_{0.25}Zr_{0.75}Ni_2Sn$ and $Hf_{0.25}Zr_{0.75}Co_2Sn$, with various mole fractions. Instead Co completely reacts with $Hf_{0.25}Zr_{0.75}NiSn$ matrix to form FH precipitates according to the Eq. (1).

$$Hf_{0.25}Zr_{0.75}NiSn + x\ Co \rightarrow (1\text{-}x)\ Hf_{0.25}Zr_{0.75}NiSn\ (HH\ matrix) + x\ Hf_{0.25}Zr_{0.75}NiCoSn\ (FH) \quad (1)$$

It should be noted that the composition of the FH phase, $Hf_{0.25}Zr_{0.75}NiCoSn$, represents a 50% solid-solution between the possible FH phases, $Hf_{0.25}Zr_{0.75}Ni_2Sn$ and $Hf_{0.25}Zr_{0.75}Co_2Sn$, that could also be anticipated from such reaction. The formation of a solid-solution rather than two competing separate phases is favored, not only by the similarity in the lattice parameters of $Hf_{0.25}Zr_{0.75}Ni_2Sn$ and $Hf_{0.25}Zr_{0.75}Co_2Sn$ phases, but also because the formation of the $Hf_{0.25}Zr_{0.75}Co_2Sn$ phase would require complete dissolution of the original HH structure and long range diffusion of Ni out of the tetrahedral sites[106-107]. The energy cost for such mechanism is higher than the formation of a 50% solid-solution through dissolution of excess Co into tetrahedral vacancies [108-110], which is represents 50% of the available tetrahedral sites in the $Hf_{0.25}Zr_{0.75}NiSn$ structure.

As can be anticipated from the chemical reaction in Eq.(1), the mole fraction of the FH phase, $Hf_{0.25}Zr_{0.75}NiCoSn$, increases with increasing concentration of excess elemental Co in the stating mixture. For example, the sample with 1 wt% Co shows a very weak FH peak at ~41º (200);

whereas the corresponding FH peak (200) on the XRD pattern of the sample with 5 wt% Co is observable and strong (Figure 7.1).

7.2.2 Microstructural analysis

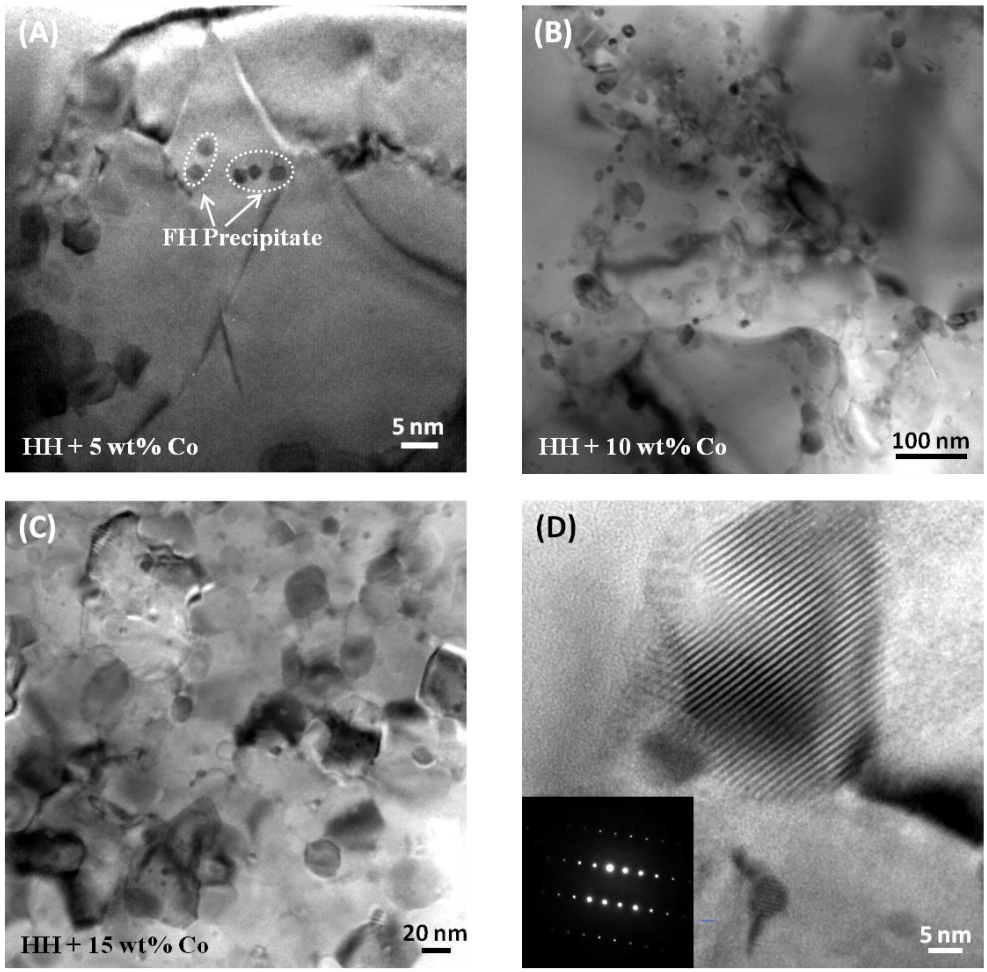

Figure 7.2 TEM images of selected FH/HH bulk composites. Low-magnification image of the sample with 5 wt% Co (A); 10 wt% Co (B); and 15 wt% Co (C); (D) high-magnification image of FH nanoparticle from the sample with 5 wt% Co and selected–area electron diffraction (insert of D).

Figure 7.2 shows the microstructure of selected $Hf_{0.25}Zr_{0.75}NiSn$/ $Hf_{0.25}Zr_{0.75}NiCoSn$ (HH/FH) bulk composites. Nearly spherical dark precipitates with sizes ranging from 1 to 3 nm can be observed in the low-magnification TEM image of the sample with 5 wt% Co (Figure 7.2A). Upon increasing the concentration of excess elemental Co to 10 wt%, a higher density of the

spherical dark precipitates is observed in a large area of the HH matrix (Figure 7.2B). Some of these small precipitates agglomerate to form large particles with size ranging from 20 to 50 nm. Further increasing the Co concentration to 15 wt% resulted to the agglomeration of the small precipitates into interconnected network (Figure 7.2C). High magnification TEM image for the sample with 5 wt% Co shows that the dark precipitates are highly crystalline and coherently embedded in the HH matrix (Figure 7.2D). The lattice parameter of the precipitate is ~ 0.63 nm, which is comparable to the lattice parameter of the FH phase calculated from the XRD powder pattern and the selected-area electron diffraction (insert of Figure 7.2D). This result confirms the fcc FH structure of the observed nanoinclusions and is consistent with the XRD analysis.

7.2.3 Thermoelectric properties

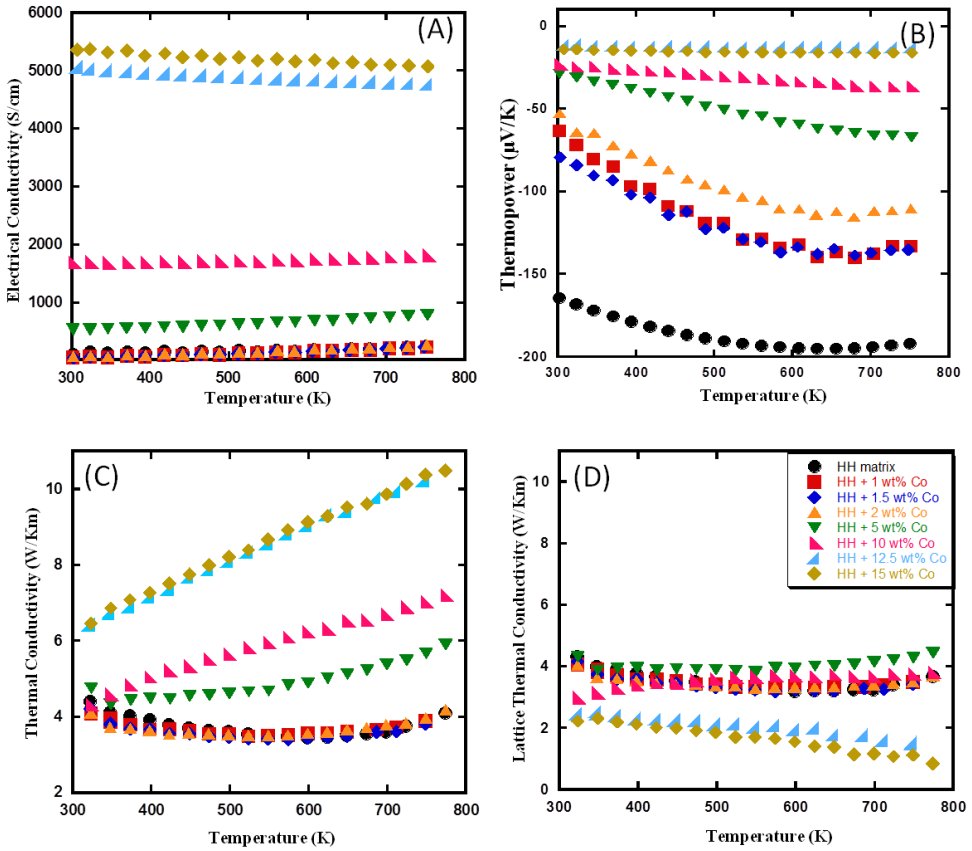

Figure 7.3 Temperature dependence of (A) electrical conductivity; (B) thermopower; (C) total thermal conductivity; (D) lattice thermal conductivity of bulk $Hf_{0.25}Zr_{0.75}NiSn$/ $Hf_{0.25}Zr_{0.75}NiCoSn$ (HH/FH) composites.

Figure 7.3A shows the temperature dependence of the electrical conductivity of various (1-x) HH/(x) FH bulk composites in the temperature range from 300K to 775K. Regardless of the temperature, the electrical conductivity of (1-x) HH/(x) FH composites increases with increasing Co concentration in the starting mixture. Various (1-x) HH/(x) FH composites can be grouped into three categories based on the temperature dependence curves of the electrical conductivity. For HH/FH composites with low Co concentration ($x \leq 5$ wt %), the electrical conductivity increases with rising temperature, indicating intrinsic semiconducting behavior. The room temperature electrical conductivity of the matrix and samples with 1 wt%, 1.5 wt% and 2 wt%

Co is below 100 S/cm, whereas the sample with 5 wt% Co displays a higher electrical conductivity (~ 537 S/cm) at 300K. When the temperature increases to 775 K, sample with 5 wt% Co still shows higher electrical conductivity (~ 792 S/cm at 775 K) than samples with lower Co concentration. The observed increase in electrical conductivity with increasing Co concentration suggests that the FH inclusions formed within the HH matrix contribute additional carriers leading an increase in the carrier concentration. Further increasing the Co concentration to 10wt% resulted in an increase of the electrical conductivity to ~1800 S/cm at 300K. The electrical conductivity of this sample remains nearly temperature independent suggesting a semimetal-like character. This suggests that metallic FH phase is formed upon addition of more Co to the HH matrix. At sufficiently high concentration of excess Co ($x \geq 12.5\%$), percolation between metallic FH precipitates (Figure 7.2B) leads to large electrical conductivity values. At 300 K, the electrical conductivity of samples with 12.5 wt% and 15 wt% Co are 5051 S/cm and 5359 S/cm, respectively. The electrical conductivity of these samples decreases with rising temperature, suggesting metallic or heavy doped semiconducting behavior. At 775 K the electrical conductivity of 12.5 wt% Co and 15 wt% Co samples is 4781 S/cm and 5084 S/cm, respectively. The observed large electrical conductivity of these samples is associated with the large carrier density of the metallic FH phases.

Figure 7.3B shows the temperature dependence of the thermopower of the synthesized HH/FH composites. All samples exhibit negative thermopower values in the measured temperature range indicating n-type semiconductor. The thermopower of all samples increases with rising temperature. Regardless of temperature, the thermopower of various composites decreases with increasing Co concentration, which is consistent with the observed large increase in the electrical conductivity. Largest thermopower values are observed for the pristine HH

matrix (-164 μV/K at 300K and -192 μV/K at 775 K). Surprisingly, the thermopower decreases drastically to ~ -60 μV/K at 300 K, upon addition of 1 wt% to 2 wt% excess Co into the HH matrix whereas only a marginal increase is observed in the electrical conductivity. This suggested that the Co-containing FH (Co-FH) inclusions formed within the n-type HH matrix act as p-type dopants leading to a large drop in the thermopower due to bipolar conduction. Further increasing the Co concentration to above 5 wt% resulted in a dramatic drop of the thermopower to -15 μV/K at 300 K. The observed drop in the thermopower with increasing Co concentration arises from an increased contribution of holes from the p-type Co-FH phase to the electronic conduction within the n-type HH matrix. It is interesting to note that samples with low Co concentration (Co ≤ 5 wt%) shows strong temperature dependence of the thermopower. Below 650K, the thermopower of samples with less than 5 wt% Co gradually increase with temperature reaching a maximum value around 650K. Further increase in the temperature resulted in minimal decrease in the thermopower. The maximum value of the thermopower at 650K suggests that thermally excited intrinsic carriers also participate to the conduction above this temperature. The estimated band gaps are 0.26 eV for the matrix, 0.18 eV for the sample with 1 wt% Co and 0.13 eV for the sample with 2 wt% Co. However, the sample with 10 wt% Co concentration shows a weak temperature dependence of the thermopower with a linear increase over the whole temperature range. For the sample with 12.5 wt% and 15 wt% Co, the thermopower remain almost constant in the measured temperature range. The observed alternation in the temperature dependence of thermopower for the samples with various Co concentrations can be explained by change in the conduction type from semiconducting to metallic behavior[111]. Starting with a semiconducting HH matrix with a band gap of 0.26 eV, additions of excess Co resulted in the formation of impurity states within the band gap due to the formation of metallic FH phase. This

reduced the band gaps of the composite leading to an increase in the carrier density at a given temperature. For high enough excess Co (≥ 12.5 wt%), the band gap completely vanishes resulting in the observed metallic behavior.

Figure 7.3C and 7.3D show the temperature dependence of the total thermal conductivity and lattice thermal conductivity of FH/HH bulk composites. The total thermal conductivity of the synthesized composites increases with rising temperature. Regardless of the temperature, the total thermal conductivity increases with increasing Co concentration. At 300 K, the matrix and samples with less than 10 wt% excess Co have similar total thermal conductivity (~ 4.2 W/Km), whereas samples with 12.5 wt% and 15 wt% Co showed higher total thermal conductivity (6.1 W/Km at 300K). As the temperature increases, the total thermal conductivity of the matrix and samples with low Co concentration (x ≤ 2 wt% Co) decreases to 4 W/Km at 775K. However, the total conductivity of samples with 5 wt%, 10 wt%, 12.5 wt% and 15 wt% Co increases from 6 W/Km at 300 K to 13 W/Km at 775K. The lattice thermal conductivity (κ_L) was obtained by subtracting the electronic thermal conductivity (κ_e) from the total thermal conductivity, κ. κ_e was estimated using Wiedemann-Franz law, $\kappa_e = L_o \sigma T$, where L_o = 2.45 x 10^{-8} $W\Omega K^{-2}$ is the Lorenz number. The lattice thermal conductivity of the matrix and the samples with x≤ 2 wt% Co remains almost constant at 4 W/Km in the whole temperature range; whereas samples with 5 wt% and 10 wt% Co exhibited a marginal increase in the lattice thermal conductivity with increasing temperature. Further increasing Co concentration to 12.5 wt% and 15 wt% leads to a drop of the lattice thermal conductivity to 2.1 W/Km at 300 K. The lattice thermal conductivity for the sample with 15 wt% Co decreases with increasing temperature to a value as low as 1.2 W/Km at 775 K. The observed low lattice thermal conductivity of the sample with 15 wt% Co reduction

can be explained by effective phonon scattering by the high density of HH/FH nano-interfaces formed with the nanocomposites.

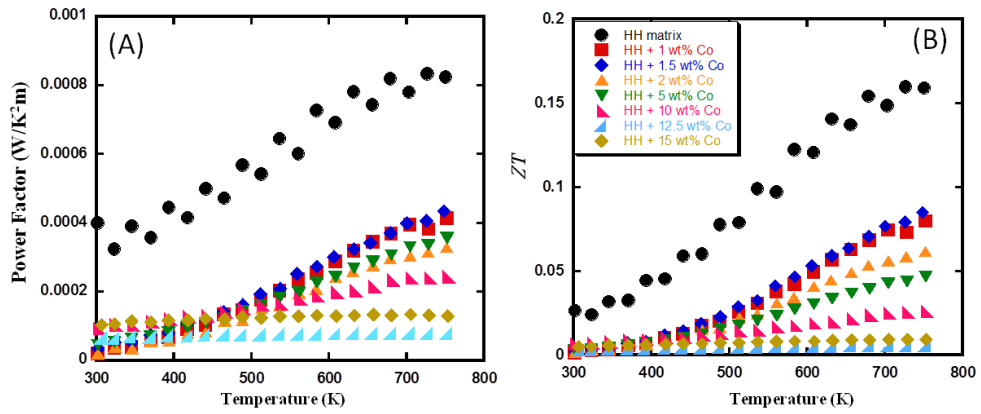

Figure 7.4 Temperature dependence of (A) power factor and (B) figure of merit of FH/HH bulk composites.

Figures 7.4A and 7.4B show the temperature dependence of the power factor and figure of merit (ZT) of various bulk $Hf_{0.25}Zr_{0.75}NiSn$/ $Hf_{0.25}Zr_{0.75}NiCoSn$ (HH/FH) composites. Highest values of the power factor (PF) were observed for the matrix in the whole temperature range. This large power factor for the HH matrix is due to its large thermopower values. The power factor of the samples with low Co concentration ($x \leq 5$ wt%) rapidly increases with increasing temperature; while samples with 10 wt%, 12.5 wt% and 15 wt% Co concentration shows a weak temperature dependence of the power factor. The power factor of samples with low Co concentration ($x \leq 5$ wt%) show a marginal decrease with increasing Co concentration in the whole temperature range suggesting that the drop of the thermopower is compensated by an increasing in the electrical conductivity. Samples with 10 wt%, 12.5 wt% and 15 wt% Co show a rapidly decreasing power factor with increasing Co concentration suggesting that the electrical conductivity in these samples cannot compensate the dramatic drop in the thermopower.

Using the power factor and thermal conductivity data, a ZT value of 0.16 for the matrix was observed at 775 K. The HH matrix and samples with excess Co show almost constant ZT values at 300 K. Regardless of temperature, ZT values for various $Hf_{0.25}Zr_{0.75}NiSn$/ $Hf_{0.25}Zr_{0.75}NiCoSn$ (HH/FH) samples decrease with increasing Co concentration. This can be attributed to the large increase in the electrical conductivity and drastic drop in the thermopower due to both the large increase of the overall carrier density as well as bipolar conduction resulting from the formation of p-type Co-containing FH inclusions within the n-type HH matrix[111].

7.3 Conclusion

In summary, the effect of Co-FH nanostructures on the thermoelectric properties of the n-type HH matrix, $Zr_{0.25}Hf_{0.75}NiSn$, was investigated. The composites were synthesized by high temperature solid-state reaction of the pre-synthesized HH phase with various amounts of elemental Co. We observed that the added Co element diffuse into vacant tetrahedral sites within the HH structure to form Co-containing inclusions with FH structure[112]. The volume fraction of the FH inclusions is controlled by adjustment of the amount of elemental Co used in the starting mixture. When the concentration of Co element is less than 5 wt%, the FH phase is formed as spherical nanoparticles with diameter ranging from 1 nm to 3 nm, dispersed in the HH matrix. However, increasing the concentration of Co to more than 10 wt% resulted in the formation of large interconnected metallic FH inclusions. The embedded Co-FH inclusions contribute holes into the *n*-type HH matrix leading to a bipolar conduction. This result in a drastic drop in the thermopower and marginal increase in the electrical conductivity for samples containing low volume fraction of the Co-FH inclusions; whereas samples with high volume

fraction of Co-FH inclusions showed extremely low thermopower and very high electrical conductivity[111]. The total thermal conductivity of the composites increased with increasing concentration of excess Co. This is attributed to an increase in the electronic thermal conductivity due to the contribution of metallic FH inclusions to the electronic conductivity. Interestingly, samples with 12.5 wt% and 15 wt% Co exhibited a dramatic decreased when the electronic thermal conductivity was taken away. This was due to the formation of FH/HH nano-interface. The combination of the power factor and thermal conductivity, the matrix had the highest ZT value, 0.16 at 775K. And ZT decreased with increasing Co concentration.

CHAPTER 8

CONCLUSION

To improve the ZT value for thermoelectric materials, enhancements in the electrical conductivity and Seebeck coefficient must be achieved simultaneously with a reduction in the thermal conductivity. However, this ideal condition is very difficult to realize in traditional semiconductors. In this thesis, we explored several simple, cheap and efficient approaches to enhance various electronic and thermal properties of HH matrices through creation of FH nanophases, doping and grain size refinement. In our studies, it was found that the energy filtering effect resulting from the contribution of FH nanophases in the HH matrix led to enhancements of the Seebeck coefficient and carrier mobility of various HH/FH nanocomposites.

Building on results from Part-I, we explore in the second part the effect of FH nanoinclusions on electronic transport in $Ti_{0.1}Zr_{0.9}Ni_{1+x}Sn$ matrix heavily doped via Sb substitution at Sn sites. Several samples of the Sb-doped nanocomposites, $Ti_{0.1}Zr_{0.9}Ni_{1+x}Sn_{0.975}Sb_{0.025}$ containing incremental volume fractions of the FH second phases were synthesized through solid-state reaction of the elements. We found that, increasing the concentration of excess Ni, resulted in the agglomeration of small semiconducting FH particles into large FH aggregates with metallic conductivity. The metallic FH phase does not exhibit the energy filtering effects observed in Part I. Instead, a large increase in the carrier density was observed in samples with increasing volume fraction of the FH second phase. This suggests

additional doping of the Sb-doped HH matrix by the embedded metallic FH nanostructures. Therefore, a large increase in the electrical conductivity and a drastic drop in the thermopower were measured in most Sb-doped $Ti_{0.1}Zr_{0.9}Ni_{1+x}Sn_{0.975}Sb_{0.025}$ composites. However, large reductions in the thermal conductivity were observed in samples with increasing Ni concentration.

In the third part, the effect of band gap engineering through isoelectronic substitution of Sn by Ge and mass fluctuation arising from the intermixing of Ti and Zr in the HH structure on the electronic and thermal transports of $Ti_xZr_{1-x}NiSn_{0.975}Ge_{0.025}$ HH matrix in the temperature range from 300 K to 775 K was investigated. A large reduction in the lattice thermal conductivity was observed with increasing Ti concentration. Surprisingly, the thermopower and electrical conductivity for the sample with x = 0.25 simultaneously increase with rising temperature. The combined reduction in lattice thermal conductivity via mass fluctuation at the Ti/Zr site and optimization of the thermopower and electrical conductivity through Ge substitution at the Sn site significantly improved the figure of merit from 0.05 to 0.48 at 775 K for the sample with x = 0.25.

In part IV, we apply the concept of energy filtering at HH/FH interfaces in $Zr_{0.25}Hf_{0.75}Ni_{1+x}Sn_{1-y}Sb_y$ (x = 0~0.15 and y = 0.025, 0.01, 0.005, 0) composites with varying doping levels. We observed that in the heavily doped regime, the effect of energy filtering at the HH/FH interfaces on the overall carrier density of the $Zr_{0.25}Hf_{0.75}Ni_{1+x}Sn_{1-y}Sb_y$ composites is marginal. We show that this behavior is due to the fact that extrinsic carriers originating from Sb substitutions at Sn sites occupy high-energy states in the conduction band of the HH matrix, leading to their effective transmission across the potential energy barrier at the HH/FH interfaces. Therefore, extrinsic carriers dominate electronic conduction in such a system and the filtering of

low energy intrinsic carriers at the HH/FH interfaces has a negligible effect on the overall carrier density of the compounds.

In the last chapter, we explore the effect of the variation in chemical composition of FH inclusions on the electronic and thermal properties of HH phases. This is achieved by reacting elemental Co with $Zr_{0.25}Hf_{0.75}NiSn$ polycrystalline powder. X-ray diffraction and transmission electron microscopy studies revealed the formation, through solid-state atomic diffusion, of nanoparticles of Co containing full-Heusler (FH) phases within the HH matrix. We found that the electrical conductivity of the resulting $Zr_{0.25}Hf_{0.75}NiCo_xSn$ samples initially remains constant for samples with $x \leq 0.02$, while the thermopower drastically drops for the sample with $x = 0.02$. For Co content $x \geq 0.05$, the electrical conductivity gradually increases and the thermopower drops with increasing Co content. This electronic behavior suggests that at low Co content the electrical conduction is dominated by charge carrier compensation between the *n-type* HH matrix and isolated *p-type* Co-containing inclusions, whereas at high Co content, electronic percolation between Co-containing inclusions results in bipolar conduction within the $Zr_{0.25}Hf_{0.75}NiCo_xSn$ composites.

REFERENCE

1. Snyder, G. J.; Toberer, E. S., Complex thermoelectric materials. *Nat Mater* **2008,** *7* (2), 105-114.

2. Vineis, C. J.; Shakouri, A.; Majumdar, A.; Kanatzidis, M. G., Nanostructured Thermoelectrics: Big Efficiency Gains from Small Features. *Adv Mater* **2010,** *22* (36), 3970-3980.

3. Liu, Y. F.; Sahoo, P.; Makongo, J. P. A.; Zhou, X. Y.; Kim, S. J.; Chi, H.; Uher, C.; Pan, X. Q.; Poudeu, P. F. P., Large Enhancements of Thermopower and Carrier Mobility in Quantum Dot Engineered Bulk Semiconductors. *J Am Chem Soc* **2013,** *135* (20), 7486-7495.

4. Makongo, J. P. A.; Misra, D. K.; Salvador, J. R.; Takas, N. J.; Wang, G. Y.; Shabetai, M. R.; Pant, A.; Paudel, P.; Uher, C.; Stokes, K. L.; Poudeu, P. F. P., Thermal and electronic charge transport in bulk nanostructured $Zr_{0.25}Hf_{0.75}NiSn$ composites with full-Heusler inclusions. *J Solid State Chem* **2011,** *184* (11), 2948-2960.

5. Sahoo, P.; Liu, Y. F.; Makongo, J. P. A.; Su, X. L.; Kim, S. J.; Takas, N.; Chi, H.; Uher, C.; Pan, X. Q.; Poudeu, P. F. P., Enhancing thermopower and hole mobility in bulk p-type half-Heuslers using full-Heusler nanostructures. *Nanoscale* **2013,** *5* (19), 9419-9427.

6. Takas, N. J.; Sahoo, P.; Misra, D.; Zhao, H. F.; Henderson, N. L.; Stokes, K.; Poudeu, P. F. P., Effects of Ir Substitution and Processing Conditions on Thermoelectric Performance of p-Type $Zr_{0.5}Hf_{0.5}Co_{1-x}Ir_xSb_{0.99}Sn_{0.01}$ Half-Heusler Alloys. *J Electron Mater* **2011,** *40* (5), 662-669.

7. Makongo, J. P. A.; Misra, D. K.; Zhou, X. Y.; Pant, A.; Shabetai, M. R.; Su, X. L.; Uher, C.; Stokes, K. L.; Poudeu, P. F. P., Simultaneous Large Enhancements in Thermopower and Electrical Conductivity of Bulk Nanostructured Half-Heusler Alloys. *J Am Chem Soc* **2011,** *133* (46), 18843-18852.

8. Sahoo, P.; Djieutedjeu, H.; Poudeu, P. F., Co_3O_4 nanostructures: the effect of synthesis conditions on particles size, magnetism and transport properties. *J Mater Chem A* **2013,** *1* (47), 15022-15030.

9. Hsu, C.-C.; Liu, Y.-N.; Ma, H.-K., Effect of the $Zr_{0.5}Hf_{0.5}CoSb_{1-x}Sn_x$ / HfO 2 half-Heusler nanocomposites on the ZT value. *J Alloy Compd* **2014,** *597*, 217-222.

10. Kim, S.-W.; Kimura, Y.; Mishima, Y., High temperature thermoelectric properties of TiNiSn-based half-Heusler compounds. *Intermetallics* **2007,** *15* (3), 349-356.

11. Biswas, K.; He, J.; Blum, I. D.; Wu, C.-I.; Hogan, T. P.; Seidman, D. N.; Dravid, V. P.; Kanatzidis, M. G., High-performance bulk thermoelectrics with all-scale hierarchical architectures. *Nature* **2012,** *489* (7416), 414-418.

12. Vining, C. B., Semiconductors are cool. *Nature* **2001,** *413* (6856), 577-578.

13. Goldsmid, H. J., The Electrical Conductivity and Thermoelectric Power of Bismuth Telluride. *P Phys Soc Lond* **1958,** *71* (460), 633-646.

14. Goldsmid, H. J., *Thermoelectric refrigeration*. Plenum Press New York: 1964; Vol. 1.

15. Rowe, D. M., Thermoelectric Generators. *Ceram Eng Sci Proc* **2010,** *30* (9), 107-123.

16. Bos, J.-W., Thermoelectric materials: efficiencies found in nanocomposites. *Education in chEmistry* **2012**.

17. Bos, J.-W. G., New compounds and structures in the solid state. *Annual Reports Section" A"(Inorganic Chemistry)* **2012,** *108*, 408-423.

18. Minnich, A.; Dresselhaus, M.; Ren, Z.; Chen, G., Bulk nanostructured thermoelectric materials: current research and future prospects. *Energ Environ Sci* **2009,** *2* (5), 466-479.

19. Gordiakova, G. N.; Sinani, S. S., The Thermoelectric Properties of Bismuth Telluride with Alloying Additives. *Sov Phys-Tech Phys* **1958,** *3* (5), 908-911.

20. Wright, D. A., Thermoelectric Properties of Bismuth Telluride and Its Alloys. *Nature* **1958,** *181* (4612), 834-834.

21. Abrikoso.Nk; Zemskov, V. S.; Iordanis.Ek; Petrov, A. V.; Rozhdest.Vv, Thermoelectric Properties of Silicon-Germanium-Boron Alloys. *Sov Phys Semicond+* **1969,** *2* (12), 1468-&.

22. Steele, M.; Rosi, F., Thermal Conductivity and Thermoelectric Power of Germanium-Silicon Alloys. *J Appl Phys* **1958,** *29* (11), 1517-1520.

23. Meddins, H.; Parrott, J., The thermal and thermoelectric properties of sintered germanium-silicon alloys. *Journal of Physics C: Solid State Physics* **1976,** *9* (7), 1263.

24. Jeitschk.W, Transition Metal Stannides with Mgagas and Mncu2al-Type Structure. *Metall Trans* **1970,** *1* (11), 3159-&.

25. Wyrick, R.; Levinstein, H., Thermoelectric Voltage in Lead Telluride. *Phys Rev* **1950,** *78* (3), 304-305.

26. Bos, J.-W. G.; Downie, R. A., Half-heusler thermoelectrics: A complex class of materials. *Journal of Physics: Condensed Matter* **2014,** *26* (43), 433201.

27. Xie, H.-H.; Mi, J.-L.; Hu, L.-P.; Lock, N.; Chirstensen, M.; Fu, C.-G.; Iversen, B. B.; Zhao, X.-B.; Zhu, T.-J., Interrelation between atomic switching disorder and thermoelectric properties of ZrNiSn half-Heusler compounds. *Crystengcomm* **2012,** *14* (13), 4467-4471.

28. Yu, C.; Zhu, T.-J.; Shi, R.-Z.; Zhang, Y.; Zhao, X.-B.; He, J., High-performance half-Heusler thermoelectric materials Hf 1− x ZrxNiSn 1− ySby prepared by levitation melting and spark plasma sintering. *Acta Mater* **2009,** *57* (9), 2757-2764.

29. Culp, S. R.; Poon, S. J.; Hickman, N.; Tritt, T. M.; Blumm, J., Effect of substitutions on the thermoelectric figure of merit of half-Heusler phases at 800 C. *Appl Phys Lett* **2006,** *88* (4), 2106.

30. Webster, P.; Ziebeck, K., Landolt-Börnstein New Series Group III. Springer, New York: 1988.

31. Otto, M.; Van Woerden, R.; Van der Valk, P.; Wijngaard, J.; Van Bruggen, C.; Haas, C.; Buschow, K., Half-metallic ferromagnets. I. Structure and magnetic properties of NiMnSb and related inter-metallic compounds. *Journal of Physics: Condensed Matter* **1989,** *1* (13), 2341.

32. Misra, D. K.; Makongo, J.; Sahoo, P.; Shabetai, M. R.; Paudel, P.; Stokes, K. L.; Poudeu, P. F., Microstructure and thermoelectric properties of mechanically alloyed $Zr_{0.5}Hf_{0.5}Ni_{0.8}Pd_{0.2}Sn_{0.99}Sb_{0.01}/WO_3$ half-heusler composites. *Sci Adv Mater* **2011,** *3* (4), 607-614.

33. Yaqub, R.; Sahoo, P.; Makongo, J.; Takas, N.; Poudeu, P. F.; Stokes, K. L., Investigation of the Effect of NiO Nanoparticles on the Transport Properties of $Zr_{0.5}Hf_{0.5}Ni_{1-x}Pd_x Sn_{0.99}Sb_{0.01}$ (x= 0 and 0.2). *Sci Adv Mater* **2011,** *3* (4), 633-638.

34. Culp, S. R.; Simonson, J.; Poon, S. J.; Ponnambalam, V.; Edwards, J.; Tritt, T. M., (Zr, Hf) Co (Sb, Sn) half-Heusler phases as high-temperature (≫ 700° C) p-type thermoelectric materials. *Appl Phys Lett* **2008,** *93* (2), 022105-022105-3.

35. Poon, G. J., Electronic and thermoelectric properties of half-Heusler alloys. *Semiconductors and Semimetals* **2001,** *70*, 37-75.

36. Aliev, F.; Kozyrkov, V.; Moshchalkov, V.; Scolozdra, R.; Durczewski, K., Narrow band in the intermetallic compounds MNiSn (M= Ti, Zr, Hf). *Zeitschrift für Physik B Condensed Matter* **1990,** *80* (3), 353-357.

37. Aliev, F.; Brandt, N.; Moshchalkov, V.; Kozyrkov, V.; Skolozdra, R.; Belogorokhov, A., Gap at the Fermi level in the intermetallic vacancy system RBiSn (R= Ti, Zr, Hf). *Zeitschrift für Physik B Condensed Matter* **1989,** *75* (2), 167-171.

38. Simonson, J.; Poon, S., Electronic structure of transition metal-doped XNiSn and XCoSb (X= Hf, Zr) phases in the vicinity of the band gap. *Journal of Physics: Condensed Matter* **2008,** *20* (25), 255220.

39. Barth, J.; Balke, B.; Fecher, G. H.; Stryhanyuk, H.; Gloskovskii, A.; Naghavi, S.; Felser, C., Thermoelectric properties of CoTiSb based compounds. *Journal of Physics D: Applied Physics* **2009,** *42* (18), 185401.

40. Chaput, L.; Tobola, J.; Pécheur, P.; Scherrer, H., Electronic structure and thermopower of Ni ($Ti_{0.5}Hf_{0.5}$) Sn and related half-Heusler phases. *Phys Rev B* **2006,** *73* (4), 045121.

41. Sakurada, S.; Shutoh, N., Effect of Ti substitution on the thermoelectric properties of (Zr, Hf) NiSn half-Heusler compounds. *Appl Phys Lett* **2005,** *86* (8), 082105.

42. Uher, C.; Yang, J.; Hu, S.; Morelli, D. T.; Meisner, G. P., Transport properties of pure and doped MNiSn (M=Zr, Hf). *Phys Rev B* **1999,** *59* (13), 8615-8621.

43. Nanda, B.; Dasgupta, I., Electronic structure and magnetism in doped semiconducting half-Heusler compounds. *Journal of Physics: Condensed Matter* **2005,** *17* (33), 5037.

44. Kroth, K.; Balke, B.; Fecher, G. H.; Ksenofontov, V.; Felser, C.; Lin, H.-J., Diluted magnetic semiconductors with high Curie temperature based on C1b compounds: $CoTi_{1-x}Fe_xSb$. *Appl Phys Lett* **2006,** *89* (20), 202509.

45. Ouardi, S.; Fecher, G. H.; Balke, B.; Kozina, X.; Stryganyuk, G.; Felser, C.; Lowitzer, S.; Ködderitzsch, D.; Ebert, H.; Ikenaga, E., Electronic transport properties of electron-and hole-doped semiconducting C1b Heusler compounds: $NiTi_{1-x}M_xSn$ (M= Sc, V). *Phys Rev B* **2010,** *82* (8), 085108.

46. Sanyal, B.; Eriksson, O.; Suresh, K.; Dasgupta, I.; Nigam, A. K.; Nordblad, P., Ferromagnetism in Mn doped half-Heusler NiTiSn: Theory and experiment. *Appl Phys Lett* **2006,** *89* (21), 212502.

47. Lin, H.; Wray, L. A.; Xia, Y.; Xu, S.; Jia, S.; Cava, R. J.; Bansil, A.; Hasan, M. Z., Half-Heusler ternary compounds as new multifunctional experimental platforms for topological quantum phenomena. *Nat Mater* **2010,** *9* (7), 546-549.

48. Chadov, S.; Qi, X.; Kübler, J.; Fecher, G. H.; Felser, C.; Zhang, S. C., Tunable multifunctional topological insulators in ternary Heusler compounds. *Nat Mater* **2010,** *9* (7), 541-545.

49. Feng, W.; Xiao, D.; Zhang, Y.; Yao, Y., Half-Heusler topological insulators: A first-principles study with the Tran-Blaha modified Becke-Johnson density functional. *Phys Rev B* **2010,** *82* (23), 235121.

50. Graf, T.; Felser, C.; Parkin, S. S., Simple rules for the understanding of Heusler compounds. *Prog Solid State Ch* **2011,** *39* (1), 1-50.

51. Chen, L.; Huang, X.; Zhou, M.; Shi, X.; Zhang, W., The high temperature thermoelectric performances of $Zr_{0.5}Hf_{0.5}Ni_{0.8}Pd_{0.2}Sn_{0.99}Sb_{0.01}$ alloy with nanophase inclusions. *J Appl Phys* **2006,** *99* (6), 064305.

52. Tang, X.; Xie, W.; Li, H.; Zhao, W.; Zhang, Q.; Niino, M., Preparation and thermoelectric transport properties of high-performance p-type Bi2Te3 with layered nanostructure. *Appl Phys Lett* **2007,** *90* (1), 12102-12102.

53. Hsu, K. F.; Loo, S.; Guo, F.; Chen, W.; Dyck, J. S.; Uher, C.; Hogan, T.; Polychroniadis, E.; Kanatzidis, M. G., Cubic AgPbmSbTe2+ m: Bulk thermoelectric materials with high figure of merit. *Science* **2004,** *303* (5659), 818-821.

54. Heremans, J. P.; Jovovic, V.; Toberer, E. S.; Saramat, A.; Kurosaki, K.; Charoenphakdee, A.; Yamanaka, S.; Snyder, G. J., Enhancement of thermoelectric efficiency in PbTe by distortion of the electronic density of states. *Science* **2008,** *321* (5888), 554-557.

55. Poon, S. J.; Wu, D.; Zhu, S.; Xie, W.; Tritt, T. M.; Thomas, P.; Venkatasubramanian, R., Half-Heusler phases and nanocomposites as emerging high-ZT thermoelectric materials. *J Mater Res* **2011,** *26* (22), 2795-2802.

56. Joshi, G.; Yan, X.; Wang, H.; Liu, W.; Chen, G.; Ren, Z., Enhancement in Thermoelectric Figure of Merit of an N-Type Half-Heusler Compound by the Nanocomposite Approach. *Adv Energy Mater* **2011,** *1* (4), 643-647.

57. Kuentzler, R.; Clad, R.; Schmerber, G.; Dossmann, Y., Gap at the Fermi Level and Magnetism in Rmsn Ternary Compounds (R = Ti, Zr, Hf and M + Fe, Co, Ni). *J Magn Magn Mater* **1992,** *104*, 1976-1978.

58. Tobola, J.; Pierre, J.; Kaprzyk, S.; Skolozdra, R. V.; Kouacou, M. A., Crossover from semiconductor to magnetic metal in semi-Heusler phases as a function of valence electron concentration. *J Phys-Condens Mat* **1998,** *10* (5), 1013-1032.

59. Poon, S.; Tritt, T.; Xi, Y.; Bhattacharya, S.; Ponnambalam, V.; Pope, A.; Littleton, R.; Browning, V. In *Bandgap features and thermoelectric properties of Ti-based half-Heusler alloys*, Thermoelectrics, 1999. Eighteenth International Conference on, IEEE: 1999; pp 45-51.

60. Bhattacharya, S.; Xia, Y.; Ponnambalam, V.; Poon, S. J.; Thadani, N.; Tritt, T. M., Reductions in the lattice thermal conductivity of ball-milled and shock compacted TiNiSn1-xSbx half-Heusler alloys. *Thermoelectric Materials 2001-Research and Applications* **2001,** *691*, 155-160.

61. Tritt, T. M.; Bhattacharya, S.; Xia, Y.; Ponnambalam, V.; Poon, S. J.; Thadhani, N., Effects of various grain structure and sizes on the thermal conductivity of Ti-based half-Heusler alloys. *Twentieth International Conference on Thermoelectrics, Proceedings* **2001**, 7-12.

62. Androulakis, J.; Lee, Y.; Todorov, I.; Chung, D.-Y.; Kanatzidis, M., High-temperature thermoelectric properties of n-type PbSe doped with Ga, In, and Pb. *Phys Rev B* **2011,** *83* (19), 195209.

63. Androulakis, J.; Chung, D.-Y.; Su, X.; Zhang, L.; Uher, C.; Hasapis, T. C.; Hatzikraniotis, E.; Paraskevopoulos, K. M.; Kanatzidis, M. G., High-temperature charge and thermal transport properties of the n-type thermoelectric material PbSe. *Phys Rev B* **2011,** *84* (15), 155207.

64. Blum, I. D.; Isheim, D.; Seidman, D. N.; He, J.; Androulakis, J.; Biswas, K.; Dravid, V. P.; Kanatzidis, M. G., Dopant distributions in PbTe-based thermoelectric materials. *J Electron Mater* **2012,** *41* (6), 1583-1588.

65. Girard, S. N.; Chasapis, T. C.; He, J. Q.; Zhou, X. Y.; Hatzikraniotis, E.; Uher, C.; Paraskevopoulos, K. M.; Dravid, V. P.; Kanatzidis, M. G., PbTe-PbSnS2 thermoelectric

composites: low lattice thermal conductivity from large microstructures. *Energ Environ Sci* **2012,** *5* (9), 8716-8725.

66. He, J. Q.; Girard, S. N.; Kanatzidis, M. G.; Dravid, V. P., Microstructure-Lattice Thermal Conductivity Correlation in Nanostructured $PbTe_{0.7}S_{0.3}$ Thermoelectric Materials. *Adv Funct Mater* **2010,** *20* (5), 764-772.

67. He, J. Q.; Girard, S. N.; Zheng, J. C.; Zhao, L. D.; Kanatzidis, M. G.; Dravid, V. P., Strong Phonon Scattering by Layer Structured $PbSnS_2$ in PbTe Based Thermoelectric Materials. *Adv Mater* **2012,** *24* (32), 4440-4444.

68. He, J. Q.; Sootsman, J. R.; Girard, S. N.; Zheng, J. C.; Wen, J. G.; Zhu, Y. M.; Kanatzidis, M. G.; Dravid, V. P., On the Origin of Increased Phonon Scattering in Nanostructured PbTe Based Thermoelectric Materials. *J Am Chem Soc* **2010,** *132* (25), 8669-8675.

69. Lo, S. H.; He, J.; Biswas, K.; Kanatzidis, M. G.; Dravid, V. P., Phonon Scattering and Thermal Conductivity in p-Type Nanostructured PbTe-BaTe Bulk Thermoelectric Materials. *Adv Funct Mater* **2012,** *22* (24), 5175-5184.

70. Ohta, M.; Biswas, K.; Lo, S. H.; He, J. Q.; Chung, D. Y.; Dravid, V. P.; Kanatzidis, M. G., Enhancement of Thermoelectric Figure of Merit by the Insertion of MgTe Nanostructures in p-type PbTe Doped with Na_2Te. *Adv Energy Mater* **2012,** *2* (9), 1117-1123.

71. Zhao, L. D.; He, J. Q.; Hao, S. Q.; Wu, C. I.; Hogan, T. P.; Wolverton, C.; Dravid, V. P.; Kanatzidis, M. G., Raising the Thermoelectric Performance of p-Type PbS with Endotaxial Nanostructuring and Valence-Band Offset Engineering Using CdS and ZnS. *J Am Chem Soc* **2012,** *134* (39), 16327-16336.

72. Zhao, L. D.; He, J. Q.; Wu, C. I.; Hogan, T. P.; Zhou, X. Y.; Uher, C.; Dravid, V. P.; Kanatzidis, M. G., Thermoelectrics with Earth Abundant Elements: High Performance p-type PbS Nanostructured with SrS and CaS. *J Am Chem Soc* **2012,** *134* (18), 7902-7912.

73. Ahn, K.; Biswas, K.; He, J.; Chung, I.; Dravid, V.; Kanatzidis, M. G., Enhanced thermoelectric properties of p-type nanostructured PbTe-MTe (M = Cd, Hg) materials. *Energ Environ Sci* **2013,** *6* (5), 1529-1537.

74. He, J. Q.; Kanatzidis, M. G.; Dravid, V. P., High performance bulk thermoelectrics via a panoscopic approach. *Mater Today* **2013,** *16* (5), 166-176.

75. Zhao, L. D.; Hao, S. Q.; Lo, S. H.; Wu, C. I.; Zhou, X. Y.; Lee, Y.; Li, H.; Biswas, K.; Hogan, T. P.; Uher, C.; Wolverton, C.; Dravid, V. P.; Kanatzidis, M. G., High Thermoelectric Performance via Hierarchical Compositionally Alloyed Nanostructures. *J Am Chem Soc* **2013,** *135* (19), 7364-7370.

76. Xie, W. J.; Yan, Y. G.; Zhu, S.; Zhou, M.; Populoh, S.; Galazka, K.; Poon, S. J.; Weidenkaff, A.; He, J.; Tang, X. F.; Tritt, T. M., Significant ZT enhancement in p-type Ti(Co,Fe)Sb-InSb nanocomposites via a synergistic high-mobility electron injection, energy-filtering and boundary-scattering approach. *Acta Mater* **2013,** *61* (6), 2087-2094.

77. Birkel, C. S.; Zeier, W. G.; Douglas, J. E.; Lettiere, B. R.; Mills, C. E.; Seward, G.; Birkel, A.; Snedaker, M. L.; Zhang, Y. C.; Snyder, G. J.; Pollock, T. M.; Seshadri, R.; Stucky, G. D., Rapid Microwave Preparation of Thermoelectric TiNiSn and TiCoSb Half-Heusler Compounds. *Chem Mater* **2012,** *24* (13), 2558-2565.

78. Birkel, C. S.; Douglas, J. E.; Lettiere, B. R.; Seward, G.; Verma, N.; Zhang, Y.; Pollock, T. M.; Seshadri, R.; Stucky, G. D., Improving the thermoelectric properties of half-Heusler TiNiSn through inclusion of a second full-Heusler phase: microwave preparation and spark plasma sintering of $TiNi_{1+x}Sn$. *Phys Chem Chem Phys* **2013,** *15* (18), 6990-6997.

79. Sumithra, S.; Takas, N. J.; Misra, D. K.; Nolting, W. M.; Poudeu, P. F. P.; Stokes, K. L., Enhancement in Thermoelectric Figure of Merit in Nanostructured Bi_2Te_3 with Semimetal Nanoinclusions. *Adv Energy Mater* **2011,** *1* (6), 1141-1147.

80. Douglas, J. E.; Birkel, C. S.; Miao, M.-S.; Torbet, C. J.; Stucky, G. D.; Pollock, T. M.; Seshadri, R., Enhanced thermoelectric properties of bulk TiNiSn via formation of a $TiNi_2Sn$ second phase. *Appl Phys Lett* **2012,** *101* (18), 183902.

81. Zhao, L.-D.; Hao, S.; Lo, S.-H.; Wu, C.-I.; Zhou, X.; Lee, Y.; Li, H.; Biswas, K.; Hogan, T. P.; Uher, C., High thermoelectric performance via hierarchical compositionally alloyed nanostructures. *J Am Chem Soc* **2013,** *135* (19), 7364-7370.

82. Sahoo, P.; Liu, Y.; Poudeu, P. F., Nanometer-scale interface engineering boosts the thermoelectric performance of n-type $Ti_{0.4}Hf_{0.6}Ni_{1+z}Sn_{0.975}Sb_{0.025}$ alloys. *J Mater Chem A* **2014,** *2* (24), 9298-9305.

83. Precision induction heating. http://www.ambrell.com/heating-with-induction.php.

84. What is induction heating ? http://www.ambrell.com/heating-with-induction.php

85. Rowe, D.; Bunce, R., The thermoelectric properties of heavily doped hot-pressed germanium-silicon alloys. *Journal of Physics D: Applied Physics* **1969,** *2* (11), 1497.

86. Lan, Y. C.; Minnich, A. J.; Chen, G.; Ren, Z. F., Enhancement of Thermoelectric Figure-of-Merit by a Bulk Nanostructuring Approach. *Adv Funct Mater* **2010,** *20* (3), 357-376.

87. Rowe, D.; Shukla, V.; Savvides, N., Phonon scattering at grain boundaries in heavily doped fine-grained silicon–germanium alloys. **1981**.

88. Downie, R. A.; Popuri, S. R.; Ning, H.; Reece, M. J.; Bos, J.-W. G., Effect of Spark Plasma Sintering on the Structure and Properties of Ti1− xZrxNiSn Half-Heusler Alloys. *Materials* **2014,** *7* (10), 7093-7104.

89. Suryanarayana, C., Mechanical alloying and milling. *Prog Mater Sci* **2001,** *46* (1-2), 1-184.

90. T-Tools. http://www.precisiontem.com/ttools.html

91. Klepeis, S.; Benedict, J.; Anderson, R. In *A grinding/polishing tool for TEM sample preparation*, MRS Proceedings, Cambridge Univ Press: 1987; p 179.

92. Rowe, D. M., *CRC handbook of thermoelectrics*. CRC press: 2010.

93. Seebeck coefficient and electrical resistance measuring system.

94. Fistul, V. I., Heavily doped semiconductors. *American Journal of Physics* **1969,** *37*, 1291-1292.

95. Ravich, Y. I.; Efimova, B.; Smirnov, I., Applications of Lead Chalcogenides. In *Semiconducting Lead Chalcogenides*, Springer: 1970; pp 323-346.

96. Chen, S.; Lukas, K. C.; Liu, W.; Opeil, C. P.; Chen, G.; Ren, Z., Effect of Hf Concentration on Thermoelectric Properties of Nanostructured n-Type half-Heusler Materials $Hf_xZr_{1-x}NiSn_{0.99}Sb_{0.01}$. *Adv Energy Mater* **2013,** *3* (9), 1210-1214.

97. Joshi, G.; Dahal, T.; Chen, S.; Wang, H.; Shiomi, J.; Chen, G.; Ren, Z., Enhancement of thermoelectric figure-of-merit at low temperatures by titanium substitution for hafnium in n-type half-Heuslers $Hf_{0.75-x}Ti_xZr_{0.25}NiSn_{0.99}Sb_{0.01}$. *Nano Energy* **2013,** *2* (1), 82-87.

98. Populoh, S.; Aguirre, M.; Brunko, O.; Galazka, K.; Lu, Y.; Weidenkaff, A., High figure of merit in (Ti, Zr, Hf) NiSn half-Heusler alloys. *Scripta Mater* **2012,** *66* (12), 1073-1076.

99. Yan, X.; Liu, W.; Chen, S.; Wang, H.; Zhang, Q.; Chen, G.; Ren, Z., Thermoelectric Property Study of Nanostructured p-Type Half-Heuslers (Hf, Zr, Ti) $CoSb_{0.8}Sn_{0.2}$. *Adv Energy Mater* **2013,** *3* (9), 1195-1200.

100. Yan, X.; Liu, W.; Wang, H.; Chen, S.; Shiomi, J.; Esfarjani, K.; Wang, H.; Wang, D.; Chen, G.; Ren, Z., Stronger phonon scattering by larger differences in atomic mass and size in p-type half-Heuslers $Hf_{1-x}Ti_xCoSb_{0.8}Sn_{0.2}$. *Energ Environ Sci* **2012,** *5* (6), 7543-7548.

101. Liu, Y.; Page, A.; Sahoo, P.; Chi, H.; Uher, C.; Poudeu, P. F., Electronic and phonon transport in Sb-doped $Ti_{0.1}Zr_{0.9}Ni_{1+x}Sn_{0.975}Sb_{0.025}$ nanocomposites. *Dalton T* **2014,** *43* (21), 8094-8101.

102. Kenjo, T.; Kimura, Y.; Mishima, Y. In *Phase stability and thermoelectric properties of half-Heusler compounds (Ti, M) NiSn (M= Zr, Hf)*, MRS Proceedings, Cambridge Univ Press: 2009; pp 1218-Z05-14.

103. Krez, J.; Schmitt, J.; Snyder, G. J.; Felser, C.; Hermes, W.; Schwind, M., Optimization of the carrier concentration in phase-separated half-Heusler compounds. *J Mater Chem A* **2014,** *2* (33), 13513-13518.

104. Downie, R.; MacLaren, D.; Bos, J.-W., Thermoelectric performance of multiphase XNiSn (X= Ti, Zr, Hf) half-Heusler alloys. *J Mater Chem A* **2014,** *2* (17), 6107-6114.

105. Schwall, M.; Balke, B., Phase separation as a key to a thermoelectric high efficiency. *Phys Chem Chem Phys* **2013,** *15* (6), 1868-1872.

106. STADNYK, Y.; Horyn, A.; Hlil, E.; Fruchart, D.; GORELENKO, Y.; Romaka, L., Mechanism of conductivity in n-ZrNiSn intermetallic semiconductor doped with yttrium acceptor impurity. **2009**.

107. Romaka, V.; Fruchart, D.; Hlil, E.; Gladyshevskii, R.; Gignoux, D.; Romaka, V.; Kuzhel, B.; Krayjvskii, R., Features of an intermetallic n-ZrNiSn semiconductor heavily doped with atoms of rare-earth metals. *Semiconductors* **2010,** *44* (3), 293-302.

108. Öğüt, S.; Rabe, K. M., Band gap and stability in the ternary intermetallic compounds NiSnM (M= Ti, Zr, Hf): A first-principles study. *Phys Rev B* **1995,** *51* (16), 10443.

109. Uher, C.; Yang, J.; Hu, S.; Morelli, D.; Meisner, G., Transport properties of pure and doped MNiSn (M= Zr, Hf). *Phys Rev B* **1999,** *59* (13), 8615.

110. Cook, B.; Meisne, G.; Yang, J.; Uher, C. In *High temperature thermoelectric properties of MNiSn (M= Zr, Hf)*, Thermoelectrics, 1999. Eighteenth International Conference on, IEEE: 1999; pp 64-67.

111. Kimura, Y.; Tanoguchi, T.; Kita, T., Vacancy site occupation by Co and Ir in half-Heusler ZrNiSn and conversion of the thermoelectric properties from n-type to p-type. *Acta Mater* **2010,** *58* (13), 4354-4361.

112. Chai, Y. W.; Kimura, Y., Nanosized precipitates in half-Heusler TiNiSn alloy. *Appl Phys Lett* **2012,** *100* (3), 033114.